

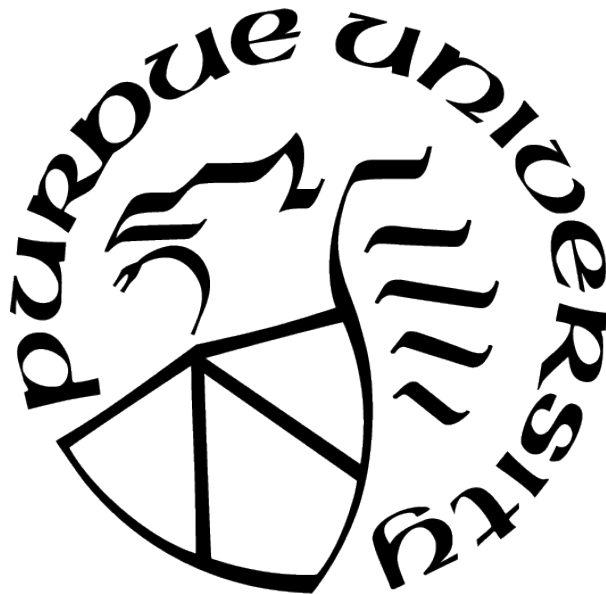
SPACE OBJECT CORRELATION BETWEEN THE SPACE-TRACK AND VIMPEL CATALOGS

by
Nicholas Baietto

A Thesis

*Submitted to the Faculty of Purdue University
In Partial Fulfillment of the Requirements for the degree of*

Master of Science in Aeronautics and Astronautics



School of Aeronautics and Astronautics
West Lafayette, Indiana
May 2022

**THE PURDUE UNIVERSITY GRADUATE SCHOOL
STATEMENT OF COMMITTEE APPROVAL**

Dr. Carolin Frueh, Chair

School of Aeronautics and Astronautics

Dr. Kathleen Howell

School of Aeronautics and Astronautics

Dr. Daniel DeLaurentis

School of Aeronautics and Astronautics

Approved by:

Dr. Gregory Blaisdell

*This work is dedicated to all those who have
believed in me and been with me on my journey.*

ACKNOWLEDGMENTS

There are so many people I would like to thank! Firstly, I would like to thank my advisor Prof. Carolin Frueh. She's been with me every step of the way in my journey here at Purdue and has always served as a generous source of knowledge, wisdom, and encouragement for me throughout my studies and research. I am beyond grateful for all the time I have had to do research with her – it has been an absolute pleasure!

Next, I would like to thank my committee members, Profs. Kathleen Howell and Daniel DeLaurentis for investing their time and effort into my research and defense. I would like to further thank Prof. Howell for being my instructor for AAE 632. It is the only in-person class I was able to attend due to COVID, and she made the already awesome topic of the three-body problem even more fun to learn about!

Additionally, I would like to thank Col. (Ret) Dave Hankins and Dr. Eric Dietz – the heads of the Purdue Military Research Initiative (PMRI) – for taking me in and connecting me to the military community here, and I am very grateful for the funding I have received from PMRI and the Air Force for my studies. I would also like to thank Tomoki Koike for being a great partner and colleague last spring and for developing the code used to download the Space-Track and Vimpel catalogs.

Lastly, I would like to thank all of the people who have been with me and supported me on my journey here. I thank my family and Academy friends who have supported me from afar, and I am so thankful for my military and Catholic friends here who have been by my side through thick and thin. I will treasure the friendships I have made here along with all the secret circles, bundt food items, and parking tickets that came with them!

TABLE OF CONTENTS

LIST OF TABLES	8
LIST OF FIGURES	10
ABBREVIATIONS	12
ABSTRACT	14
1 INTRODUCTION	15
1.1 Current Methods of Space Object Correlation	17
1.1.1 Catalog Correlation	18
1.2 Thesis Scope and Outline	21
2 SPACE OBJECT CATALOGS	23
2.1 The Space-Track Catalog	23
2.2 The Vimpel Catalog	26
2.2.1 The Datefirst.txt File	28
3 ORBITAL THEORY	30
3.1 Two-Body Motion	30
3.2 Time	31
3.2.1 Sidereal Time	33
3.3 Coordinate Frames	34
3.3.1 Inertial Frames: ECI, Geocentric Equatorial	35
3.3.2 Reference Epochs, Mean Systems, and True Systems (TEME, J2000)	37
3.3.3 Earth Centered Earth Fixed (ECEF) Frame	41
3.3.4 Topocentric Equatorial Frame	41
3.3.5 Satellite Reference Frame: RSW	42
3.3.6 Satellite Reference Frame: In-Track, Cross-Track, Out-Of-Plane (ICO)	43
3.4 Classical Orbital Elements	45
3.5 Perturbations	46

3.5.1	Spherical Harmonics	46
3.5.2	Third Body Effects	48
3.5.3	Drag	49
3.5.4	Solar Radiation Pressure	49
3.6	Propagators	50
3.6.1	Simplified General Perturbation 4 (SGP4)	50
3.6.2	Numerical Propagators	51
4	CATALOG CORRELATION THEORY	53
4.1	The Mahalanobis Distance	53
4.2	Uncertainty Distributions	53
4.3	ECI to Topocentric Equatorial Transformations	60
4.3.1	Linear Covariance Matrix Transformation Validation	63
4.4	The Topocentric Right Ascension Rate and Declination Rate Frame	68
4.5	Likelihoods and Log Likelihoods	70
4.6	Two-Body Least Squares	71
5	CATALOG CORRELATION METHODS	73
5.1	Method 1: Direct Catalog Comparison	73
5.1.1	Download Space-Track and Vimpel Catalogs	73
5.1.2	Split Catalogs into Buckets	74
5.1.3	Match Space-Track Objects to Vimpel Objects – Within a Bucket	75
	Filter 1: Squared Mahalanobis Distance (Md2) Filter	75
	Squared Mahalanobis Distance (Md2) Threshold	76
	Filter 2: Classical Orbital Element (COE) Filter	77
5.2	Method 2: Optical Observation Correlation	79
5.2.1	Pull Close Catalogs	79
5.2.2	Determine Potential Catalog Object Matches	80
5.2.3	Calculate Log Likelihoods for Potential Objects	82
	Tracking Data Message (TDM) Likelihood	83
5.2.4	Match the Potential Object with the Highest Likelihood	83

6	VALIDATION AND RESULTS	85
6.1	Direct Catalog Comparison	85
6.1.1	Validation Against the Datefirst.txt File	85
6.1.2	Inconsistency in the Datefirst.txt File	88
6.2	Arc Correlation	90
6.2.1	Validation using the Purdue Optical Ground Station (POGS)	90
6.2.2	DLR TDM Set 1	92
	TDM 1: METEOSAT 8	92
	TDMs 2–5: ASTRA Cluster	93
	TDM 6: Unknown	96
6.2.3	DLR TDM Set 2	97
	TDM 1 (2017-16A): WGS 9	97
	TDM 2 (unassociated)	98
6.2.4	DLR TDM Set 3	106
7	SUMMARY	112
7.1	Conclusions	112
7.2	Recommendations and Future Work	114
	REFERENCES	116

LIST OF TABLES

6.1	GEO bucket combination for catalogs referenced to 3 February 2020 with an md2 threshold of $1 \times 10^6/s^2$	85
6.2	GEO bucket combination for 99 catalog pairs ranging from January, 2019 through December, 2021	86
6.3	All buckets combination for 99 catalog pairs ranging from January, 2019 through December, 2021 with an md2 threshold of $1 \times 10^6/s^2$	86
6.4	GEO bucket combination for catalogs referenced to 3 February 2020 with an md2 threshold of $1 \times 10^7/s^2$	86
6.5	All buckets combination for 99 catalog pairs ranging from January, 2019 through December, 2021 with an md2 threshold of $1 \times 10^7/s^2$	87
6.6	Error analysis of the md2 threshold	87
6.7	Incorrectly Matched Objects from the datefirst.txt file - 3 Feb 2020	88
6.8	Test on an observation set containing 222 observations of NORAD 29486 taken by POGS	90
6.9	Arc Correlation test on 6 DLR TDMs	92
6.10	TDM 1: Likely Space-Track objects	93
6.11	TDM 2: Likely Space-Track objects	95
6.12	TDM 3: Likely Space-Track objects	95
6.13	TDM 4: Likely Space-Track objects	95
6.14	TDM 5: Likely Space-Track objects	95
6.15	TDM 6: Likely Space-Track objects	97
6.16	Arc Correlation results for 2017-16A TDM	97
6.17	TDM 1: Likely Space-Track objects	98
6.18	TDM 1: Likely Vimpel objects	98
6.19	TDM 2 Space-Track object matches	99
6.20	TDM 2 Vimpel object matches	101
6.21	Arc Correlation results for 1993-056A TDM	106
6.22	Arc Correlation results for 1994-035A TDM	106
6.23	Arc Correlation results for 1996-042A TDM	106
6.24	Arc Correlation results for 1999-063A TDM	106

6.25	Arc Correlation results for 2002-001A TDM	107
6.26	Arc Correlation results for 2002-040A TDM	107
6.27	Arc Correlation results for 2005-049B TDM	107
6.28	Arc Correlation results for 2006-012A TDM	107
6.29	Arc Correlation results for 2007-046A TDM	107
6.30	Arc Correlation results for 2009-017A TDM	107
6.31	Arc Correlation results for 2010-039A TDM	108
6.32	Arc Correlation results for 2012-035B TDM	108
6.33	Arc Correlation results for 2015-034A TDM	108
6.34	Arc Correlation results for 2017-016A TDM	108

LIST OF FIGURES

1.1	Historical launch and payload data from space-track.org [3]	15
1.2	Percentage of payloads meeting the 25-year deorbit standard [6]	16
2.1	Example TLE/3LE [26]	24
2.2	Section of Vimpel orbital data from 01/29/2018 [27]	27
2.3	Top portion of datefirst.txt file from 7 January 2022	28
3.1	Sidereal Day vs. Solar Day [29]	32
3.2	Apparent and Mean Sidereal Times [29]	33
3.3	ECI frame [30]	36
3.4	Geocentric Equatorial frame [29]	36
3.5	Precession and nutation of Earth from solar and lunar torques [31]	37
3.6	MOD, TOD, TEME vernal equinox directions [32]	38
3.7	Topocentric Equatorial Frame ($\alpha := \alpha'$, $\delta := \delta'$) [29]	42
3.8	RSW frame [30]	43
3.9	ICO frame overlaid onto RSW frame	44
3.10	Visual representation of the COEs [29]	45
3.11	Zonal, Tesseral and Sectoral Harmonics [33]	47
4.1	1 day Monte Carlo GEO uncertainty simulation ($i = 0^\circ$, $n=100$)	55
4.2	1 day Monte Carlo GEO uncertainty simulation ($i = 25^\circ$, $n=100$)	55
4.3	1 day Monte Carlo GEO uncertainty simulation ($i = 45^\circ$, $n=100$)	56
4.4	10 day Monte Carlo GEO uncertainty simulation ($i = 25^\circ$, $n=1000$)	56
4.5	2D projection of Gaussian ellipsoids – size comparison	59
4.6	ECI uncertainty ellipsoid	64
4.7	ra (α'), dec (δ') linear transformation	64
4.8	ra (α'), dec (δ') linear vs true transformation: $s = 100$ km	65
4.9	ra (α'), dec (δ') linear vs true transformation: $s = 1000$ km	65
4.10	ra (α'), dec (δ') linear vs true transformation: $s = 10000$ km	66
4.11	LEO object (ISS – NORAD 25544) ra (α'), dec (δ') linear vs true transformation: $s = 1000$ km	67

4.12	GEO object (WGS 9 – NORAD 42075) ra (α'), dec (δ') linear vs true transformation: $s = 1000$ km	67
4.13	Two observations with one potential Space-Track object in the α' , δ' frame . . .	68
4.14	Change between the two observations in Figure 4.13 in the $\Delta\alpha'$, $\Delta\delta'$ frame . . .	68
5.1	Md2 threshold set to ∞ – case for a Vimpel object 79504	76
5.2	Space-Track potential matches for an observation	81
6.1	Space-Track catalog objects 41879 and 42075 [3]	89
6.2	ESA Classification of Geosynchronous Objects, Issue 21, pairing WGS 9 to Vimpel 92400 [44]	89
6.3	Difference between NORAD 29486 distribution (light blue) and observation position (blue asterisk) for newly processed POGS observations	91
6.4	ASTRA cluster in the observation frame for an observation in TDM 2 OS 7 . .	93
6.5	ASTRA cluster in the observation frame for an observation in TDM 2 OS 8 . .	94
6.6	ASTRA cluster in the observation frame for an observation in TDM 2 OS 9 . .	94
6.7	Determined least squares two-body orbit for the observation sets pertaining to NORAD 36745	102
6.8	Right Ascension residuals for the NORAD 36745 two-body least squares orbit determination	103
6.9	Declination residuals for the NORAD 36745 two-body least squares orbit determination	103
6.10	Undetermined least squares two-body orbit for the observation sets pertaining to NORAD 14497	104
6.11	Undetermined least squares two-body orbit for the observation sets pertaining to NORAD 44803	104
6.12	TDM 7: Vimpel object 25701 at first observation in set	109
6.13	TDM 7: Vimpel object 25701 at second observation in set	110
6.14	TDM 7: Vimpel object 25701 at third observation in set	110

ABBREVIATIONS

AMR	Area-To-Mass Ratio
CFSCC	Combined Force Space Component Command
COEs	Classical Orbital Elements
DLR	German Aerospace Center
ECEF	Earth Centered Earth Fixed
ECI	Earth Centered Inertial
EOL	End-of-life
ESA	European Space Agency
ESASDT	European Space Agency Space Debris Telescope
GEO	Geostationary Orbit
HEO	High-Eccentricity Orbit
HS	Human Spaceflight
IAM	Institute of Applied Mathematics
ICO	In-Track, Cross-Track, Out-Of-Plane
INN	Inertial Nearest Neighbor
IOD	Initial Orbit Determination
JSC	Joint Stock Corporation
LEO	Low Earth Orbit
MEO	Mid-Earth Orbit
Md2	Squared Mahalanobis Distance
MTT	Multiple Target Tracking
NASA	National Aeronautics and Space Administration
POGS	Purdue Optical Ground Station
SDP4	Simplified Deep-Space Perturbations
SGP4	Simplified General Perturbations
SID	Space Information Dynamics
SO	Space Object
SRP	Solar Radiation Pressure

SSA	Space Situational Awareness
SSN	United States Space Surveillance Network
TDM	Tracking Data Message
TEME	True Equator Mean Equinox
TLE	Two-Line Element
US	United States
USSPACECOM	United States Space Command
WDC-A-R&S	World Data Center-A for Rockets and Satellites
ZimLAT	Zimmerwald Laser and Astrometry Telescope
ZimSMART	Zimmerwald Small Robotic Telescope
3LE	Three-Line Element
18 SPCS	18 th Space Control Squadron

ABSTRACT

Earth-orbiting space debris poses a severe threat to current and future space missions. To combat the dangers of debris, countries (and companies) perform collision avoidance using catalogs of space objects. Better technology has also led to the detection of more space objects, increasing the amount of data in these catalogs. With this increase in data comes a greater need for a single comprehensive catalog without duplicates, and this work proposes two methods of catalog correlation to address this need. These methods are tested using the publicly available Space-Track (US) and Vimpel (Russian) catalogs. The first method, called direct catalog comparison, directly correlates the Space-Track and Vimpel catalogs to determine the same objects between them. This method is validated using the `datefirst.txt` file – a file from Vimpel which lists Space-Track and Vimpel object pairs. When correlating the Vimpel objects in the `datefirst.txt` file to the Space-Track catalog, the direct catalog comparison method produces over 90% of these pairs. It is also found that the `datefirst.txt` file pairing for Vimpel 92400 should be NORAD 42075 and not NORAD 41879. The second method, arc correlation, uses optical observations received from the Purdue Optical Ground Station and the German Aerospace Center to correlate optical observations to both of the catalogs. By matching observations to objects in the catalogs, these catalog objects are indirectly correlated to each other. This method is validated using tracking data messages containing observation sets of tasked Space-Track objects in various orbits. For all tasked Space-Track objects, even ones in a cluster, the tracking data messages are appropriately matched to the Space-Track catalog. For the cases where Vimpel objects are associated with these Space-Track objects – as claimed by the `datefirst.txt` file (except for the case listed above) – the appropriate Vimpel objects are matched to the tracking data messages. When observation sets of unknown objects are tested, the arc correlation method produces distinct and viable candidate matches for both catalogs. Overall, the direct catalog combination and arc correlation methods can be used together to effectively correlate the Space-Track and Vimpel catalogs, aiding the development of a comprehensive catalog of space objects.

1. INTRODUCTION

The National Aeronautics and Space Administration (NASA) defines space debris as “both natural meteoroid and artificial (human-made) orbital debris” and further defines orbital debris as “any human-made object in orbit about the Earth that no longer serves a useful function” [1]. As of January 5th, 2022, the European Space Agency (ESA) reported about 4900 active human-made satellites, 36500 orbital debris greater than 10 cm, one million orbital debris between 1-10 cm, and 330 million orbital debris between 1 mm to 1 cm [2]. New launches and payloads continue to increase these numbers. Figure 1.1 shows the history of annual launches and deployed payloads.

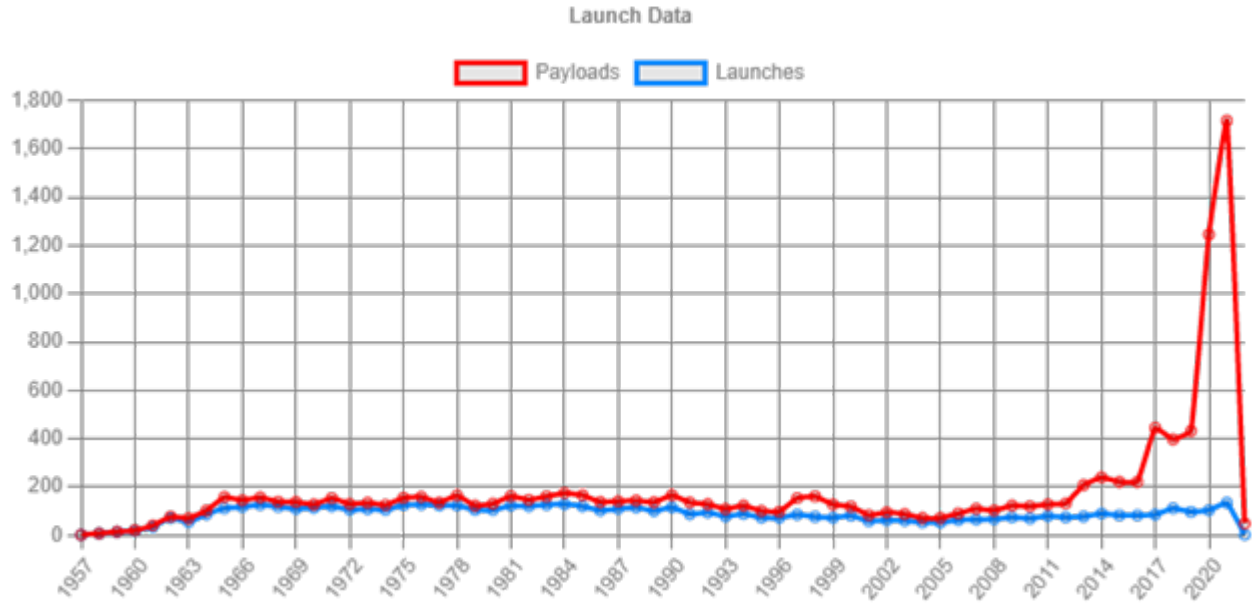


Figure 1.1. Historical launch and payload data from space-track.org [3]

Figure 1.1 is relatively constant throughout the earlier years of space operations; however, the last decade shows a spike in the number of deployed payloads culminating with over 1700 payloads released in 2021 alone. With an increase in satellites and debris, collisions become more likely. Collisions in space are dangerous because space objects travel with very high velocities – up to 7.8 km/s in Low Earth Orbit (LEO) [4] – allowing even the smaller debris to damage or destroy active spacecraft [1].

The increase in spacecraft and debris point to a need for debris mitigation and removal. There are currently no consistent methods for active space debris removal; however, objects in a low enough orbit will naturally decay over time and be removed from the space environment. For LEO payloads in their post mission phase, NASA requires that they deorbit within 25 years [5] as a way to mitigate some space debris. Unfortunately, this requirement is not always met. Figure 1.2 – taken from the ESA’s 2021 Space Environment Report – gives information on the percentage of payloads compliant with this 25-year standard.

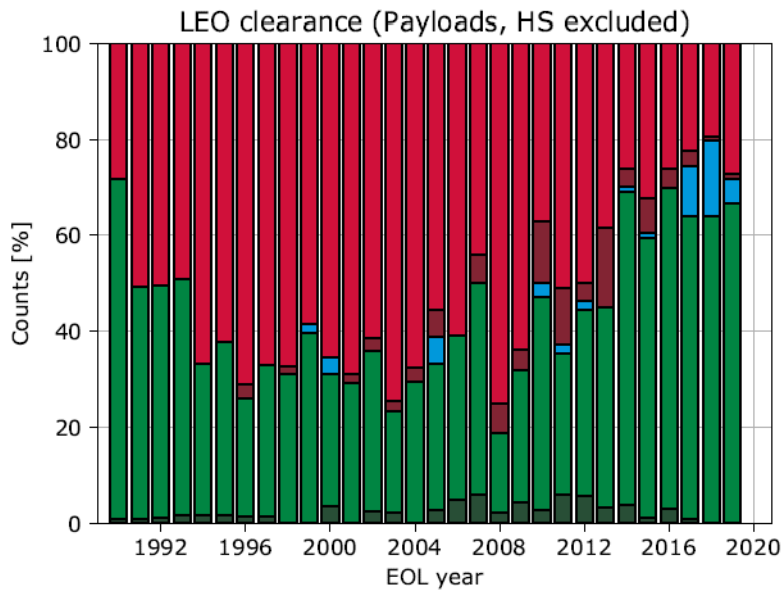


Figure 1.2. Percentage of payloads meeting the 25-year deorbit standard [6]

Figure 1.2 is a histogram with the percentage of payloads by count on the vertical axis and the end-of-life (EOL) year on the horizontal axis. The EOL year marks when a satellite is no longer active and is in its final orbit. The dark green, green, and blue sections make up the percentage of payloads that deorbit within 25 years post-mission, and the red and maroon areas show the percentage of payloads that do not meet this standard. HS stands for Human Spaceflight, and these missions are excluded from this graph. Figure 1.2 shows a 40% increase in payloads meeting the 25-year standard from the late 1990s to the late 2010s. While this standard will help limit the number of new debris introduced into the space environment, it does not attack the problem of debris already in space.

Until an effective solution for debris removal is implemented, mitigation techniques such as collision detection and avoidance keep active payloads in flight and operational. These techniques require access to complete and accurate catalogs of space objects. By propagating cataloged objects forward in time, potential collisions can be detected and avoided. When there are future methods of space debris removal, they will also likely rely on the accurate locations of space debris stored within these catalogs.

Catalogs of space objects are created with sensor networks. One such network is the United States Space Surveillance Network (SSN). The SSN consists of “30+ ground based radars and optical telescopes” and 6 space-based sensors [7]. Radars provide range, topocentric right ascension, and topocentric declination observations. Optical telescopes provide topocentric right ascension and declination observation pairs – defined in Section 3.3.4. Depending on the radar or optical telescope, rate values (range rate, right ascension rate, declination rate) may also be included with the observations. Space-based sensors provide optical observations for space objects.

The ESA estimates 30630 space objects are tracked and cataloged within all sensor networks [2]. As of January 2022, the United States (US) Space-Track catalog (defined in Section 2.1) contains 25184 of those objects [3], and the rest reside in various other catalogs like the Russian Vimpel catalog (defined in Section 2.2). Ideally, there would exist a single database containing all 30630 objects. Data stored within multiple catalogs would be merged into this database, reducing the condition of propagating the same object more than once. Decreasing the amount of downloaded and processed data would increase the efficiency of debris mitigation algorithms currently using multiple catalogs. As more debris continues to be cataloged, the need for this complete database also continues to rise.

1.1 Current Methods of Space Object Correlation

Single target tracking and multiple target tracking (MTT) are two broad categories of methods used to create and upkeep the catalogs of space objects. Single target tracking uses one measurement per optical observation to create a tracklet (or a “short series of

astrometric positions” [8]) for a single object. Other detections from these observations are marked as clutter since they do not pertain to the tracklet for the single object [9]; however, these observations may be used later to create a tracklet for a different object. These tracklets are then matched to known catalog objects or used to establish new objects. Multiple target tracking (MTT) methods focus on taking all measurements from optical sensor readings and classifying them as catalog objects, new objects, or clutter. Unlike single target tracking, MTT methods work with one or more measurements per observation. The underlying assumption for these methods is that each object is only measured once per observation.

Some common MTT methods include the Bayesian method and the nearest neighbor method. These methods can be run independently of the catalogs to produce tracklets of solely “new” objects. When given the uncertainty distribution for measurements, a Bayesian error classification works very well in producing tracklets and identifying clutter [10]. When this uncertainty is unknown, the nearest neighbor method proves simple and effective. The nearest neighbor method creates tracklets using measurements in close proximity to each other over the observation period. Initial measurements are used to establish another new tracklet or as clutter. When more observations are added, the nearest neighbor acts as a multi-object Kalman filter, updating each tracklet with the closest new measurement [9]. [11] improved upon the nearest neighbor method for objects which cross paths by developing an inertial nearest neighbor (INN) method. INN takes into account the direction of motion of the measurements over time when choosing the closest neighbor for the Kalman filter update step. When working with a catalog, MTT operates in a similar fashion as described above. The only difference is that an MTT algorithm will first attempt to correlate a new measurement with the catalog before classifying it as a new object or clutter.

1.1.1 Catalog Correlation

This thesis relies on the catalog correlation theory for single target tracking and multiple target tracking methods. For these methods, there are two well known algorithms for

catalog correlation: initial orbit determination (IOD) correlation and arc correlation. IOD correlation algorithms take observations, determine/refine a full state orbit (position and velocity), and then correlate them with the full states of the catalog objects. Arc correlation algorithms use catalog object’s states to produce computed tracklets at the time of the observations. The measurements are then correlated to these computed tracklets.

The first IOD algorithm was created in 1780 by Laplace followed shortly after by Gauss in 1809 [12]. These IOD methods run by taking in three optical observations and returning a determined state at the second observation time. To work effectively, these three observations should be far enough apart in space but close enough together in time – preferably within a single revolution. In 1997, Gooding created an IOD algorithm which more accurately determines an orbit when given observations spanning multiple revolutions [13]. The challenge of accurately determining orbits from closely spaced observations still persists today.

It is simple to obtain multiple observations for a single object within a short period as many optical telescopes deliver tracklets for each observed object. Unfortunately, using three observations from a single tracklet for IOD will likely fail as tracklets usually contain observations that are too close together. Milani et al. attacks the problem of single tracklet orbit determination by producing admissible regions and, from them, multiple hypothetical orbits [14]. With the emergence of a new class of optical detectors known as photon counting devices, optical observations can give both angle and angle rate information [15]. Angle rates can sometimes also be extracted from the tracklets themselves. [16] uses these angle rates to reduce the hypothetical IODs for a given tracklet. [17] addresses this problem by correlating multiple tracklets of unknown objects observed in a sensor network to each other using a full least-squares solution. If the least-squares solution converges for a collection of tracklets, then it is likely that these tracklets all pertain to the same object. Better yet, the success of the least-squares algorithm results in an initially determined orbit for the object related to these tracklets. A similar least-squares process is used later in this thesis to correlate unknown tracklets from the German Aerospace Center (DLR).

With a successful initial orbit determination, the orbits for observed objects can be correlated to the orbits of cataloged objects. [18] provides a method for correlating objects based on their Keplerian states which is built upon and used in this thesis. Another method of catalog correlation – arc correlation – skips the initial orbit determination process entirely. Arc correlation reverses the IOD process by taking the determined orbits of catalog objects and computing tracklets from them. The computed tracklets for the catalog objects are for the same epoch as the observed tracklet. After this computation, the observed tracklet is correlated to the computed tracklets for the catalog objects. [19] uses this method to develop a working correlation algorithm which proves very successful but relies heavily on accurate uncertainty information for the cataloged objects.

In many catalogs available today, little to no error data for an object is provided. TLEs, the data format used in the Space-Track catalog, do not provide error information. The Vimpel catalog provides a single error value for the in-track direction of an object but does not give any error information for the cross-track or out-of-plane directions. Thus, error estimation is a crucial component in the overall process of space object correlation. Current research in this error estimation focuses on the TLEs and observations of known objects. Specifically, [20] takes TLEs from objects in the geostationary orbit (GEO) and high-eccentricity orbit (HEO) regimes and computes extrinsic errors by correlating optical observations from the Zimmerwald Laser and Astrometry Telescope (ZimLAT), the Zimmerwald Small Robotic Telescope (ZimSMART), and the ESA Space Debris Telescope (ESASDT). This work pulls on research from [8] which performed a similar error analysis using data from the DISCOS catalog. [20] found the errors between the observations and TLEs were about 25 km in-track and 10 km cross-track for GEO objects and 35 km in-track and 25 km cross-track for HEO objects. This data is discussed in Section 4.2 for the error estimation of TLEs for this thesis.

Newer research in the correlation of space objects also uses radar observations. [21] capitalizes on the range parameter provided by radar to perform catalog correlation with just a single observation. The algorithm starts by applying two filters – one for the field of view of the radar during the observation time and the other for the height of the observation

– to reduce the number of potential catalog matches. Then, a maximum error prism in the RSW coordinate system is created using defined error estimates. The RSW coordinate system – further defined in Section 3.3.5 – has an origin, O, located at the center of the space object. The R-axis points in the radial direction (from the center of the Earth), the S-axis points perpendicular to the R-axis in the direction of the velocity vector, and the W-axis is normal to the orbital plane. If the relative position of a catalog object to the observed object falls within this prism, the observation is matched to the catalog object. Otherwise, the observation remains unmatched. The filters help reduce the computational intensity of the algorithm, and the error prism enables an appropriate correlation between observed and cataloged objects. Both of these techniques are used in this thesis for efficient and effective catalog correlation.

Another challenge in the correlation of space objects is spacecraft maneuvers. When a spacecraft performs a maneuver, its past observations will no longer accurately describe its orbit. For this reason, a known catalog object can be identified as a new object after its maneuver. [22] attacks this problem by establishing a set of criteria for determining whether a newly identified object is just a known object that has performed a maneuver or if it is new. One of the challenges of catalog combination is the potential for one catalog to have pre-maneuver information for an object and the other catalog to have post maneuver information for an object. This information mismatch would result in an improper correlation. This issue is noted as a possible source of error for active payloads but is not addressed further in this thesis.

1.2 Thesis Scope and Outline

This thesis focuses on correlating the Space-Track and Vimpel catalogs to determine and verify the same objects between them. This correlation is performed using a modified nearest neighbor approach which relies on the closest mahalanobis distance between the cataloged objects themselves and from optical observations to the catalog objects. In Chapter 2, the necessary background on the Space-Track catalog, Vimpel catalog, and datefirst.txt file (used

for validation) is given. Chapter 3 provides the orbital theory and systems that are needed when performing single and multi-target tracking for Earth orbiting space objects. Chapter 4 dives into the specific theory behind the two modified nearest neighbor algorithms used in this thesis to directly (direct catalog correlation) and indirectly (arc correlation) correlate the Space-Track and Vimpel catalogs, and Chapter 5 outlines these methods. The direct catalog correlation algorithm is tested against 99 pairs of Space-Track and Vimpel catalogs ranging from January 2019 through December 2021, and the arc correlation algorithm is tested using optical observations of tasked objects received from the Purdue Optical Ground Station (POGS) and from the German Aerospace Center (DLR). Chapter 6 shows the validation and results of these catalog correlation methods and tests. Lastly, Chapter 7 summarizes the conclusions drawn from this research and gives future recommendations on research that could stem from this thesis.

2. SPACE OBJECT CATALOGS

Two publicly available catalogs of space objects are the US (Space-Track) and Russian (Vimpel) catalogs. On a large scale, catalogs of space objects offer Space Situational Awareness (SSA) which “refers to keeping track of objects in orbit and predicting where they will be at any given time” [23]. SSA for both active satellites and space debris are provided within the Space-Track and Vimpel catalogs, making them useful for space debris mitigation. For these catalogs, Coordinated Universal Time (UTC) is used – defined in Section 3.2.

2.1 The Space-Track Catalog

The Space-Track catalog (www.space-track.org) is owned by the United States Space Command (USSPACECOM) and the Combined Force Space Component Command (CFSCC) and managed/populated by the 18th Space Control Squadron (18 SPCS) [24]. Surveillance data of unclassified objects in the form of two-line elements (TLEs) or three-line elements (3LEs) are available to general users [3]. TLEs use the True Equator Mean Equinox (TEME) Earth Centered Inertial (ECI) reference frame described in Section 3.3.2.

The TLE format was created by the North American Aerospace Defense Command (NORAD) as a standard for cataloging space objects. These “two 69-character lines of data” are used with NORAD’s simplified general perturbations (SGP4) model or NORAD’s simplified deep-space perturbations (SDP4) model – defined in Section 3.6.1 – to output the position and velocity of the TLE object [25]. The TLE/3LE format is described using definitions from [25] and is shown in Figure 2.1.

Line 0: (Only included in a 3LE)

- Name of Satellite: The alphanumeric designator of an object.

Line 1:

- Satellite Number: The assigned NORAD ID to each object in the catalog. The ‘U’ stands for unclassified (all public objects have this classification).

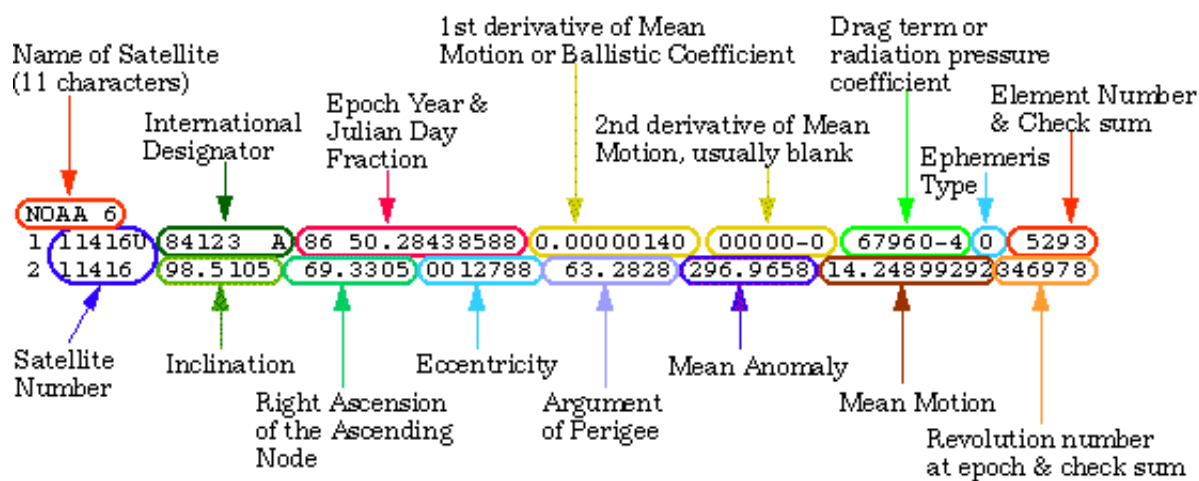


Figure 2.1. Example TLE/3LE [26]

- International Designator: An additional designator assigned by the World Data Center-A for Rockets and Satellites (WDC-A-R&S). The first two numbers are the last two digits of the launch year. The remaining numbers note the launch number of the year (Launch 123 in the case of Figure 2.1). The alphabetic term refers to the piece of the launch.
- Epoch Year & Julian Day Fraction: The epoch is the reference time for the TLE (the time this data corresponds to). The first two digits are the last two digits of the year. The remaining digits correspond to the fractional day of that year.
- 1st and 2nd derivatives of Mean Motion: These fields show the change in mean motion over time. They are not used with the SGP4 or SDP4 models. The decimal point is assumed for the 2nd derivative of Mean Motion.
- Drag term or radiation pressure coefficient: This term is the BSTAR term and is a SGP4 drag coefficient. It gives an idea of how susceptible an object is to drag – the higher the number, the more susceptible. The decimal point is assumed for this term.
- Ephemeris Type: Represents the model used to generate the data (distributed sets have a value of zero).
- Element Number & Check sum: All digits except the last digit in this section pertain to the element set number. This number is ideally incremented every time a new element set is generated. The last digit in each line is a modulo-10 checksum of the data in this line (sum all numbers in the line – giving minus signs a value of 1 and ignoring all other characters – and see if the last digit of the sum equals the last digit of the line).

Line 2:

- Satellite Number: As in line 1, this ID is the NORAD ID assigned to the object. It must match the satellite number in line 1 for this TLE to be valid.

- Orbital Elements: Inclination (0-180 degrees), Right Ascension of the Ascending Node (0-360 degrees), Eccentricity (unitless, decimal point assumed), Argument of Perigee (0-360 degrees) and Mean Anomaly (0-360 degrees).
- Mean Motion: The number of revolutions per day.
- Revolution number at epoch & check sum: All digits in this section except the last digit pertain to the number of revolutions this object has completed from launch until the given epoch time. The last digit is the modulo-10 checksum of the data in this line (the same as in line 1).

Unfortunately, TLEs do not give any covariance data. Estimates of this covariance are needed for both catalog correlation and the correlation of observations to a single catalog. Section 1.1 describes some of the methods other researchers have used to estimate the error for TLE objects. Section 4.2 discusses the methods of covariance estimation used within this thesis.

2.2 The Vimpel Catalog

The Vimpel catalog is owned and maintained by Russia, and the following information about this catalog is from the Vimpel website (<http://spacedata.vimpel.ru>) [27]. The Joint Stock Corporation (JSC) and the Keldysh Institute of Applied Mathematics (IAM) partner with Russia to collect, process, and analyze optical observations. This catalog focuses on objects with an orbital period of over 200 minutes – mainly objects with GEO or HEO orbits.

There are some differences between the Vimpel and Space-Track catalogs. First, objects in this catalog are in the J2000 ECI reference frame – described in Section 3.3.2 – not the TEME ECI reference frame. Second, all data is stored in a single line (instead of two or three lines in TLEs or 3LEs). There are fifteen parameters stored for each observed object, separated by commas. Figure 2.2 shows a few lines of Vimpel data from January 29th, 2018.

1,	12500,26122008,30012018	000860,	19,	8298.0,	63.328,262.286,0.089046,	0.0,300.485,1.23e-02,	17.4,	0.2,	88
2,	12700,18022009,29012018	224605,	11,	8408.1,	63.289,151.565,0.070940,	0.1,122.866,2.86e-02,	17.1,	0.3,	135
3,	12801,23122016,30012018	011453,	13,	8279.0,	63.205,331.946,0.190327,	359.9,350.747,8.48e-02,	16.5,	24.6,	19

Figure 2.2. Section of Vimpel orbital data from 01/29/2018 [27]

Parameters (columns):

1. Sequence Number: The line number – starts with 1 and increments by one for each line (“1, 2, 3” seen in Figure 2.2)
2. The Space Object (SO) number: The assigned Vimpel ID to each cataloged object.
3. The date of the first measurement of the object: In day, month, year [DDMMYYYY] format.
4. The reference (epoch) time of the data: In day, month, year, hours, minutes, seconds [DDMMYYYY HHMMSS] format.
5. The gap time: Note how each object’s argument of latitude at its reference time (#10) in Figure 2.2 is around 0 degrees (or 360 degrees). Each object in the Vimpel catalog is propagated from its last known observation to the time of the ascending node closest to the catalog date – 01/29/2018 in the case of Figure 2.2. This closest time is the reference time (#4). The gap time is the number of days between the last observation of an object and its reference time.
6. Semi-major axis: [km]
7. Inclination: [degrees]
8. Right Ascension of the Ascending Node: [degrees]
9. Eccentricity: [unitless]
10. Argument of latitude at the reference time: [degrees]
11. Argument of perigee: [degrees]
12. Average value of effective area to mass: Used to calculate the effects of drag, [m²/kg]

13. SO magnitude: The apparent magnitude of the space object, [m]
14. Time uncertainty of object longitudinal position at a confidence level of 0.5, [minutes]
15. Position uncertainty at reference time for the confidence level of 0.5, [km]

The Vimpel catalog is published weekly. As stated in the description of the gap time parameter, the data for each object is propagated from its last known observation to its reference time. These propagated parameters are all stored in osculating Keplerian elements referred to the epoch J2000. Osculating elements are the exact value of these parameters at the reference time. A numerical propagator taking into account the Earth’s gravitational field, the gravitational field of the Sun and the Moon, Solar radiation pressure, and the Earth’s atmosphere is used to propagate these objects to the reference time. The Space Information Dynamics (SID) research group’s numerical propagator, discussed in Section 3.6.2, is used to propagate Vimpel data for this thesis.

2.2.1 The Datefirst.txt File

Russia also provides a ‘datefirst.txt’ file on the Vimpel website. This file lists the Vimpel objects appearing in the Space-Track catalog, paring Vimpel IDs to NORAD IDs, and a section of it is shown in Figure 2.3. The first column, Nvym, contains the Vimpel ID and the third column contains its paired Space-Track NORAD ID, Nnor. t_det_v is the date of detection of the Vimpel object, and t_det_n is the date of first information of the Space-Track object in the website space-track.org.

Nvym	t_det_v	Nnor	t_det_n
010201	20200716	45952	20200727
010400	20200524	45932	20200722
010901	20200720	45924	20200722
011400	20200728	45928	20200722
011401	20200520	45989	20200727
011500	20200512	45836	20200629

Figure 2.3. Top portion of datefirst.txt file from 7 January 2022

The `datefirst.txt` file for 7 January 2022 is used to validate the results for the direct catalog comparison method described in Section 5.1, and it contains 902 pairs of Space-Track and Vimpel objects. A drawback of the `datefirst.txt` file is that there is no justification provided from Vimpel for these pairings. In Section 6.1.2, it is shown that at least two of the pairings are incorrect.

3. ORBITAL THEORY

3.1 Two-Body Motion

The fundamental equation of motion for an object in a near-Earth orbit is the relative two-body equation. [28] uses Newton's second law of motion and Newton's law of gravitation to derive this equation. Newton's second law relates the Force, F , acting on a body to the body's mass, m , and inertial acceleration, \ddot{r}_i . Newton's law of gravitation gives the force of gravity of one body acting on a second body.

$$\bar{F} = m\ddot{r}_i \quad (3.1)$$

$$\bar{F}_g = -\frac{Gm_\oplus m_{sat}}{r_{\oplus,sat}^3} \bar{r}_{\oplus,sat} \quad (3.2)$$

G is the universal gravitational constant, m_\oplus is the mass of the Earth (body 1), m_{sat} is the mass of the spacecraft (body 2), $\bar{r}_{\oplus,sat}$ is relative position vector from the Earth to the spacecraft, and $r_{\oplus,sat}$ is the magnitude of $\bar{r}_{\oplus,sat}$. Using Equations 3.1 and 3.2, the gravitational forces on the spacecraft (with respect to the Earth) and on the Earth (with respect to the spacecraft) are derived.

$$\bar{F}_{gsat} = m_{sat}\ddot{r}_{sat} = -\frac{Gm_\oplus m_{sat}}{r_{\oplus,sat}^3} \bar{r}_{\oplus,sat} \quad (3.3)$$

$$\bar{F}_{g\oplus} = m_\oplus\ddot{r}_\oplus = \frac{Gm_\oplus m_{sat}}{r_{\oplus,sat}^3} \bar{r}_{\oplus,sat} \quad (3.4)$$

\ddot{r}_{sat} and \ddot{r}_\oplus are inertial accelerations with respect to an inertially fixed point in space (the center of mass of the Earth, spacecraft system). Eliminating the like mass terms from Equations 3.3 and 3.4 and subtracting them gives the equation for the relative acceleration between the two bodies.

$$\ddot{r} = \ddot{r}_{sat} - \ddot{r}_\oplus = -\frac{Gm_\oplus}{r_{\oplus,sat}^3} \bar{r}_{\oplus,sat} - \frac{Gm_{sat}}{r_{\oplus,sat}^3} \bar{r}_{\oplus,sat} \quad (3.5)$$

$$\ddot{\vec{r}} = -\frac{G(m_{\oplus} + m_{sat})}{r_{\oplus,sat}^3} \vec{r}_{\oplus,sat} \quad (3.6)$$

Four assumptions are given in [28]:

1. The mass of the spacecraft is negligible when compared that of the Earth
2. The coordinate system is inertial with the origin at the center of the Earth (the ECI coordinate frame is used – defined in Section 3.3.1)
3. The Earth and spacecraft bodies are spherically symmetric with uniform density – can be treated as point masses
4. No other forces act on the system

Applying the first assumption and replacing Gm_{\oplus} with μ (the Earth’s gravitational parameter) reduces Equation 3.6 to:

$$\ddot{\vec{r}} = -\frac{\mu}{r_{\oplus,sat}^3} \vec{r}_{\oplus,sat} \quad (3.7)$$

This equation is the basic relative two-body equation for an object in an Earth orbit. With the assumptions, Equation 3.7 fully models the orbit of a spacecraft. Unfortunately, assumptions 3 and 4 are not accurate enough for the long term propagation of space objects. Therefore, the acceleration terms for the perturbations in Section 3.5 are added to Equation 3.7 and used to propagate the catalog objects.

3.2 Time

Before diving into the perturbations accounted for in space object propagation, it is important to discuss the time systems, coordinate frames, and orbital elements used to represent spacecraft states and observations. This section focuses on time and draws from [29]. A solar day is the traditional day of 86400 seconds (24 hours), and it is measured by subsequent meridian transits of the Sun. A sidereal day is defined as the period of the

Earth's rotation – the time between successive meridian passes of the vernal equinox – and it is about 4 minutes shorter than the solar day. This time difference is due to the Sun's right ascension changing about a degree per day. Figure 3.1 illustrates this difference between a solar and sidereal day.

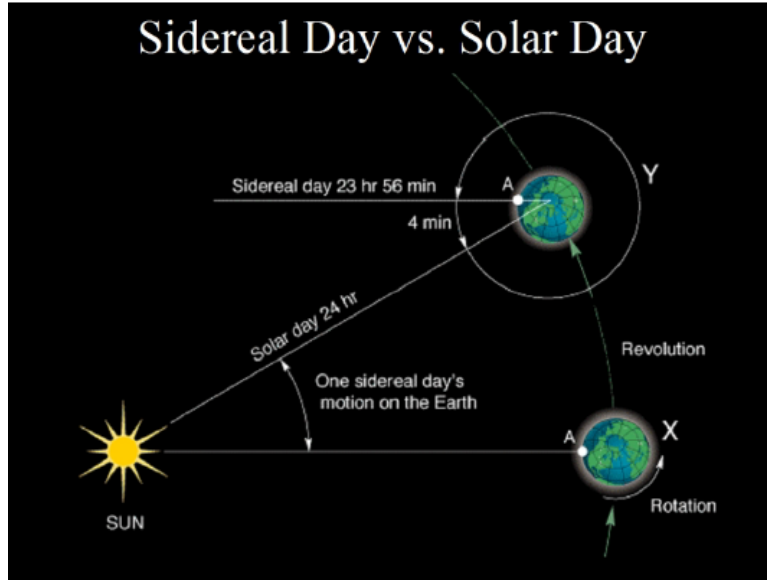


Figure 3.1. Sidereal Day vs. Solar Day [29]

The Earth's motion around the Sun is also affected by the elliptical orbit of the Earth around the Sun and the Earth's rotation axis not being orthogonal to the ecliptic plane. These factors, along with others, affect time calculations and give a need for well defined time scales. Common time scales include Universal Time (UT) – an Earth time scale defined with respect to the mean Sun, Terrestrial Time (TT) – a conceptually uniform time scale measured in 86400 second days, International Atomic Time (TAI) – a practically realized uniform time scale offset from TT by 32.184 seconds and taking the existing clock imperfections into account, Greenwich Mean Sidereal Time (GMST) – the hour angle of the vernal equinox at Greenwich (defined in Section 3.2.1), Universal Time UT1 – the mean solar time in today's standards, and Coordinated Universal Time (UTC) – an offset integer of seconds from TAI that is also kept in close agreement with UT1. In addition to time scales, the Julian Date (JD) is a widely used parameter which gives the exact date in number of days since noon,

12h, on January 1, 4713 BC. A modified Julian date (MJD) is also commonly used and is defined as the number of days since November 17, 1858 at midnight, 0h.

$$MJD = JD - 2400000.5 \quad (3.8)$$

3.2.1 Sidereal Time

The sidereal time is the in-plane hour angle between the vernal equinox and a position on the Earth. The Greenwich sidereal time is known as the specific hour angle between the vernal equinox and the prime meridian (longitude = 0°), while the local sidereal time is the sidereal time of an observer at any longitude value. Sidereal times can be measured from the vernal equinox in the “true” or “mean” system – defined in Section 3.3.2. The sidereal times measured from the true equinox are known as apparent sidereal times, and these times include the Greenwich Apparent Sidereal Time (GAST) Θ_{app} and Local Apparent Sidereal Time (LAST) θ_{app} . The sidereal times measured from the mean equinox include the Greenwich Mean Sidereal Time (GMST) Θ and Local Mean Sidereal Time (LMST) θ . The GAST, LAST, GMST, and LMST are shown in Figure 3.2.

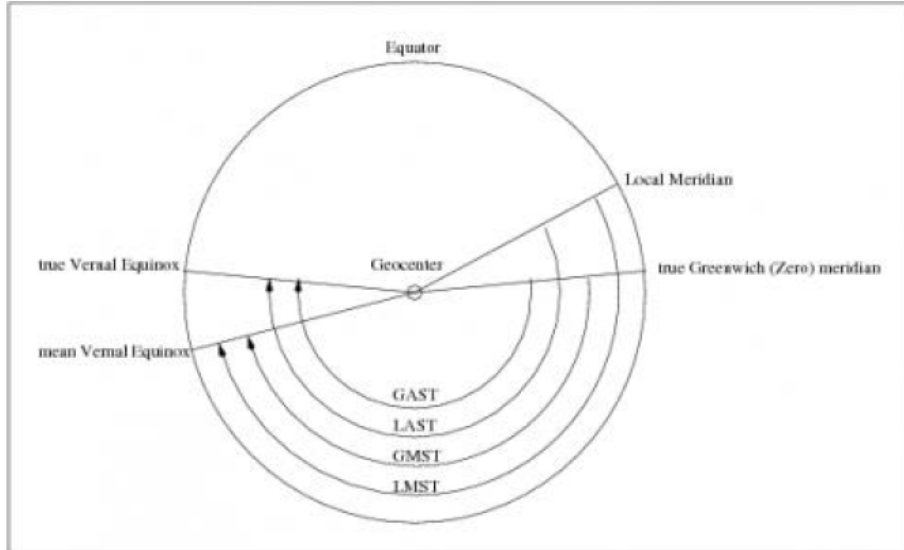


Figure 3.2. Apparent and Mean Sidereal Times [29]

To obtain the local sidereal time, the Greenwich sidereal time is calculated and then a longitude shift is applied. [29] gives a mathematical expression to compute the GMST when given the current Julian Date.

$$\begin{aligned} \Theta(UT) = & 24110.54841sec + 8640184.812866sec \cdot T_0 + 0.093104 \cdot T_1^2 \\ & - 0.0000062 \cdot T_1^3 + 1.0027279093 \cdot UT[sec] \end{aligned} \quad (3.9)$$

$$T_0 = \frac{JD_0 - 2451545}{36525} \quad T_1 = \frac{JD - 2451545}{36525}, \quad (3.10)$$

JD is the Julian Date of the observation time, JD_0 is the Julian Date of midnight (0h) on the observation date, and $UT[sec]$ is the elapsed time in seconds from JD_0 to JD [29]. Once the Greenwich sidereal time is known, the local sidereal time is calculated by adding the observers longitude, λ , to Θ .

$$\theta(UT) = \Theta(UT) + \lambda(1[hour]/15[deg]) \quad (3.11)$$

Equation 3.11 can also be rewritten for apparent sidereal times.

$$\theta_{app}(UT) = \Theta_{app}(UT) + \lambda(1[hour]/15[deg]) \quad (3.12)$$

3.3 Coordinate Frames

[29] defines a coordinate frame using the following quantities:

- origin
- fundamental plane
- direction of reference
- handedness (right/left handed)
- Cartesian or non-Cartesian (spherical, cylindrical)

Coordinate frames such as the Earth Centered Inertial (ECI) and Geocentric Equatorial frames are inertial (non-accelerating) in nature. These two inertial frames have fixed axes with a reference direction (x-axis) pointing towards the vernal equinox. Due to Earth rotational effects (such as nutation and precession), the vernal equinox direction does not remain fixed over time. Therefore, for proper coordinate system transformations, the inertial frames are further defined with respect to J2000 or TEME by Vimpel and Space-Track respectfully. For catalog comparison, the Space-Track objects are transformed from TEME ECI to J2000 ECI. Non-inertial Earth based coordinate frames include the Earth Centered Earth Fixed (ECEF) frame and the Topocentric Equatorial frame. These frames are useful for locating topocenters (ECEF) and for representing spacecraft observations from these topocenters (topocentric equatorial). Satellite fixed frames are another type of coordinate frame, and they are useful when working with the local reference plane of space objects. Two satellite fixed frames are the RSW frame and the In-Track, Cross-Track, Out-Of-Plane (ICO) frame.

3.3.1 Inertial Frames: ECI, Geocentric Equatorial

The Earth Centered Inertial (ECI) frame has an origin located at the center of the Earth. Since this frame is inertial, its origin is assumed to be stationary or moving at a constant velocity. The fundamental plane is the Earth's equator, and the reference direction points through the intersection of the ecliptic and equatorial planes to the vernal equinox at a fixed equinox. Lastly, the frame is right handed and Cartesian.

The Geocentric Equatorial frame has the same characteristics as the ECI frame except that is in spherical coordinates. The coordinates are right ascension α , declination δ , and radial distance r . α is the in-plane angle and is zero in the direction of the vernal equinox, δ is the angle above or below the equator (South $-\pi/2$, North $\pi/2$), and r is the magnitude of the position vector [29]. Figures 3.3 and 3.4 show the ECI and Geocentric Equatorial frames respectfully.

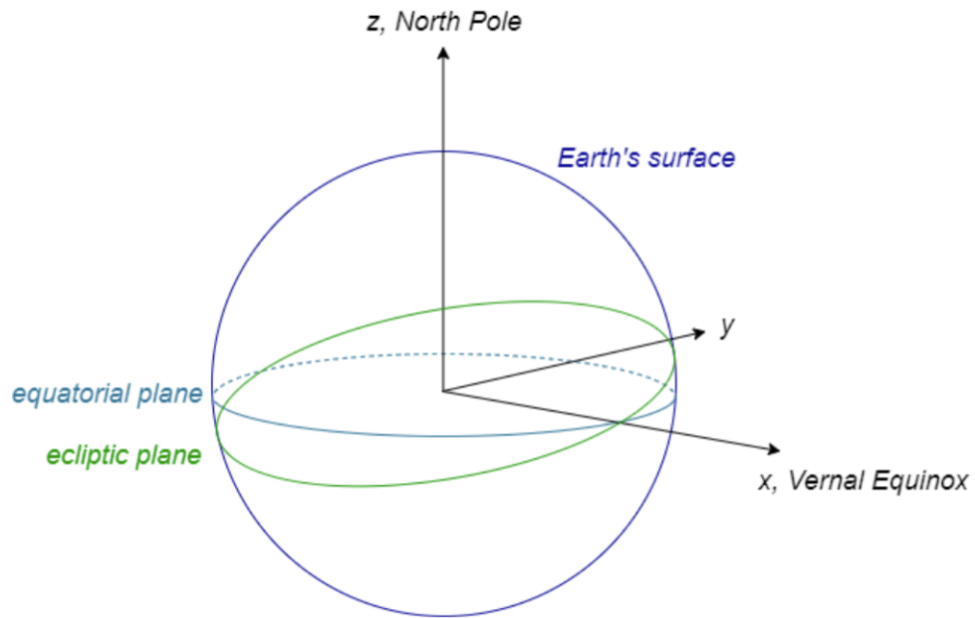


Figure 3.3. ECI frame [30]

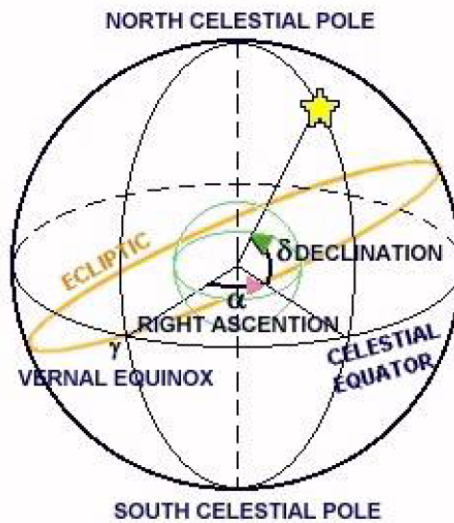


Figure 3.4. Geocentric Equatorial frame [29]

3.3.2 Reference Epochs, Mean Systems, and True Systems (TEME, J2000)

As discussed, the direction of the vernal equinox changes over time due to rotational effects on the Earth. These effects are defined in [29] as precession and nutation and shown in Figure 3.5. Precession describes the change between the orientation of the Earth's rotation axis and the equinox, and it is caused by the torque exerted on the Earth from the Sun, the Moon, and the other planets in the solar system. The orientation due to precession repeats every 26,000 years. Nutation describes the short-term periodic variations between the equator and the vernal equinox due to solar and lunar torques, and these variations repeat on the scale of months.

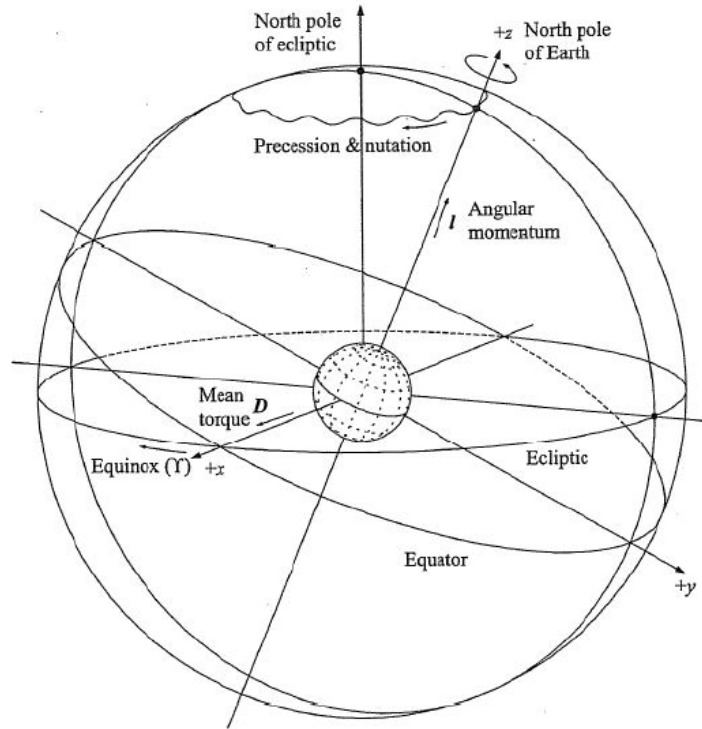


Figure 3.5. Precession and nutation of Earth from solar and lunar torques [31]

With the constant change in the direction to the vernal equinox over time, it is essential to choose a specific reference direction to base the ECI or Geocentric Equatorial coordinate frames on. This reference vernal equinox direction is defined first with respect to an epoch

and second with respect to the “mean” or “true” systems at the epoch. The epoch is simply a chosen time. For J2000, this epoch is noon on January 1st, 2000. For mean of date (MOD), true of date (TOD), and true equator mean equinox (TEME), the epoch is the current time of the given spacecraft state. The “mean” system is of mean equator and mean equinox, and it is calculated using only the precession of the Earth at a given epoch. The “true” system is of true equator and true equinox, and it is calculated using both the secular (precession) effects along with the short-periodic motion (nutation) of the Earth at a given epoch. Figure 3.6 shows the vernal equinox (Υ) directions at a current epoch in the “mean” system (Υ_{MOD}), “true” system (Υ_{TOD}) and TEME system (Υ_{TEME}).

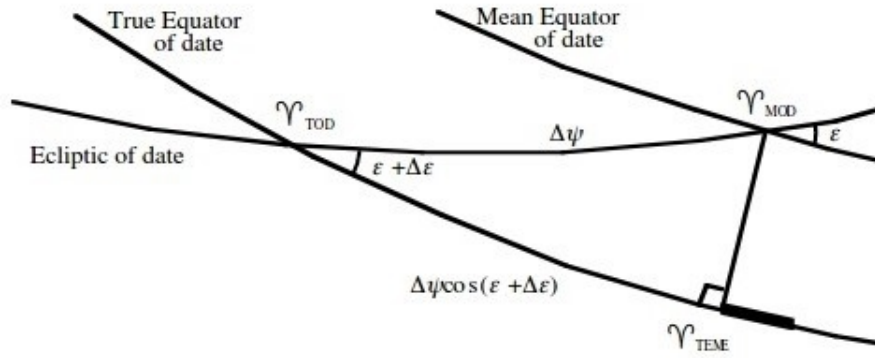


Figure 3.6. MOD, TOD, TEME vernal equinox directions [32]

To transform between the MOD, TOD, and TEME systems for a given epoch, rotation matrices are used. These rotation matrices use ϵ , $\Delta\epsilon$, and $\Delta\psi$ to angles of rotation. ϵ is the mean obliquity of the ecliptic, $\Delta\epsilon$ is the difference between the true and mean obliquity of the ecliptic, and $\Delta\psi$ is the longitude of the mean vernal equinox in relation to the true vernal equinox. [29] gives equations to approximate ϵ , $\Delta\epsilon$, and $\Delta\psi$.

$$\epsilon = 23.43929111^\circ - 46.8150'' \cdot T - 0.00059'' \cdot T^2 + 0.001813'' \cdot T^3 \quad (3.13)$$

$$\begin{aligned}\Delta\epsilon = & 9.203'' \cos(\Omega) - 0.090'' \cos(2\Omega) - 0.547'' \cos(2(F - D + \Omega)) \\ & + 0.098'' \cos(2(F + \Omega))\end{aligned}\tag{3.14}$$

$$\begin{aligned}\Delta\psi = & -17.200'' \sin(\Omega) + 0.202'' \sin(2\Omega) - 1.319'' \sin(2(F - D + \Omega)) \\ & + 0.143'' \sin(l) - 0.227'' \sin(2(F + \Omega))\end{aligned}\tag{3.15}$$

T is the centuries since noon on 1 January 2000 (J2000) measured in terrestrial time (TT), l is the mean anomaly of the Sun, F is the mean distance between the nodes of the moon, D is the mean distance from the Sun to the moon, and Ω is the mean longitude of the moon.

$$T = (JD - 2451545.0)/36525\tag{3.16}$$

$$l = 357.525 \text{ deg} + 35999.049 \text{ deg} \cdot T\tag{3.17}$$

$$F = 93.273 \text{ deg} + 483202.019 \text{ deg} \cdot T\tag{3.18}$$

$$D = 297.850 \text{ deg} + 445267.111 \text{ deg} \cdot T\tag{3.19}$$

$$\Omega = 125.045 \text{ deg} - 1934.136 \text{ deg} \cdot T\tag{3.20}$$

Using ϵ , $\Delta\epsilon$, and $\Delta\psi$, a 3x1 position vector, \bar{r} , or velocity vector, \bar{v} , can be rotated from TEME to TOD to MOD.

$$\bar{r}_{tod} = \mathbf{R}_3(-\Delta\psi \cos(\epsilon + \Delta\epsilon)) \cdot \bar{r}_{teme}\tag{3.21}$$

$$\bar{v}_{tod} = \mathbf{R}_3(-\Delta\psi \cos(\epsilon + \Delta\epsilon)) \cdot \bar{v}_{teme}\tag{3.22}$$

$$\bar{r}_{mod} = \mathbf{N}^T \cdot \bar{r}_{tod}\tag{3.23}$$

$$\bar{v}_{mod} = \mathbf{N}^T \cdot \bar{v}_{tod}\tag{3.24}$$

$$\mathbf{N} = \mathbf{R}_1(-\epsilon - \Delta\epsilon) \cdot \mathbf{R}_3(-\Delta\psi) \cdot \mathbf{R}_1(\epsilon)\tag{3.25}$$

\mathbf{R}_1 and \mathbf{R}_3 are defined as the first and third axis rotation matrices for an angle θ , respectfully. A positive θ means the system is rotating in the mathematical positive direction.

$$\mathbf{R}_1(\theta) = \begin{bmatrix} 1 & 0 & 0 \\ 0 & \cos(\theta) & \sin(\theta) \\ 0 & -\sin(\theta) & \cos(\theta) \end{bmatrix} \quad (3.26)$$

$$\mathbf{R}_3(\theta) = \begin{bmatrix} \cos(\theta) & \sin(\theta) & 0 \\ -\sin(\theta) & \cos(\theta) & 0 \\ 0 & 0 & 1 \end{bmatrix} \quad (3.27)$$

For completeness, the second axis rotation matrix \mathbf{R}_2 for an angle θ is

$$\mathbf{R}_2(\theta) = \begin{bmatrix} \cos(\theta) & 0 & -\sin(\theta) \\ 0 & 1 & 0 \\ \sin(\theta) & 0 & \cos(\theta) \end{bmatrix}. \quad (3.28)$$

Equations 3.21 - 3.25 allow for the transformation between “mean”, “true”, and TEME systems at a specific epoch. For this research the mean J2000 reference system is used. Thus, mean equator and equinox of the observation epoch T (MOD) vectors need to be transformed to mean equator and equinox of J2000 vectors. [29] gives three Euler angles (ζ , θ , and z) that can be used to create a rotation matrix to transform 3x1 position and velocity vectors from MOD to mean of J2000.

$$\bar{\mathbf{r}}_{J2000} = \mathbf{P}^T \cdot \bar{\mathbf{r}}_{mod} \quad (3.29)$$

$$\bar{\mathbf{v}}_{J2000} = \mathbf{P}^T \cdot \bar{\mathbf{v}}_{mod} \quad (3.30)$$

$$\mathbf{P} = \mathbf{R}_3(-z) \cdot \mathbf{R}_2(\theta) \cdot \mathbf{R}_3(-\zeta) \quad (3.31)$$

$$\zeta = 2306.2181'' \cdot T + 0.30188'' \cdot T^2 + 0.017998'' \cdot T^3 \quad (3.32)$$

$$\theta = 2004.3109'' \cdot T - 0.42665'' \cdot T^2 - 0.041833'' \cdot T^3 \quad (3.33)$$

$$z = \zeta + 0.79280'' \cdot T^2 + 0.000205'' \cdot T^3 \quad (3.34)$$

3.3.3 Earth Centered Earth Fixed (ECEF) Frame

The rest of the frames discussed are non-inertial coordinate frames. This first frame, ECEF, has an origin located at the center of the Earth with a reference direction pointing to the intersection of the prime meridian and the equator (latitude = 0° , longitude = 0°). The fundamental plane is the Earth's equator, and the frame is right handed and Cartesian. Since the reference direction is set to a point on the Earth, the ECEF frame is useful for identifying the positions of observation sites (topocenters) as they are just the latitude, longitude, and altitude of the site transformed into Cartesian coordinates.

To transform a position from the ECEF frame to the ECI frame, the the Greenwich sidereal time Θ is used, and the Greenwich sidereal time is calculated from the current Julian Date in Equation 3.9. Using the \mathbf{R}_3 rotation matrix, a position or velocity vector in the ECEF frame can be transformed into the ECI frame.

$$\bar{r}_{eci} = \mathbf{R}_3(-\Theta) \cdot \bar{r}_{ecef} \quad (3.35)$$

$$\bar{v}_{eci} = \mathbf{R}_3(-\Theta) \cdot \bar{v}_{ecef} \quad (3.36)$$

Another rotational effect on the Earth is known as polar motion. Polar motion describes the short periodic variations (up to 10 meters) between the Earth pole and the ephemeris pole. Because of these variations, the true transformation between the ECEF and ECI frames would need to take into account both the polar motion and the sidereal time. Since the effects of polar motion are so small compared to other errors, however, this research only uses the sidereal time for transforming between the ECEF and ECI frames.

3.3.4 Topocentric Equatorial Frame

A frame used when taking observations from observation sites is the topocentric equatorial frame. This frame has an origin on the surface of the Earth, centered at an observer's location. The fundamental plane is the plane parallel to the equator at a fixed equinox, the reference direction is the vernal equinox direction at a fixed equinox, and the frame is right

handed. The coordinate system is in spherical coordinates – right ascension α' , declination δ' , (range ρ) – as shown in Figure 3.7. The local sidereal time θ is used in Equation 3.35 to transform the position vector of the observation site from ECEF coordinates, \bar{R}_{ecef} , to ECI coordinates, \bar{R}_{eci} .

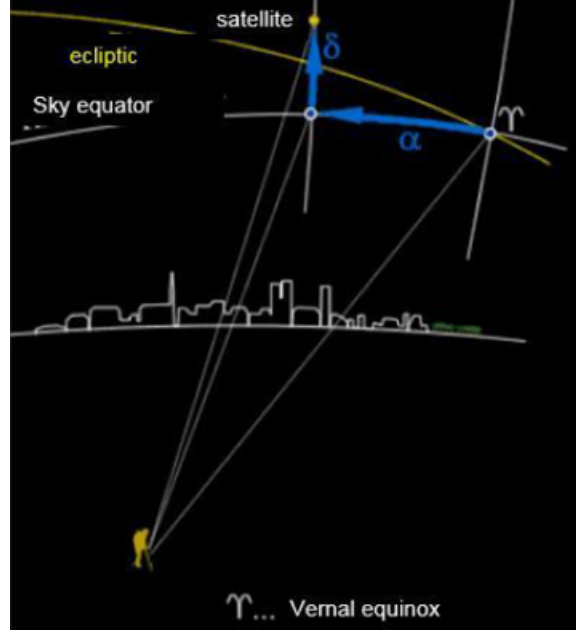


Figure 3.7. Topocentric Equatorial Frame ($\alpha := \alpha'$, $\delta := \delta'$) [29]

When α' , δ' , and ρ are known, the ECI range vector $\bar{\rho}_{eci}$ can be computed. To get the ECI position vector \bar{r}_{eci} , $\bar{\rho}_{eci}$ is added to \bar{R}_{eci} .

$$\bar{\rho}_{eci} = \begin{bmatrix} \rho \cos(\alpha') \cos(\delta') \\ \rho \sin(\alpha') \cos(\delta') \\ \rho \sin(\delta) \end{bmatrix} \quad (3.37)$$

$$\bar{r}_{eci} = \bar{R}_{eci} + \bar{\rho}_{eci} \quad (3.38)$$

3.3.5 Satellite Reference Frame: RSW

A common satellite based coordinate frame is the RSW frame. The origin is located at the spacecraft's center, the fundamental plane is the orbital plane, the reference direction

points in the radial direction (from the Earth to the spacecraft), and the frame is right handed and Cartesian. From Figure 3.8, R is the radial direction from the center of the Earth, W is the two-body orbit angular momentum direction, and S is the direction of the cross product between W and R – where dot product between S and the spacecraft’s velocity vector is positive.

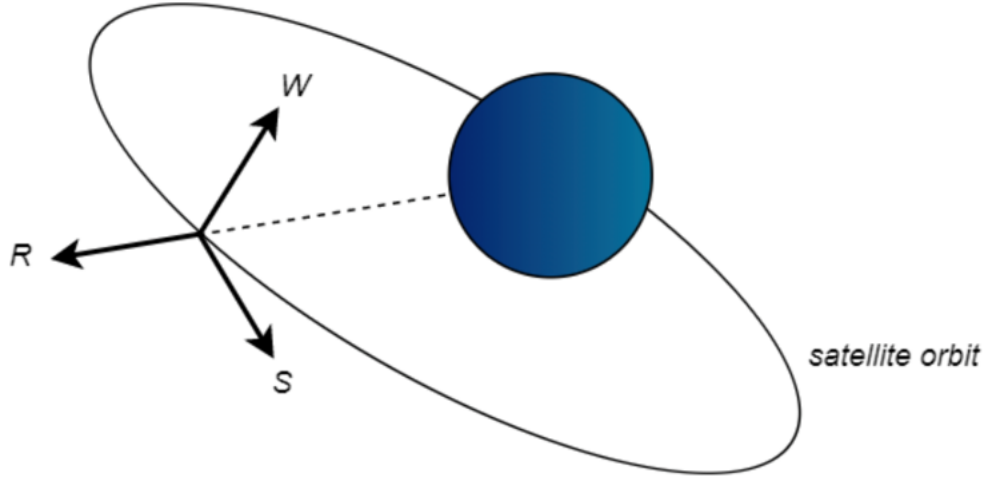


Figure 3.8. RSW frame [30]

3.3.6 Satellite Reference Frame: In-Track, Cross-Track, Out-Of-Plane (ICO)

Another satellite based coordinate frame is the In-Track, Cross-Track, Out-Of-Plane (ICO) frame. Like the RSW frame, the origin is located at the spacecraft’s center, the fundamental plane is the orbital plane, and the frame uses Cartesian coordinates. Unlike RSW, the reference direction points in the direction of motion (the velocity direction) and the frame is left handed. From Figure 3.9, in-track is the velocity direction of the spacecraft, out-of-plane is the two-body orbit angular momentum direction (W from RSW), and cross-track is the direction orthogonal to both in-track and out-of-plane and pointing away from the center of the Earth. Since little uncertainty information is known for the cataloged objects, this frame is used to establish a propagated covariance around them as discussed in Section 4.2.

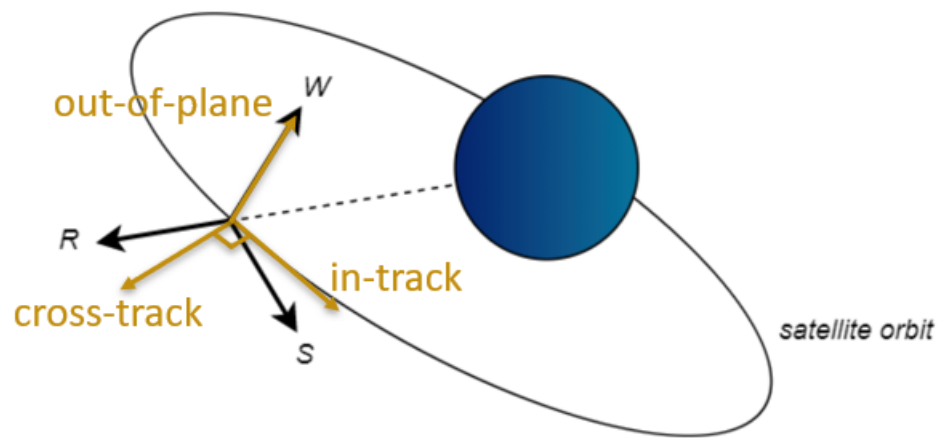


Figure 3.9. ICO frame overlaid onto RSW frame

3.4 Classical Orbital Elements

For two-body orbits, there are a few ways to represent the state of a spacecraft. In an inertial coordinate system, the six Classical Orbital Elements (COEs) – also known as the Keplerian elements – can be used. The COEs are six scalar parameters which describe the size, shape and orientation of an elliptical two-body orbit, along with the spacecrafts location on the orbit. They include the semi-major axis a , the eccentricity e , the inclination i , the right ascension of the ascending node Ω , the argument of perigee ω (perigee for Earth, perihelion for Sun, periapsis for a general body), and the true anomaly ν . i , Ω , ω , and ν are depicted in Figure 3.10.

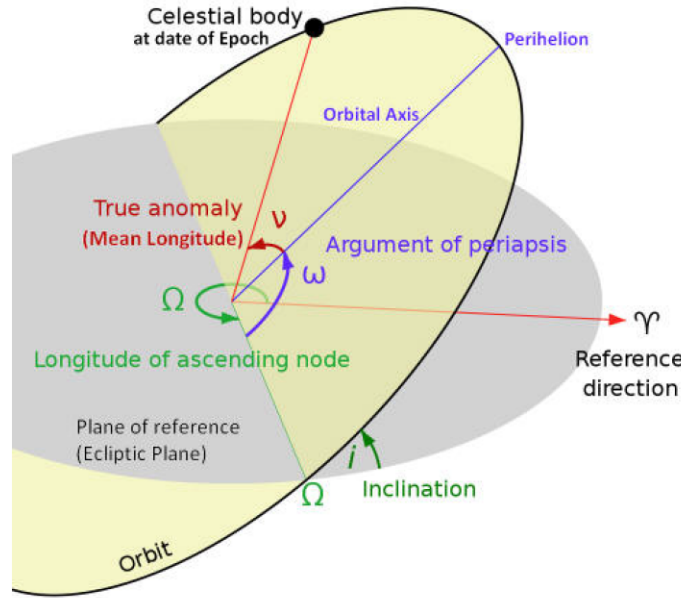


Figure 3.10. Visual representation of the COEs [29]

The semi-major axis a is a measure of the size of an orbit. Specifically it is half of the value of the major axis of the ellipse representing the orbit and is normally given in kilometers in the ECI frame. The eccentricity e for an elliptical orbit is a non-dimensional value between 0 and 1. The larger the value, the more elliptical the orbit is. The inclination i is the angle from the fundamental plane of the inertial frame (The equatorial plane in the ECI frame) to the orbital plane. The right ascension of the ascending node Ω is the angle

from the reference direction of the inertial frame (the vernal equinox direction in the ECI frame) to the ascending node of the orbit. The ascending node is the point in the orbit where the spacecraft crosses the fundamental plane moving in the $+z$ direction. The argument of perigee ω is the angle from the ascending node to perigee. Perigee (or periapsis) is the closest point on the orbit to Earth (or the body being orbited). The furthest away is known as apogee (or apoapsis). The true anomaly ν is the angle from perigee to the spacecraft's location on the orbit. Figure 3.10 depicts the latter four COEs.

3.5 Perturbations

At the end of Section 3.1, it is noted that perturbation acceleration terms need to be added to the relative two-body equation (Equation 3.7) to accurately propagate objects around the Earth. These added acceleration terms address the fact that the Earth is not a point mass or a perfect sphere, other bodies – the Sun and the Moon – have gravitational effects on the Earth and the spacecraft, the Earth's atmosphere is present in lower Earth orbits, and there is Solar Radiation Pressure (SRP) from the Sun.

3.5.1 Spherical Harmonics

The Earth is not a spherically symmetric body with uniform density. Therefore, the two-body assumption that the Earth is a point mass is not sufficient, and a different representation of Earth's gravitational potential is needed. To achieve this representation, the Earth's spherical harmonics must be considered. [29] demonstrates how the spherical harmonics of Earth can be modeled by a series of Legendre polynomials, $P_{l,m}$, where l and m are the respective degree and order for each polynomial. The spherical harmonics can further be broken up into three sections: zonal harmonics ($m = 0$), sectoral harmonics ($l = m$), and tesseral harmonics ($l \neq m \neq 0$). Figure 3.11 shows how each section models the mass distribution of the Earth.

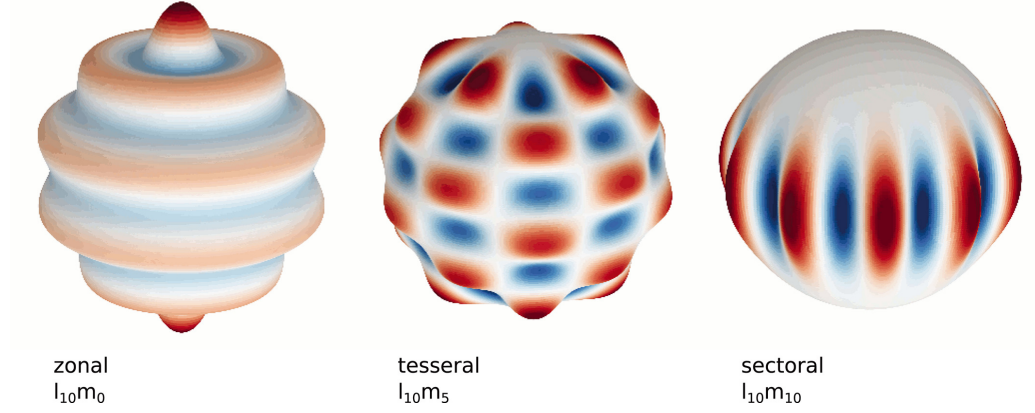


Figure 3.11. Zonal, Tesseral and Sectoral Harmonics [33]

Basically, the zonal harmonics deal with the Earth's horizontal mass distribution, the sectoral harmonics represent the vertical mass distribution, and the tesseral harmonics give a mass distribution grid. The commonly known J_l perturbation terms, with J_2 being the most impactful term, all fall under zonal harmonics. Through proper modeling of the Earth's spherical harmonics with Legendre polynomials, [29] delivers an equation representing the Earth's gravitational potential, U .

$$U = \frac{\mu}{r} + \frac{\mu}{r} \sum_{l=2}^{\infty} \sum_{m=0}^l \left(\frac{R_E}{r}\right)^l P_{l,m}[\sin(\phi_{gc,sat})] (C_{l,m} \cos(m\lambda_{sat}) + S_{l,m} \sin(m\lambda_{sat})) \quad (3.39)$$

R_E is the mean radius of the Earth, $\phi_{gc,sat}$ is the geocentric latitude of the spacecraft, λ_{sat} is the longitude of the spacecraft, and $C_{l,m}$ and $S_{l,m}$ are gravitational coefficients. Equation 3.39 can be reduced to a function of the position of the spacecraft in the Earth Centered Earth Fixed (ECEF) frame, \mathbf{r}^{ECEF} , and the collection of model parameters, $\boldsymbol{\theta}$. The ECEF frame is defined in Section 3.3.3.

$$U = U(\mathbf{r}^{ECEF}, \boldsymbol{\theta}) \quad (3.40)$$

The ECEF acceleration is given by

$$\mathbf{a}_g^{ECEF}(\mathbf{r}^{ECEF}, \boldsymbol{\theta}) = \left[\frac{\partial U(\mathbf{r}^{ECEF}, \boldsymbol{\theta})}{\partial \mathbf{r}^{ECEF}} \right]^T, \quad (3.41)$$

and is rotated to the ECI frame using the transformation of the fixed reference frame to the inertial reference frame, \mathbf{T}_{ECEF}^{ECI} .

$$\mathbf{a}_g^{ECI} = \mathbf{T}_{ECEF}^{ECI} \mathbf{a}_g^{ECEF}(\mathbf{r}^{ECEF}, \boldsymbol{\theta}) \quad (3.42)$$

3.5.2 Third Body Effects

While the gravitational effects of the Earth are the largest for near Earth orbiting spacecraft, other bodies have non-negligible gravitational effects. The Sun and Moon are two commonly considered bodies for the near Earth system. Equation 3.3 shown for the two-body problem in Section 3.1 can be expanded for the n-body problem.

$$m_{sat} \ddot{\mathbf{r}}_{sat} = -G \sum_{i=1}^n \frac{m_i m_{sat}}{r_{i,sat}^3} \bar{\mathbf{r}}_{i,sat} \quad (3.43)$$

[28] reduces Equation 3.43 to the relative n-body problem where $\ddot{\mathbf{r}}$ is the relative acceleration of the spacecraft, body 1 is the Earth (\oplus), and body 2 is the Spacecraft (sat).

$$\ddot{\mathbf{r}} = -G \frac{(m_{\oplus} + m_{sat})}{r_{\oplus,sat}^3} \bar{\mathbf{r}}_{\oplus,sat} + G \sum_{i=3}^n m_i \left(\frac{\bar{\mathbf{r}}_{sat,i}}{r_{sat,i}^3} - \frac{\bar{\mathbf{r}}_{\oplus,i}}{r_{\oplus,i}^3} \right) \quad (3.44)$$

The first term on the right hand side of Equation 3.44 is the two-body acceleration. The third body acceleration is the summation term from this equation. If only the Sun and Moon gravitational effects are taken into account, then the acceleration becomes

$$\bar{a}_{third_body} = Gm_{\odot} \left(\frac{\bar{\mathbf{r}}_{sat,\odot}}{r_{sat,\odot}^3} - \frac{\bar{\mathbf{r}}_{\oplus,\odot}}{r_{\oplus,\odot}^3} \right) + Gm_{moon} \left(\frac{\bar{\mathbf{r}}_{sat,moon}}{r_{sat,moon}^3} - \frac{\bar{\mathbf{r}}_{\oplus,moon}}{r_{\oplus,moon}^3} \right) \quad (3.45)$$

where \odot is the Sun and *moon* is the Moon.

3.5.3 Drag

Another perturbation which affects near Earth objects is drag. The Earth's atmosphere extends far into the LEO regime, significantly perturbing objects in this region. [31] models the force of drag as Equation 3.46

$$\bar{a}_{drag} = -\frac{1}{2}C_D \frac{A}{m_{sat}} \rho v \bar{v} \quad (3.46)$$

where C_D is the drag coefficient of the satellite, A is its cross-sectional area, m_{sat} is its mass, ρ is the atmospheric density at its location, \bar{v} is its relative velocity vector, and v is the magnitude of \bar{v} . The drag coefficient is a dimensionless quantity describing the interaction of the atmosphere with the satellite's surface. Common values of C_D range between 1.5 – 3.0, and in 1966, [34] estimated the C_D for spherical spacecraft to be 2.2. The atmospheric density is obtained by using mathematical atmospheric models. More accurate models will take into account the exospheric temperature, geomagnetic activity, solar flux values, semi-annual variations, and other space weather analysis when calculating a density. Well known atmospheric models include the 1959 ARDC Atmosphere model, the Harris-Priester model, the 1976 US Standard Atmosphere model, the Jacchia 1970 model, the Jacchia-Roberts model, the Mass Spectrometer Incoherent Scatter (MSIS) 1986 and 1990 models, and the NRLMSISE-00 model which builds upon MSIS-90 [35].

3.5.4 Solar Radiation Pressure

Solar radiation pressure (SRP) is the perturbing force on a satellite due to the absorption or reflection of photons from solar radiation [31]. A common assumption is to assume the spacecraft is a spherical object. Using this assumption, [29] models the SRP experienced by a spacecraft as

$$\bar{a}_{SRP} = -\frac{A}{m} \frac{E}{c} \frac{AU^2}{r_{sat,\odot}^2} \left(\frac{1}{4} + \frac{1}{9}C_d \right) \frac{\bar{r}_{sat,\odot}}{r_{sat,\odot}} \quad (3.47)$$

where A/m is the area-to-mass ratio (AMR) of the spacecraft, E is the solar constant at the Earth's surface, c is the speed of light, AU is the astronomical unit, $\bar{r}_{sat,\odot}$ is the vector from the spacecraft to the sun, $r_{sat,\odot}$ is the magnitude of $\bar{r}_{sat,\odot}$, and C_d is the coefficient of diffuse reflection of the spacecraft. The C_d varies based on the spacecraft's surface material.

3.6 Propagators

For this research, catalog objects are either propagated to each other for catalog correlation or propagated to observation times for arc correlation. Therefore, it is necessary to define the types of propagation models and the specific models used for the Space-Track and Vimpel catalogs. Three types of propagation models exist: analytic, numeric and semi-analytic. Analytic models use equations to approximate the motion of an object over time, resulting in fast propagation times and, usually, less accurate propagated states. Numerical models propagate objects by numerically integrating their equations of motion. These models have longer run times, as more computations are required, but tend to be the most accurate type of propagator. Semi-analytic models attempt to find a common ground between analytic and numerical models. To find this middle ground, semi-analytic models typically approximate the secular and long-period components of motion with analytic equations while using numerical integration to compute the short period components. For Space-Track objects, the Simplified General Perturbations 4 (SGP4) semi-analytic model is used in this research. For Vimpel objects, an in-house numerical propagator is used.

3.6.1 Simplified General Perturbation 4 (SGP4)

In Section 2.1, it is noted that Space-Track objects are given in two-line element (TLE) format. [36] explains that this format consists of mean object elements obtained through the removal of periodic variations in a specific manner. Thus, to accurately propagate a TLE object, these variations must be reconstructed in the same manner by which they were removed. The Simplified General Perturbations (SGP) family contains six models which are suitable for the reconstruction of TLE variations and the propagation of TLEs. They are SGP, SGP4, SDP4, SGP8, SDP8, and the new SGP4-XP model.

The first model, SGP, is an analytic propagator developed in 1966 by Hilton and Kuhlman for the propagation of near-Earth satellites [36]. By 1969, the number of cataloged space objects being propagated with SGP was too large for computers of the time to handle, so a simplification of the Lane and Cranford analytic theory was developed and implemented in 1970 [37]. This method, known as SGP4, is the primary method for near-Earth propagation. As objects with larger orbits around the Earth began to arise, a semi-analytic deep-space model was introduced. In 1977, the Simplified Deep Space 4 (SDP4) model, which includes lunar and solar gravitational effects and geopotential resonance effects for objects with periods greater than or equal to 225 minutes, was fully merged with the near-Earth SGP4 model to produce the SGP4 model used today [36] [37]. The SGP8/SDP8 methods were created to “alleviate deficiencies of SGP4/SDP4 for the special cases of orbital decay and reentry” [28], but there is no evidence suggesting these models are used for operational TLE formulations. The newest model, SGP4-XP, was briefed to the US Space Force on 7 February 2021. It uses improved and additional perturbation models of SRP, atmospheric drag, and deep space altitudes to obtain 1 to 2 orders of magnitude more accuracy than the current SGP4 routine used today while still maintaining comparable run times [38]. From these results, it is likely that the SGP4-XP routine will soon replace the current SGP4 routine for general TLE use.

The SGP4 routine used in this research was written by Vallado (2006). This routine is a hybrid SGP4/SDP4 routine that uses a near-Earth model for objects with periods less than 225 minutes and a deep-space model for objects with periods greater than or equal to 225 minutes. It works by taking in a TLE and propagation time and outputting a propagated object state in the TEME ECI frame referred to the epoch of the propagated state – Section 3.3.2.

3.6.2 Numerical Propagators

Before publishing a catalog, Vimpel propagates its objects to the ascending node closest to the published date. For its propagations, Vimpel uses a numerical propagator that takes into account “perturbations from the Earth’s gravitational field (geopotential harmonics up to the eighth inclusive), the gravitational field of the Moon and the Sun (as point-masses

in accordance with DE-405 model), the Earth’s atmosphere (in accordance with GOST R 25645.166-2004), [and] Sun radiation pressure” [27]. A numerical propagator developed in-house by the Space Information Dynamics (SID) group that takes into account the perturbations the Earth’s spherical harmonics (Equations 3.39–3.42; up to $l=4$, $m=4$), the Sun and Moon third body effects (Equation 3.45), drag (Equation 3.46; in accordance with the Jacchia 1970 density model [39]), and solar radiation pressure (Equation 3.47), is used to further propagate these Vimpel objects. Vimpel objects are given and propagated in the ECI frame with respect to the epoch J2000.

4. CATALOG CORRELATION THEORY

To correlate the US and Russian catalogs of space objects with each other and with observations, a modified nearest neighbor approach is taken. This section provides the theory behind this approach.

4.1 The Mahalanobis Distance

For this research, squared mahalanobis distances are used to correlate Vimpel objects to propagated Space-Track objects and optical observations to either catalog. The mahalanobis distance, d , is the number of standard deviations from a point, y , to a distribution. The distribution around a propagated catalog object is assumed to be a Gaussian, $N(\mu, \Sigma)$, ellipsoid as defined in Section 4.2, and the mahalanobis distance between y and $N(\mu, \Sigma)$ is taken from [40].

$$d = \sqrt{(y - \mu) \cdot \Sigma^{-1} \cdot (y - \mu)^T} \quad (4.1)$$

Squaring Equation 4.1 gives the md2, d^2 , equation.

$$d^2 = (y - \mu) \cdot \Sigma^{-1} \cdot (y - \mu)^T \quad (4.2)$$

4.2 Uncertainty Distributions

To use the squared mahalanobis distance, the covariance information for the propagated catalog objects is needed. Unfortunately, TLEs do not provide any covariance information and most (but not all) Vimpel objects come with a single positional in-track uncertainty value. Since the catalogs do not provide enough information to establish covariance matrices around the given states of their objects, this research seeks to establish viable covariance matrices around the final propagated states of these catalog objects. From [20], the largest uncertainty should be in the in-track direction of a spacecrafts ICO frame. To test this theory, and to determine an approximate covariance matrix for propagated catalog objects,

several Monte Carlo simulations were run. The first simulation was for 100 objects in a spherical $N(\mu, \Sigma)$ distribution. Using a two-body numerical propagator, these objects were propagated for a single 24 hour period and the characteristics were noted.

$$\mu = \begin{bmatrix} 42121.836 \text{ km} \\ 0 \\ 0 \\ 0 \\ 3.0777427 \text{ km/s} \\ 0 \end{bmatrix}_{ECI} \quad (4.3)$$

$$\Sigma = \begin{bmatrix} 100 \text{ km}^2 & 0 & 0 & 0 & 0 & 0 \\ 0 & 100 \text{ km}^2 & 0 & 0 & 0 & 0 \\ 0 & 0 & 100 \text{ km}^2 & 0 & 0 & 0 \\ 0 & 0 & 0 & 1 \text{ (m/s)}^2 & 0 & 0 \\ 0 & 0 & 0 & 0 & 1 \text{ (m/s)}^2 & 0 \\ 0 & 0 & 0 & 0 & 0 & 1 \text{ (m/s)}^2 \end{bmatrix}_{ECI} \quad (4.4)$$

Figure 4.1 shows that the initial spherical distribution elongates to an ellipsoidal distribution after the 24 hour propagation. As is the case from [20], the in-track direction contains the most uncertainty while the cross-track and out-of-plane directions have lower amounts of uncertainty. Figures 4.2 and 4.3 are from 24 hour Monte Carlo simulations similar to the initial simulation but with varying inclinations for the orbit. From these simulations it is found that changing the inclination has a very small effect on the shape and size of the final uncertainty distribution. When varying the time of propagation, or the initial position and velocity variance values, a much larger effect on the final distribution was obtained. Figure 4.4 is a 10 day Monte Carlo simulation for the 25° inclined initial GEO orbit, and it shows that as the propagation time increases, the uncertainty moves so far along the in-track direction that the shape is no longer ellipsoidal.

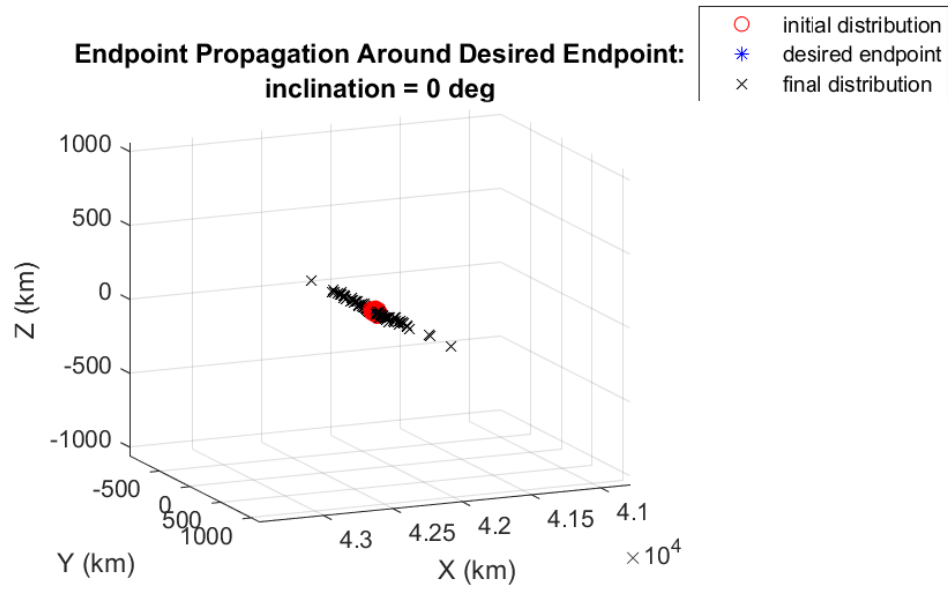


Figure 4.1. 1 day Monte Carlo GEO uncertainty simulation ($i = 0^\circ$, $n=100$)

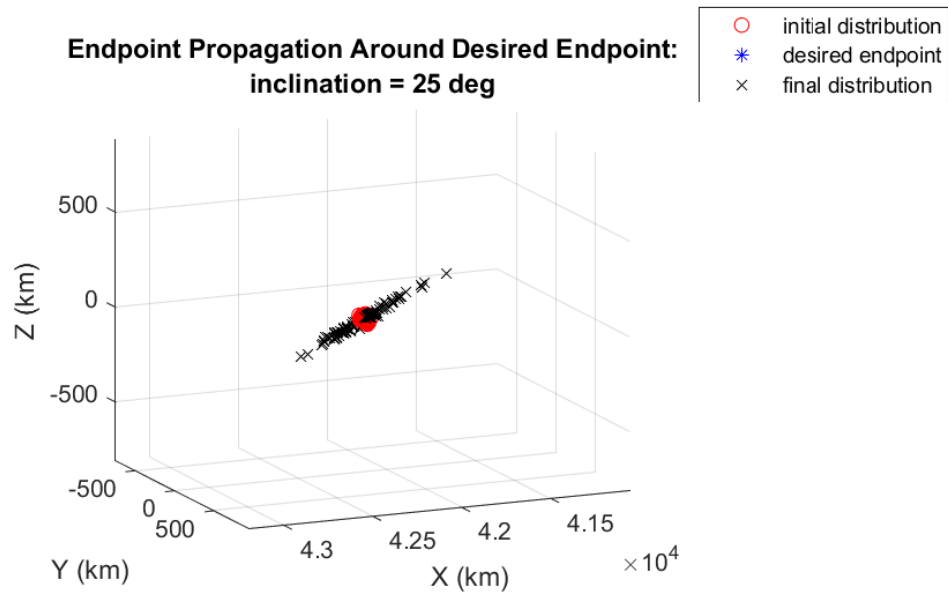


Figure 4.2. 1 day Monte Carlo GEO uncertainty simulation ($i = 25^\circ$, $n=100$)

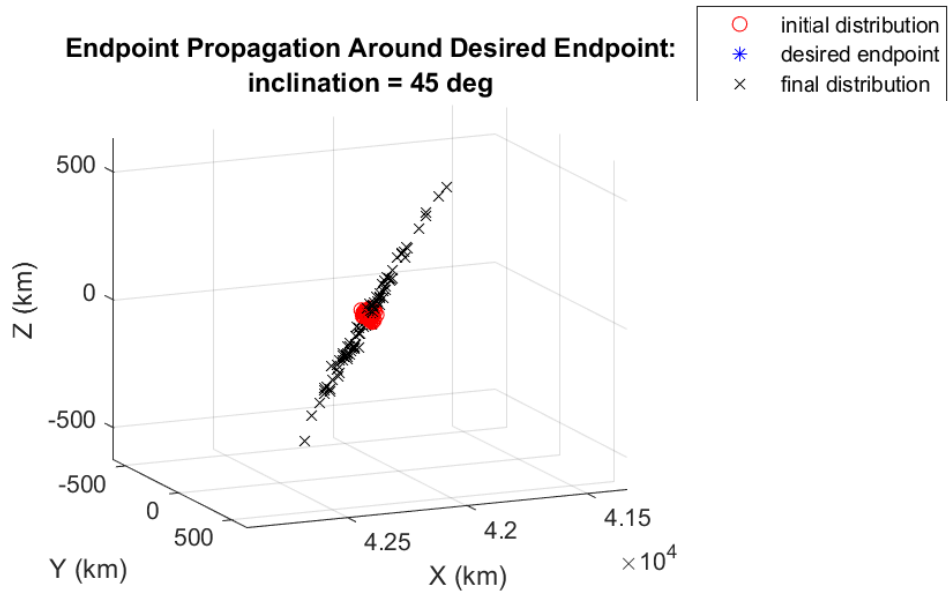


Figure 4.3. 1 day Monte Carlo GEO uncertainty simulation ($i = 45^\circ$, $n=100$)

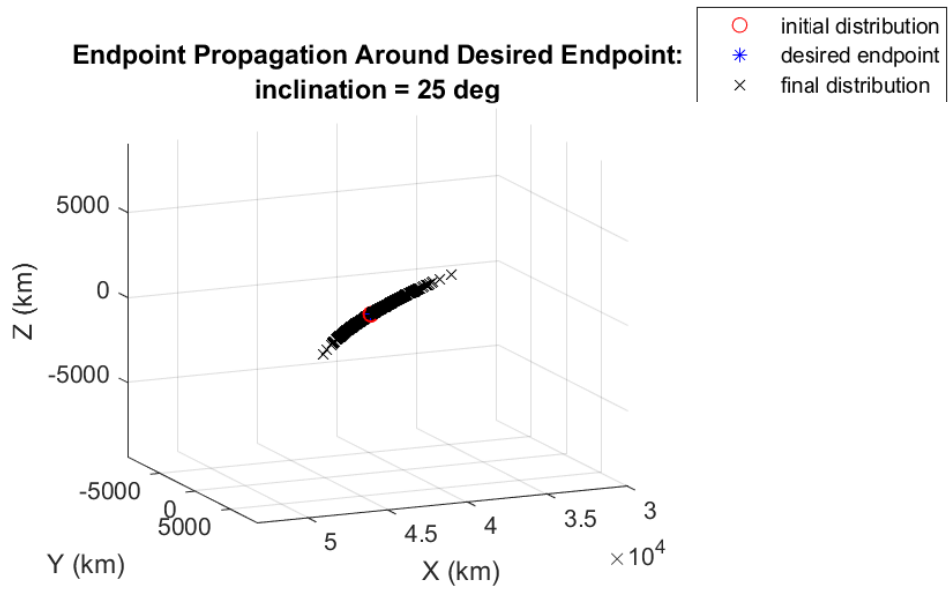


Figure 4.4. 10 day Monte Carlo GEO uncertainty simulation ($i = 25^\circ$, $n=1000$)

Figure 4.4 shows that the Gaussian assumption is only valid for short period propagations. A few more tests resulted in a valid Gaussian assumption for about 4 days of propagation using the same position and velocity standard deviations. For this research, the largest propagation times are about half a week. Therefore, the general assumption used in this research is that, for short period propagations, the uncertainty distribution of a propagated catalog object is Gaussian and ellipsoidal in nature with the largest uncertainty being in the in-track direction.

To determine the shape of the positional uncertainty ellipsoid, the ratios between the in-track standard deviation and the cross-track and out-of-plane standard deviations are calculated for each simulation. The ratio between the in-track and cross-track standard deviations is called the *itct* ratio, and the ratio between the in-track and out-of-plane standard deviations is called the *itoop* ratio. The covariance matrix is created by assigning an in-track standard deviation size term s and then dividing it by the the respective ratio to get the cross-track and out-of-plane standard deviations.

$$\Sigma_{ICO} = \begin{bmatrix} s^2 & 0 & 0 \\ 0 & (s/itct)^2 & 0 \\ 0 & 0 & (s/itoop)^2 \end{bmatrix} \quad (4.5)$$

To get the specific ratio values, a 1000 object, 24 hour Monte Carlo simulation for the 25° inclined Geosynchronous object scenario with position and velocity standard deviations of 10 km and 1 m/s, respectfully, is used. The values obtained from this simulation are:

$$itct = 5.608 \quad (4.6)$$

$$itoop = 5.663 \quad (4.7)$$

It is important to note that other values for these ratios would also work for the representation of the propagated uncertainty distribution. These ratios are solely two ratios which fit the criteria and work well for this research.

The size of the uncertainty distribution (the standard deviation, s , for the in-track term) is kept as the same parameter s for each propagated object. For the propagated Space-Track objects, their s term can be assumed to be equal since there is no uncertainty information is provided by TLEs. Unlike Space-Track, most Vimpel objects come with an in-track position uncertainty value which could be used as the value of s . However, some Vimpel objects do not come with this information. For the objects that do, this value ranges from a few kilometers for one object to hundreds of kilometers for another object. Therefore, to eliminate the potential bias posed by extremely large covariance matrices and remove the need to guess s values for the Vimpel objects with no given in-track uncertainty, the size of the covariance matrix for each Vimpel object is likewise set to the same parameter s . In the future, when more covariance information is known for the catalog objects, a numerical value can be given for s . Also, from Equations 4.1 and 4.5, s is seen to be inversely proportional to d . It is important to note that an s value is not required for this research as the main focus is to determine a “closest” object match. This closest match – and the match order – is only dependent on the shape of the uncertainty distribution when each catalog object has the same uncertainty distribution size.

In the direct catalog comparison method, the Space-Track objects are propagated to each Vimpel object and assigned an uncertainty distribution. Figure 4.5 is a scenario showing two propagated and transformed Space-Track objects with assigned covariance matrices near a Vimpel object projected into 2D space. In each image, the Space-Track objects have the same size and shape distributions with respect to their ICO frame. The top frame shows the Vimpel object’s position as inside the position distribution of Space-Track object 2, while being outside the distribution of Space-Track object 1. Therefore, Space-Track object 2 is more closely matched to the Vimpel object than Space-Track object 1. When the distribution sizes are reduced for the bottom frame, the match order remains the same.

To rotate the covariance matrix defined in Equation 4.5 to the ECI frame, a rotation matrix is built using the unit vectors of the ICO frame defined with respect to the ECI

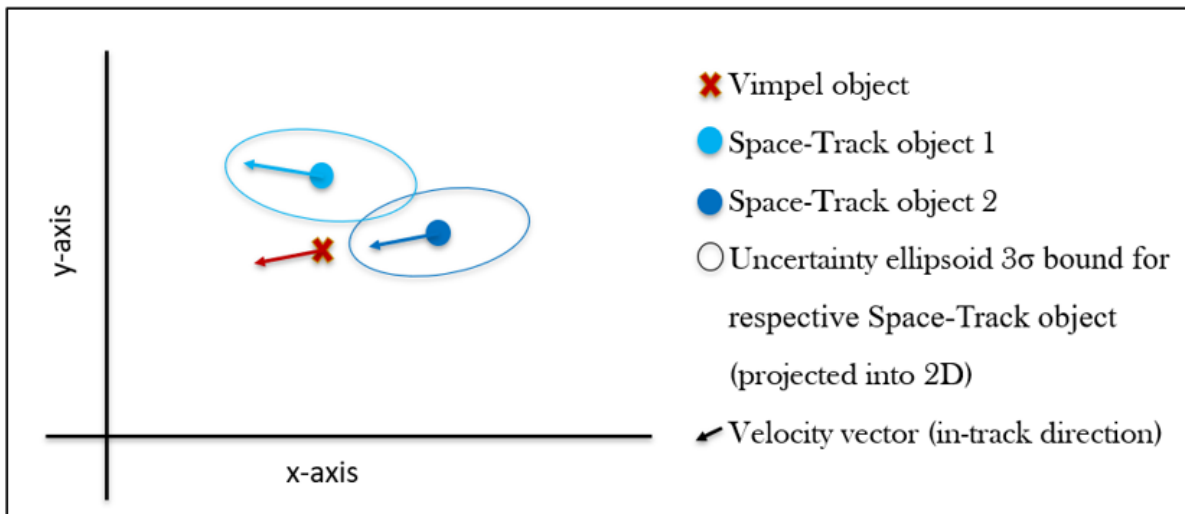
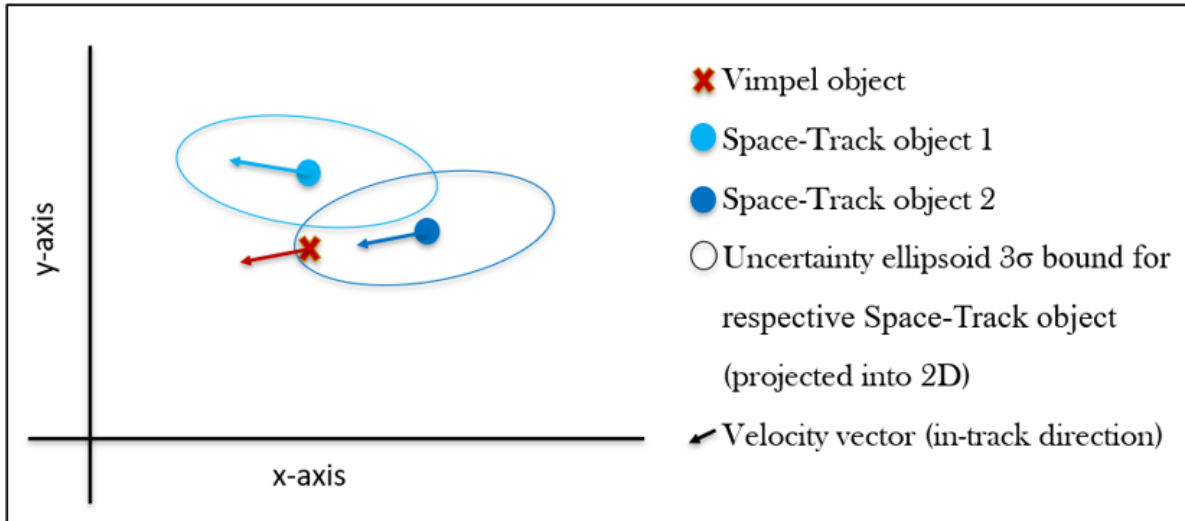


Figure 4.5. 2D projection of Gaussian ellipsoids – size comparison

frame. These unit vectors are obtained using the ECI position and velocity vectors for an object.

$$R = \begin{bmatrix} \text{in-track}_x & \text{cross-track}_x & \text{out-of-plane}_x \\ \text{in-track}_y & \text{cross-track}_y & \text{out-of-plane}_y \\ \text{in-track}_z & \text{cross-track}_z & \text{out-of-plane}_z \end{bmatrix} \quad (4.8)$$

$$\Sigma_{ECI} = R \Sigma_{ICO} R^T \quad (4.9)$$

4.3 ECI to Topocentric Equatorial Transformations

When using arc correlation to correlate catalog objects to optical observations, the propagated catalog object's Gaussian distributions need to be further transformed from the ECI frame to the 2D topocentric right ascension and declination frame.

To transform a catalog object's mean ECI position vector into a topocentric equatorial range, right ascension, and declination, the topocenter position vector needs to be known. In the case of spacecraft observations, the topocenter is an observation site. Using the local sidereal time of the observer (θ), the latitude of the observer (ϕ), and the magnitude of the site vector (R), an observation site position vector (\bar{R}_{eci}) can be calculated in the TOD ECI frame [29], and this vector can be transformed from TOD to J2000 using the methods described in Section 3.3.2.

$$\bar{R}_{eci} = \begin{bmatrix} R \cos(\phi) \cos(\theta) \\ R \cos(\phi) \sin(\theta) \\ R \sin(\phi) \end{bmatrix}_{ECI_TOD} \quad (4.10)$$

Using the position vector of the observation site in the J2000 ECI frame (\bar{R}_{eci}), a catalog object's mean ECI position vector ($\mu_{eci} = \bar{r}_{eci}$) can be transformed into its mean topocentric range vector ($\bar{\rho}_{eci}$).

$$\bar{\rho}_{\text{eci}} = \bar{r}_{\text{eci}} - \bar{R}_{\text{eci}} \quad (4.11)$$

$\bar{\rho}_{\text{eci}}$ can be represented as a vector in the ECI frame depicted by Figure 3.3.

$$\bar{\rho}_{\text{eci}} = x\hat{x} + y\hat{y} + z\hat{z} \quad (4.12)$$

Using this representation, $\bar{\rho}_{\text{eci}}$ can then be transformed into the range ρ , topocentric right ascension α' , and topocentric declination δ' spherical coordinates.

$$\rho = \sqrt{x^2 + y^2 + z^2} \quad (4.13)$$

$$\tilde{\rho} = \sqrt{x^2 + y^2} \quad (4.14)$$

$$\delta' = \frac{\pi}{2}, 0, -\frac{\pi}{2} \quad \text{for} \quad \tilde{\rho} = 0 \text{ and } z > 0, z = 0, z < 0 \quad (4.15)$$

$$\delta' = \arctan\left(\frac{z}{\tilde{\rho}}\right) \quad \text{for} \quad \tilde{\rho} \neq 0 \quad (4.16)$$

$$\alpha' = 0 \quad \text{for} \quad x = 0 \text{ and } y = 0 \quad (4.17)$$

$$\alpha' = \phi \quad \text{for} \quad x \geq 0 \text{ and } y \geq 0 \quad (4.18)$$

$$\alpha' = 2\pi + \phi \quad \text{for} \quad x \geq 0 \text{ and } y \leq 0 \quad (4.19)$$

$$\alpha' = \pi - \phi \quad \text{for} \quad x \leq 0 \quad (4.20)$$

$$\phi = \arctan\left(\frac{y}{x}\right) \quad (4.21)$$

For this research, the transformed ECI to topocentric equatorial mean of a catalog object distribution, $\mu_{\rho\alpha'\delta'}$, is defined as:

$$\mu_{\rho\alpha'\delta'} = \begin{bmatrix} \rho \\ \alpha' \\ \delta' \end{bmatrix}. \quad (4.22)$$

To transform the covariance matrix of a catalog object from the ECI frame (Σ_{ECI}) to the topocentric equatorial frame ($\Sigma_{\rho\alpha'\delta'}$), a linear transformation is used. To perform this transformation, the equations relating ρ , α' , and δ' to the components of $\bar{\rho}_{eci}$ (as defined by Equation 4.12) are taken from [29] and used to compute a Jacobian matrix – a matrix of partial first derivatives.

$$x = \rho \cos(\alpha') \cos(\delta') \quad (4.23)$$

$$y = \rho \sin(\alpha') \cos(\delta') \quad (4.24)$$

$$z = \rho \sin(\delta') \quad (4.25)$$

Using Equations 4.23–4.25, the the Jacobian matrix which linearly transforms a vector in the topocentric equatorial frame to the ECI frame is constructed.

$$J_{xyz} = \frac{\partial(x, y, z)}{\partial(\rho, \alpha', \delta')} = \begin{bmatrix} \frac{\partial x}{\partial \rho} & \frac{\partial x}{\partial \alpha'} & \frac{\partial x}{\partial \delta'} \\ \frac{\partial y}{\partial \rho} & \frac{\partial y}{\partial \alpha'} & \frac{\partial y}{\partial \delta'} \\ \frac{\partial z}{\partial \rho} & \frac{\partial z}{\partial \alpha'} & \frac{\partial z}{\partial \delta'} \end{bmatrix} \quad (4.26)$$

$$J_{xyz} = \begin{bmatrix} \cos(\alpha') \cos(\delta') & -\rho \sin(\alpha') \cos(\delta') & -\rho \cos(\alpha') \sin(\delta') \\ \sin(\alpha') \cos(\delta') & \rho \cos(\alpha') \cos(\delta') & -\rho \sin(\alpha') \sin(\delta') \\ \sin(\delta') & 0 & \rho \cos(\delta') \end{bmatrix} \quad (4.27)$$

Since the transformation needed is from the ECI frame to the topocentric equatorial frame, J_{xyz} is inverted.

$$J_{\rho\alpha'\delta'} = J_{xyz}^{-1} \quad (4.28)$$

$$\Sigma_{\rho\alpha'\delta'} = J_{\rho\alpha'\delta'} \Sigma_{ECI} J_{\rho\alpha'\delta'}^T \quad (4.29)$$

Equations 4.13–4.21 and 4.29 are used to transform a $N(\mu_{eci}, \Sigma_{ECI})$ ECI Gaussian ellipsoid into a $N(\mu_{\rho\alpha'\delta'}, \Sigma_{\rho\alpha'\delta'})$ topocentric equatorial Gaussian ellipsoid. Since the observations for this research are optical, 2D, (α', δ') pairs, the catalog object range information is unnec-

essary for the correlation process. Therefore, the 3D Gaussian $N(\mu_{\rho\alpha'\delta'}, \Sigma_{\rho\alpha'\delta'})$ is transformed into a 2D Gaussian $N(\mu_{\alpha'\delta'}, \Sigma_{\alpha'\delta'})$ retaining only the α' and δ' information.

$$\mu_{\alpha'\delta'} = \begin{bmatrix} 0 & 1 & 1 \end{bmatrix} \mu_{\rho\alpha'\delta'} \quad (4.30)$$

$$\Sigma_{\alpha'\delta'} = \begin{bmatrix} 0 & 1 & 0 \\ 0 & 0 & 1 \end{bmatrix} \Sigma_{\rho\alpha'\delta'} \begin{bmatrix} 0 & 0 \\ 1 & 0 \\ 0 & 1 \end{bmatrix} \quad (4.31)$$

4.3.1 Linear Covariance Matrix Transformation Validation

To verify the accuracy of the linear covariance matrix transformation, a Monte Carlo simulation is run to linearly (Equation 4.29) and non-linearly (Equations 4.13–4.21) transform a 3D uncertainty distribution for the GPS satellite NORAD 29486 (in a MEO orbit) from the 3D ECI frame to the 3D topocentric equatorial frame. Equations 4.30 and 4.31 are used to transform these points into the 2D topocentric right ascension (α') and declination (δ') frame. An initial Gaussian distribution for 100 km of in-track uncertainty in the ECI frame is shown in Figure 4.6 where the orange dot is the mean and the blue dots are simulated points in the distribution. Figure 4.7 shows these points linearly transformed from the 3D ECI frame to 2D topocentric frame. Figure 4.8 shows the linear transformed points overlayed by the true (non-linearly) transformed points. This figure shows that for 100 km of in-track uncertainty, the linear transformation is a very accurate representation of the actual uncertainty distribution in the topocentric frame. Figure 4.9 shows that even for an in-track uncertainty of 1000 km, the linear transformation still decently represents the actual uncertainty distribution. In Figure 4.10, it is seen that the linearly transformed covariance matrix is a very bad representation of the actual uncertainty distribution for an in-track uncertainty of 10000 km.

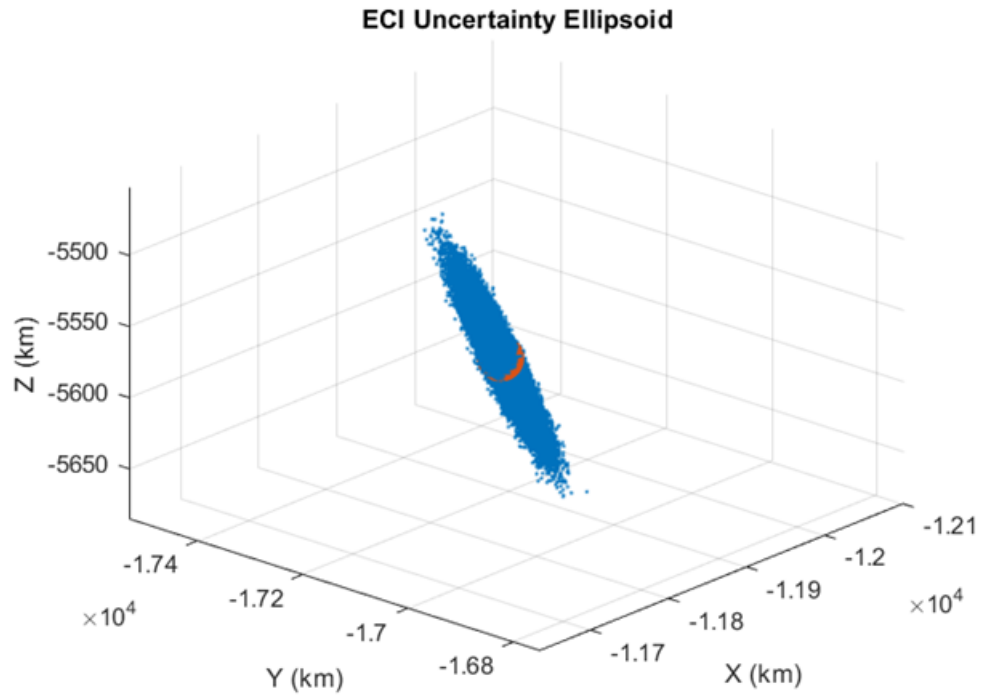


Figure 4.6. ECI uncertainty ellipsoid

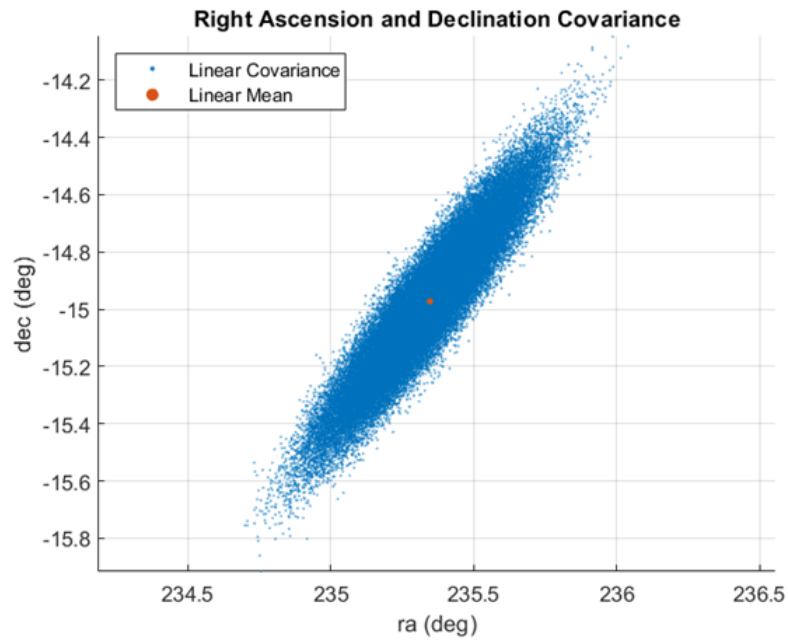


Figure 4.7. ra (α'), dec (δ') linear transformation

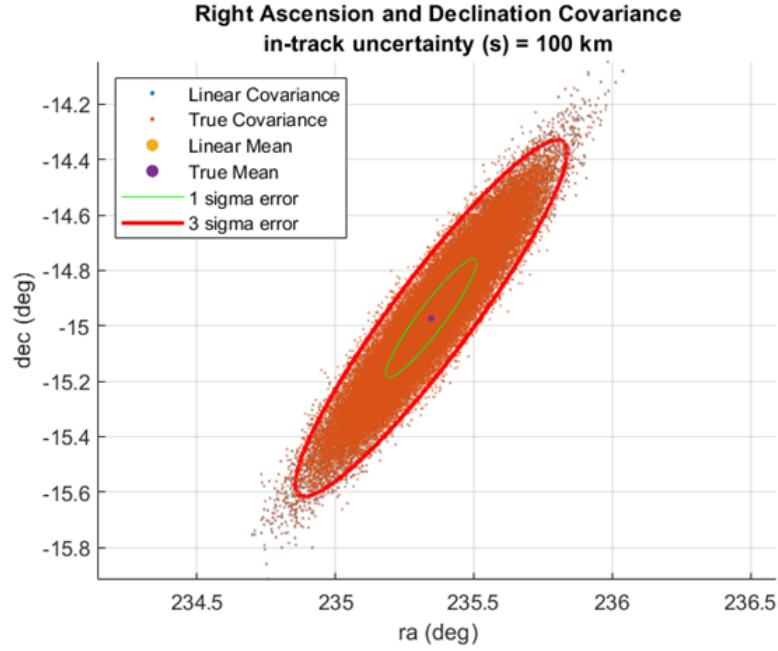


Figure 4.8. $ra (\alpha')$, $dec (\delta')$ linear vs true transformation: $s = 100$ km

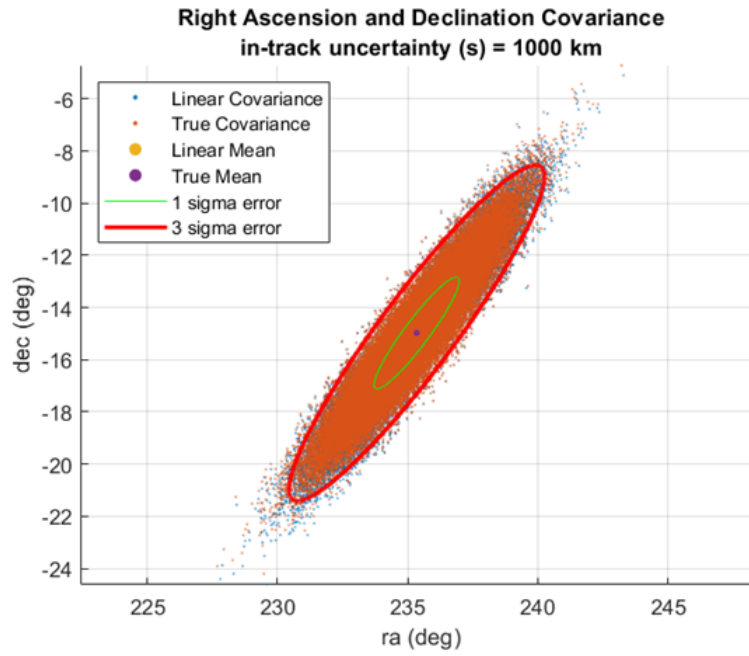


Figure 4.9. $ra (\alpha')$, $dec (\delta')$ linear vs true transformation: $s = 1000$ km

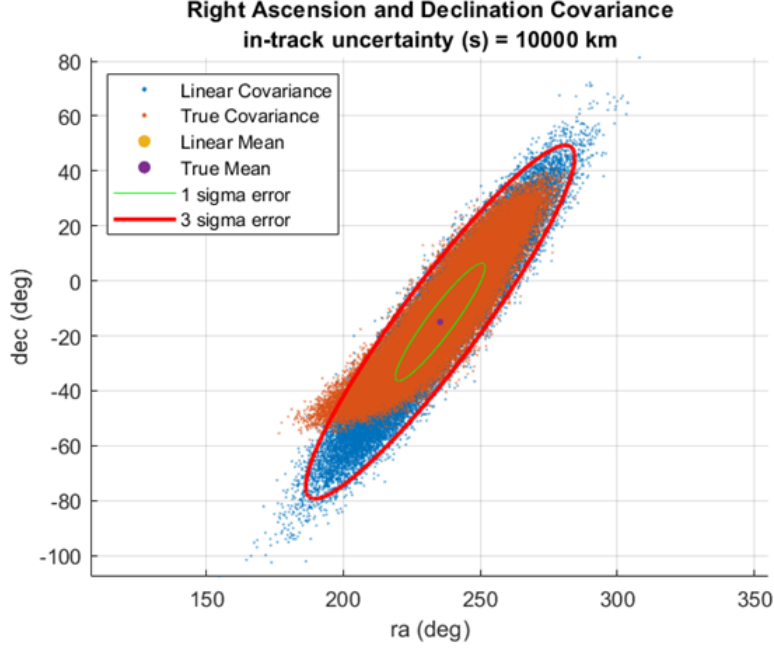


Figure 4.10. ra (α'), dec (δ') linear vs true transformation: $s = 10000$ km

For this research, it is assumed that the in-track uncertainty will be less than 1000 km, and Figures 4.11 and 4.12 show further testing for an s of 1000 km for LEO and GEO objects. From these figures, and from Figure 4.9, it is assumed that a linearly transformed covariance matrix is a good representation of the true uncertainty distribution for an object in the topocentric frame. These assumptions are reasonable since the average in-track uncertainty given for a Vimpel object is less than 100 km, and [20] states that GEO and HEO TLEs have an average of 25 and 35 km of in-track uncertainty, respectfully.

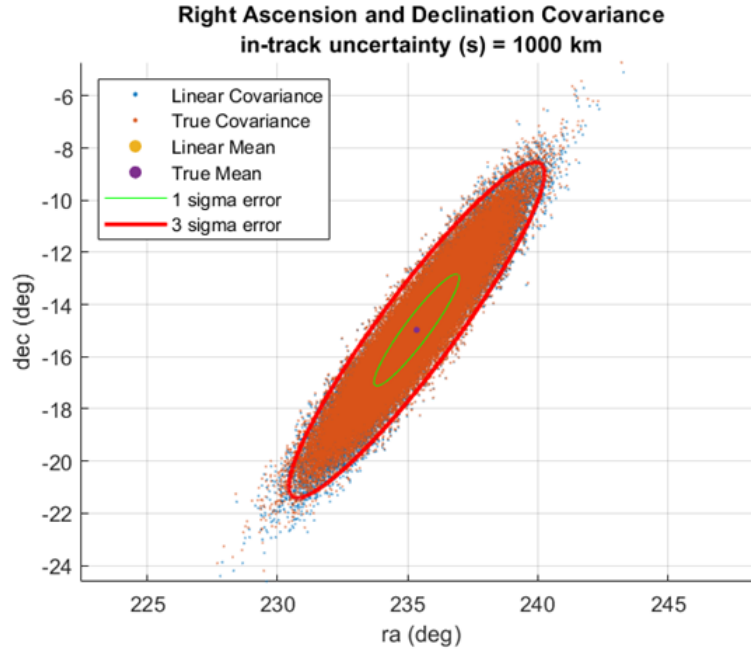


Figure 4.11. LEO object (ISS – NORAD 25544) ra (α'), dec (δ') linear vs true transformation: $s = 1000$ km

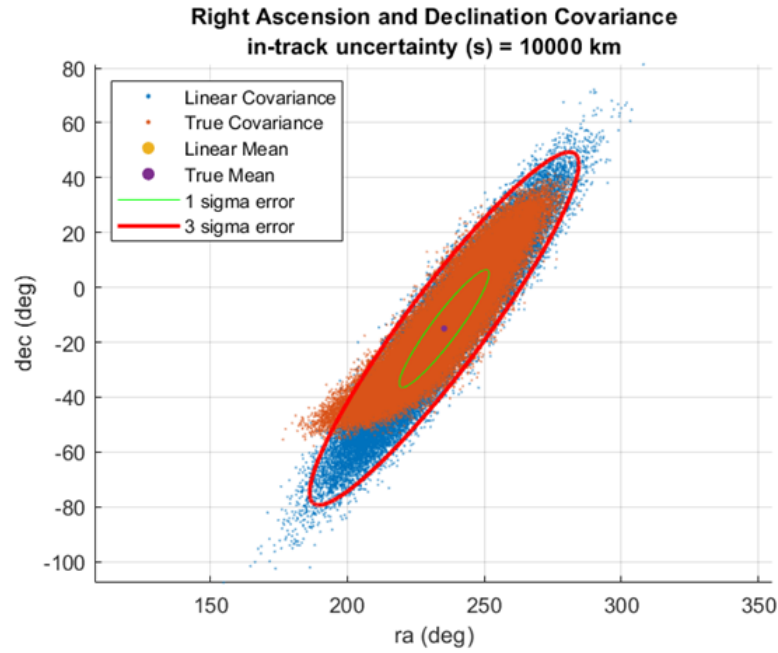


Figure 4.12. GEO object (WGS 9 – NORAD 42075) ra (α'), dec (δ') linear vs true transformation: $s = 1000$ km

4.4 The Topocentric Right Ascension Rate and Declination Rate Frame

Another frame used for the comparison of optical observations to catalog objects is the topocentric right ascension rate, $\Delta\alpha'$, and declination rate, $\Delta\delta'$, frame. This frame is created between two observations in an observation set by subtracting the first observation from the second observation. To illustrate this frame, Figures 4.13 and 4.14 show two consecutive observations from a set in the α' , δ' frame that are subtracted from each other to obtain velocity observations and distributions in the $\Delta\alpha'$, $\Delta\delta'$ frame.

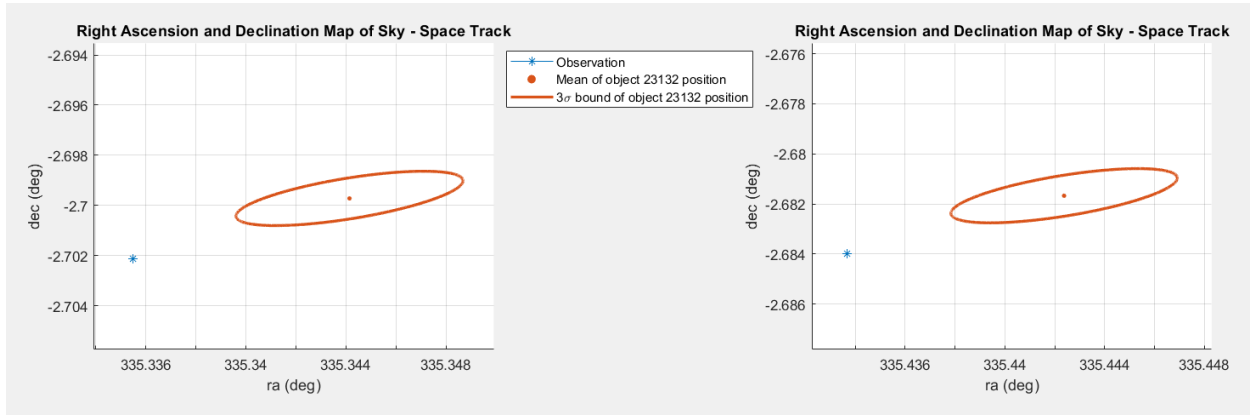


Figure 4.13. Two observations with one potential Space-Track object in the α' , δ' frame

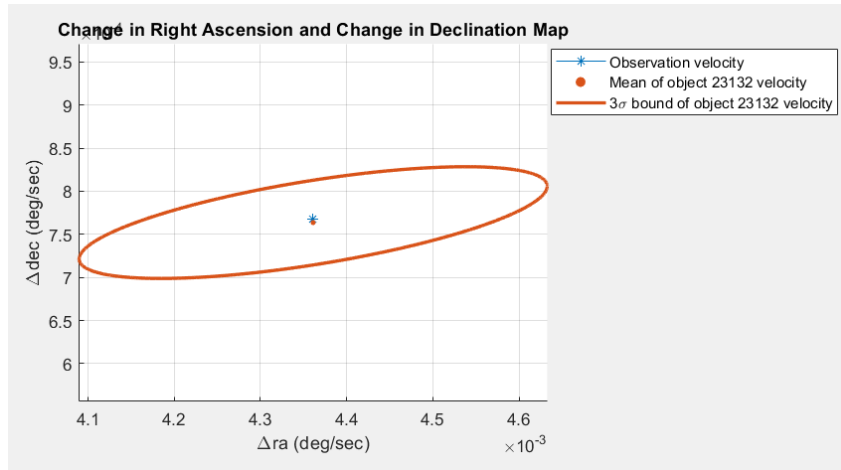


Figure 4.14. Change between the two observations in Figure 4.13 in the $\Delta\alpha'$, $\Delta\delta'$ frame

To compute the velocity, v_{obs} , of an observed object between two observations in the $\Delta\alpha'$, $\Delta\delta'$ frame, the first optical observation, $y_{obs1} = (\alpha'_{obs1}, \delta'_{obs1})$, is subtracted from the second optical observation, $y_{obs2} = (\alpha'_{obs2}, \delta'_{obs2})$.

$$\Delta\alpha'_{obs} = \alpha'_{obs2} \cos(\delta'_{obs2}) - \alpha'_{obs1} \cos(\delta'_{obs1}) \quad (4.32)$$

$$\Delta\delta'_{obs} = \delta'_{obs2} - \delta'_{obs1} \quad (4.33)$$

$$v_{obs} = (\Delta\alpha'_{obs}, \Delta\delta'_{obs})/\Delta t \quad (4.34)$$

Δt is the change in time between the two observations. For subtracting catalog object distributions between the two observations – where $N(\mu_{\alpha'\delta'1}, \Sigma_{\alpha'\delta'1})$ and $N(\mu_{\alpha'\delta'2}, \Sigma_{\alpha'\delta'2})$ are the distributions for an object in the first and second observations, respectfully – the equations for subtracting random variables from page 381 in [41] are used.

$$\mu_{\Delta\alpha'\Delta\delta'} = \mu_{\alpha'\delta'2} - \mu_{\alpha'\delta'1} \quad (4.35)$$

$$\Sigma_{\Delta\alpha'\Delta\delta'} = \Sigma_{\alpha'\delta'2} + \Sigma_{\alpha'\delta'1} \quad (4.36)$$

To obtain velocity values, Equations 4.35 and 4.36 are modified to account for the change in time between the observations.

$$\mu_{\Delta\alpha'\Delta\delta'} = (\mu_{\alpha'\delta'2} - \mu_{\alpha'\delta'1})/\Delta t \quad (4.37)$$

$$\Sigma_{\Delta\alpha'\Delta\delta'} = (\Sigma_{\alpha'\delta'2} + \Sigma_{\alpha'\delta'1})/\Delta t^2 \quad (4.38)$$

4.5 Likelihoods and Log Likelihoods

The likelihood, L , is defined as the likeliness of a point belonging to a distribution. It is indirectly related to the cumulative distribution function, F , of the point.

$$L = 1 - F \quad (4.39)$$

In this research, the likelihood is used to measure how likely a catalog object is to being the observed object in an observation set. Individual position and velocity likelihoods are calculated in the α' , δ' and $\Delta\alpha'$, $\Delta\delta'$ frames, respectfully, and both of these frames are in two dimensions with the catalog objects being modeled as 2D Gaussian distributions. For a 2D Gaussian distribution, [42] shows that the cumulative distribution function, F , for a point can be represented as a function of its mahalanobis distance, d . Therefore, the likelihood can also be represented as a function of the Mahalanobis distance.

$$F = 1 - e^{-d^2/2} \quad (4.40)$$

$$L = e^{-d^2/2} \quad (4.41)$$

To mitigate the effects of large squared mahalanobis distance values, log likelihoods are used and converted back to likelihoods when necessary. The log likelihood, l , is simply the natural log of Equation 4.41, and like the squared mahalanobis distance, l is also inversely proportional to s^2 .

$$l = \ln(L) = \frac{-d^2}{2} \quad (4.42)$$

$$L = e^l \quad (4.43)$$

$$l \propto \frac{1}{s^2} \quad (4.44)$$

4.6 Two-Body Least Squares

Later in this research, a two-body least squares algorithm is used to take tracklets of observations which might pertain to the same catalog object and see if a two-body orbit can be fit to them. To use this algorithm, an initial orbit is determined using the potential catalog object. Next, the optical observations given in the tracklets are used together to iteratively improve the initial orbit using a batch least squares (LUMVE) method as defined in [29] from pages 183 to 201. Two variables λ and Λ are used to update the initially determined orbit.

$$\lambda = \lambda + H^T R^{-1} \delta z \quad (4.45)$$

$$\Lambda = \Lambda + H^T R^{-1} H \quad (4.46)$$

For this least squares algorithm, no prior information is assumed, so the initial λ and Λ values are set to a 6x1 zero vector and a 6x6 matrix of zeros, respectfully. H is the multiplication of the measurement mapping matrix and the state transition matrix at the k^{th} observation time, R is the least squares weighting matrix for an assumed noise of 2 arcseconds,

$$R = \begin{bmatrix} 2^2 & 0 \\ 0 & 2^2 \end{bmatrix}^{-1}, \quad (4.47)$$

and δz is the difference between the k^{th} observation and the reference state measurement at the time of the k^{th} observation. After λ and Λ are computed and updated using all of the observations, a batch update of the orbit state, \hat{x} , and covariance, P , is performed.

$$\delta \hat{x} = \Lambda^{-1} \lambda \quad (4.48)$$

$$\hat{x} = \hat{x} + \delta\hat{x} \tag{4.49}$$

$$P = \Lambda^{-1} \tag{4.50}$$

Since the least squares algorithm is not guaranteed to converge, a fixed number of iterations (seven for this research) are used to update the initial orbit state with observations. This final orbit is then marked as either determined or undetermined.

5. CATALOG CORRELATION METHODS

Two methods of catalog correlation are constructed in this thesis. The first method directly compares Space-Track objects to Vimpel objects, using multiple filters to determine the closest object pairing. The second method uses arc correlation to match optical observations to each catalog. These methods are validated against the `datefirst.txt` file.

5.1 Method 1: Direct Catalog Comparison

To directly and efficiently compare Space-Track objects to Vimpel objects, the method outlined below is used.

1. Download a pair of Space-Track and Vimpel catalogs
2. Split the catalogs into buckets based on orbital regimes
3. Determine the closest Space-Track object to each Vimpel object for a bucket

5.1.1 Download Space-Track and Vimpel Catalogs

The first step is to download the catalogs of space objects. Tomoki Koike, a 2021 Purdue graduate, developed code to query the Space-Track and Vimpel catalog websites – `space-track.org` and `spacedata.vimpel.ru` – for recent catalogs. This code is modified and used to pull Space-Track and Vimpel catalogs referenced to a specific date. Since Vimpel catalogs are published weekly, downloading the Vimpel catalog pertaining to a specific date is simply a matter of choosing the catalog published closest to that date. Unlike Vimpel, the Space-Track catalog is continuously updated, and the only “published” catalog is the catalog containing the most recent TLEs for each object. To obtain a Space-Track catalog referenced to a specific date, a search is performed which collects all the TLEs generated up to three days prior to the desired date. For each object, its closest TLE to the date is kept and all others are thrown out. Lastly, Space-Track and Vimpel catalogs pertaining to the same date are downloaded and compared in order to minimize the propagation error. For this research, 99 catalog pairs ranging from January of 2019 to December of 2021 are downloaded and

compared. Also, since the Space-Track and Vimpel catalogs are pulled and compared with respect to the same reference date, the largest propagation time for any of the Space-Track object to the Vimpel object will be no longer than a few days, with most propagations being less than a day. Therefore, the covariance matrix for a propagated Space-Track object in this method can be assumed to be ellipsoidal.

5.1.2 Split Catalogs into Buckets

As of 2021, a full Space-Track catalog contains about 25000 objects and a full Vimpel catalog contains about 7000 objects. Comparing 25000 Space-Track objects to 7000 Vimpel objects results in 175 million comparisons. One way to reduce the number of comparisons is to group the catalog objects into buckets based on their orbital regime. Since most Space-Track objects are in near-Earth orbits and most Vimpel objects have periods greater than 200 minutes, this grouping results in many near-Earth Space-Track objects being compared to only a few near-Earth Vimpel objects and vice versa.

Therefore, the next step after downloading and selecting a Space-Track and Vimpel catalog pair is to split the catalogs into buckets based on the orbital regimes. Five buckets are used in this research. The first four buckets contain objects which fit into the LEO, Mid-Earth Orbit (MEO), GEO/Geosynchronous Orbit, and High-Eccentricity Orbit (HEO) regimes. The last bucket contains all objects which do not fit into any of the first four buckets. The buckets are defined with respect to an object's perigee and apogee altitudes.

1. LEO bucket – perigee ≥ 80 km, apogee < 2000 km
2. MEO bucket – perigee ≥ 2000 km, apogee < 36000 km
3. GEO bucket – perigee ≥ 35586 km, apogee < 35986 km
4. HEO bucket – perigee < 2000 km, apogee > 35000 km
5. Other bucket – all objects which don't meet the above criteria

The perigee/apogee bounds for the LEO, MEO and HEO buckets are obtained from [43]. The listed average perigee and apogee altitudes for HEO objects are 1000 km and 36000

km, respectfully, but a 1000 km buffer is added to catch any slightly less than average HEO objects. The GEO/Geosynchronous bounds are obtained from [29], and any objects placed into the GEO bucket are excluded from the MEO bucket. Using these buckets, the number of necessary Space-Track to Vimpel comparisons is reduced by an order of magnitude – from about 175 million comparisons to less than 12 million comparisons. A source of error that comes with using these buckets is the chance for two Space-Track and Vimpel catalog objects which pertain to the same space object to be sorted into two different buckets. This error could happen if the perigee/apogee values for these catalog objects border the bounds between buckets, and the possibility for this error will increase as the number of buckets increase.

5.1.3 Match Space-Track Objects to Vimpel Objects – Within a Bucket

After splitting the catalogs into buckets, a bucket is chosen to be compared (e.g. the GEO bucket). For each Vimpel object in a chosen bucket, all of the Space-Track objects in the same bucket are propagated to the reference time of the Vimpel object. The Space-Track objects are then transformed from the TEME ECI frame to the J2000 ECI frame as described in Section 3.3.2 and put through two filters to match the most likely Space-Track object to the Vimpel object.

Filter 1: Squared Mahalanobis Distance (Md2) Filter

The first filter calculates a positional squared mahalanobis distance (md2) between each Space-Track object and the Vimpel object. To compute this distance, an ellipsoidal covariance matrix with a constant size s is built around each propagated Space-Track object in the J2000 ECI frame as described by Equations 4.5–4.9. Equation 4.2 is then used to calculate positional d^2 values for each Space-Track object where y is the position vector of the Vimpel object, μ is the position vector of the Space-Track object, and Σ is the covariance matrix of the Space-Track object. Once a md2 value is computed for each Space-Track object, the objects with md2 values below a chosen md2 threshold are marked as potential matches and put through a second filter to match a single Space-Track object to the Vimpel object.

Squared Mahalanobis Distance (Md2) Threshold

The md2 threshold is defined as the largest md2 a Space-Track object can have from a Vimpel object and still be considered a potential match. Since the second filter used to match a Space-Track object to a Vimpel object is more robust, the md2 threshold is set so a feasible number of potential Space-Track object matches are run through the second filter. If this threshold was set to infinity, all the Space-track objects in the bucket would be potential matches for the Vimpel object – ordered from closest to furthest with respect to their md2s. Figure 5.1 shows the case where the md2 threshold is set to infinity for the GEO bucket. (The notably larger purple sphere in the center is the Earth)

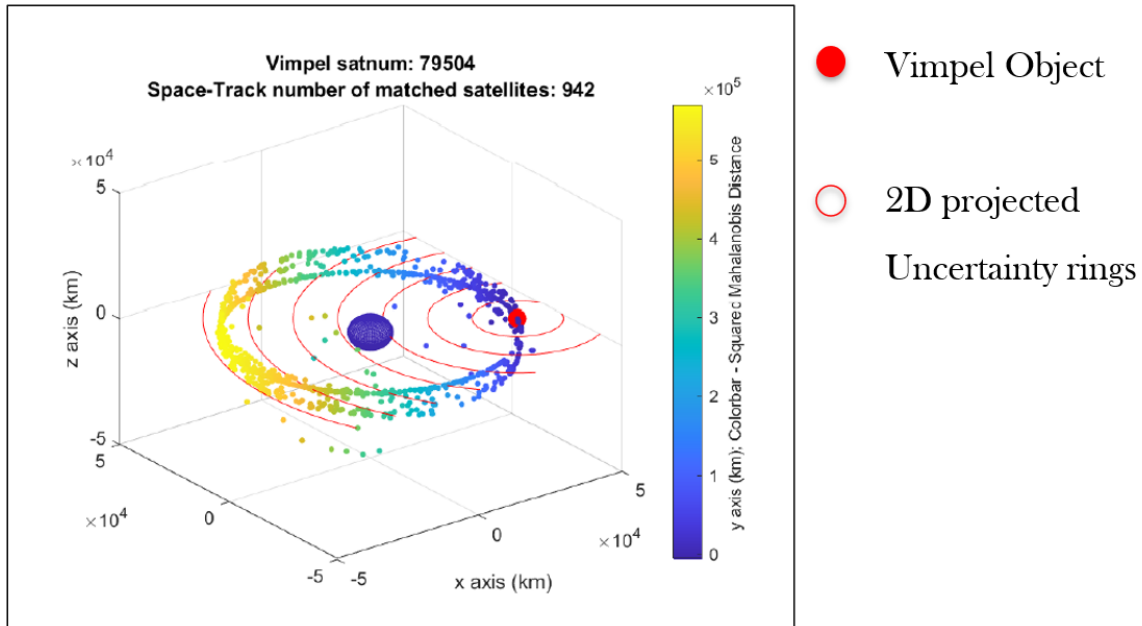


Figure 5.1. Md2 threshold set to ∞ – case for a Vimpel object 79504

For this research, the md2 threshold is chosen to be $1 \times 10^6/s^2$. If no Space-Track objects have md2s below this threshold, then the Vimpel object is said to be “unmatched” to the Space-Track catalog. This threshold is found to retain a sufficient level of potential Space-Track matches; however, more testing would be necessary to find the best threshold value for direct catalog comparison.

Filter 2: Classical Orbital Element (COE) Filter

Once all the potential Space-Track matches are identified for a Vimpel object, the orbital elements of these potential matches are compared to those of the Vimpel object using a COE filter. This filter draws upon the work of [18] and has the following steps:

1. Compute the six classical orbital elements (COEs – described in Section 3.4) for each potential Space-Track object
2. Establish five correlation parameters based on the COEs
3. For each Space-Track object, compute the error between its parameters and the Vimpel object’s parameters
4. Normalize the error for each correlation parameter
5. Compute a confidence value for each normalized parameter error
6. Compute coplanar (C_p), co-orbital (C_o), and same object (C_s) confidence levels
7. Scale the C_s by the mahalanobis distance of the potential Space-Track object to get a C_{s_scaled} value
8. Match the Space-Track object with the largest C_{s_scaled} value to the Vimpel object

The first step is to take the potential Space-Track objects labeled by the md2 filter and compute their six classical orbital elements (a [m], e , i [rad], Ω [rad], ω [rad], ν [rad]). Using these elements, five correlation parameters are established:

- a : semi-major axis [m]
- e : eccentricity
- i : inclination [rad]
- Ω : right ascension of the ascending node (raan) [rad]
- $\lambda = \omega + \nu$: argument of perigee + true anomaly [rad]

The first four parameters used are just the first four COEs. The fifth parameter combines the argument of perigee and the true anomaly is used to reduce the error when comparing nearly circular orbits. Step three is to compute the error between the correlation parameters for the Space-Track (st) and Vimpel (v) objects.

$$\Delta x = |x_{\text{st}} - x_{\text{v}}|; x = (a, e, i, \Omega, \lambda) \quad (5.1)$$

To normalize the parameter error, Δa is divided by 6,378,140 meters (the radius of the Earth) and Δi , $\Delta \Omega$, and $\Delta \lambda$ are divided by 2π radians. A confidence value (ranging from [0.001, 1]) for each parameter is computed using the normalized errors.

$$C_x = \frac{1}{1 + 999 \cdot \Delta x}; x = (a, e, i, \Omega, \lambda) \quad (5.2)$$

Using these confidence parameter values, coplanar (C_p), co-orbital (C_o), and same object (C_s) confidence values are computed (ranging from $[1 \times 10^{-9}, 1]$). The coplanar confidence value is based off of the inclination and raan confidence values because these COEs define the plane of an orbit. A small difference between the inclinations and raans of the Space-Track and Vimpel objects will result in a high coplanar confidence value. A Space-Track object in the same orbit as a Vimpel object – but not necessarily in the same location on the orbit – will be in the same orbital plane with the same size and shape orbit. Therefore, the co-orbital confidence level is based off of the semi-major axis and eccentricity COEs along with the coplanar confidence level. The same object confidence level uses the co-orbital confidence and the λ value – the spacecrafts angular position in its orbit – to determine the confidence of the Space-Track and Vimpel objects being the same object.

$$C_p = \frac{1}{2}(C_i + C_\Omega) \quad (5.3)$$

$$C_o = C_p \cdot \frac{1}{3}(C_p + C_a + C_e) \quad (5.4)$$

$$C_s = C_o \cdot \frac{1}{2}(C_o + C_\lambda) \quad (5.5)$$

For this research, the C_s value is taken since this filter is being used to match the same objects between the Space-Track and Vimpel catalogs. The last step is to take this C_s value for a Space-Track object and weight it by its mahalanobis distance. This weighting allows the mahalanobis distance information from the md2 filter to be retained in the COE filter.

$$C_{s_scaled} = \frac{C_s}{d} \quad (5.6)$$

The potential Space-Track object with the largest C_{s_scaled} value is matched to the Vimpel object.

5.2 Method 2: Optical Observation Correlation

The optical observation correlation method focuses on taking sets of optical observations (tracklets) and correlating them to both the Space-Track and Vimpel catalogs. Through matching observed objects to each catalog, the catalog objects themselves can be correlated. This method takes in an observation set and outputs a log likelihood, l_{OS} , value for each potential object match sorted from most likely to least likely. The most likely object for each catalog is “matched” as the object being observed by the tracklet, and the full process is outlined below.

1. Pull catalogs closest in date to the time of the first observation in a set
2. Determine potential catalog object matches for the observation set
3. Calculate a log likelihood value for each potential object
4. Match the potential object with the highest likelihood

5.2.1 Pull Close Catalogs

Section 5.1.1 describes how this research acquires Space-Track and Vimpel catalogs. Each downloaded catalog comes with an associated date that the catalog is referenced to, and pulling the catalogs referenced to dates closest to the Julian Date of the first observation in

a set reduces the propagation time for each catalog object. Reducing the propagation time should increase the accuracy since shorter propagation times should result in less propagation error. This research uses the Space-Track and Vimpel catalog pairs discussed in Section 5.1, and these pairs are spaced out in weekly intervals. Therefore, the longest propagation time for any catalog object in this algorithm should be about half a week. This propagation time falls within the definition of a short period propagation from Section 4.2, which means the covariance matrices assigned to propagated Space-Track and Vimpel objects can be assumed to be Gaussian ellipsoids. The next steps in the method are performed separately for the Space-Track and Vimpel catalogs.

5.2.2 Determine Potential Catalog Object Matches

To determine a potential catalog object match for an observation, each object is propagated to the observation time, transformed into the J2000 ECI frame if necessary, and assigned a Gaussian uncertainty ellipsoid in the ECI frame, $N(\mu_{eci}, \Sigma_{ECI})$. From here, the catalog objects are transformed into the same frame as the observations – the topocentric right ascension and declination frame – as described in Section 4.3. Once all the catalog objects are represented as 2D $N(\mu_{\alpha'\delta'}, \Sigma_{\alpha'\delta'})$ Gaussian distributions, a positional squared mahalanobis distance, d_p^2 , is calculated from each catalog object to the observation, y_{obs} . The objects with md2s less than the chosen threshold of $1 \times 10^6/s^2$ (the same threshold chosen in Section 5.1.3) are marked as potential matches for an observation. Figure 5.2 shows an observation with its potential Space-Track objects in the α' , δ' frame.

$$d_p^2 = (y_{obs} - \mu_{\alpha'\delta'}) \cdot \Sigma_{\alpha'\delta'}^{-1} \cdot (y_{obs} - \mu_{\alpha'\delta'})^T \quad (5.7)$$

Lastly, the potential matches for an observation set are just the combined potential matches for all of the observations in the set.

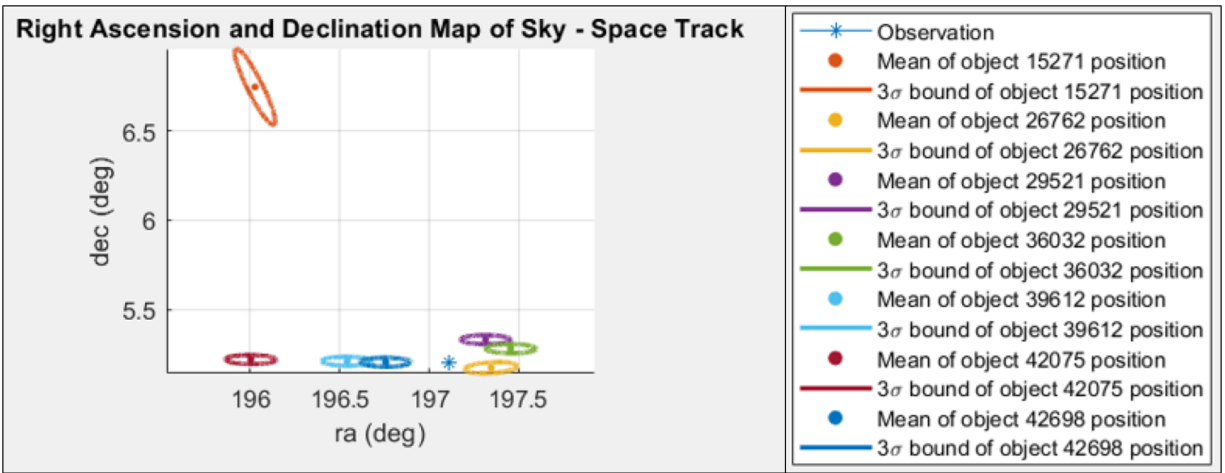


Figure 5.2. Space-Track potential matches for an observation

5.2.3 Calculate Log Likelihoods for Potential Objects

For each potential object in an observation set, an observation set log likelihood, l_{OS} , is calculated. The l_{OS} is a measure of how likely a catalog object is to being the observed object in the set, and it ranges from $(-\infty, 0]$. To calculate the l_{OS} , a series of position and velocity log likelihoods are used. For each object, a position log likelihood is calculated for each observation in the set and a velocity log likelihood is calculated for each consecutive pair of observations. So, if there are six observations (labeled 1 through 6) in a set, there will be six position log likelihoods $[l_1, l_2, l_3, l_4, l_5, l_6]$ and five velocity log likelihoods $[l_{1:2}, l_{2:3}, l_{3:4}, l_{4:5}, l_{5:6}]$. Position and velocity log likelihoods are calculated using Equation 5.2.3 where d^2 is the position or velocity md2 value, respectfully. Position log likelihoods are represented as l_i ; ($i = 1, \dots, n$), where n is the number of observations in a set. To calculate l_i for a catalog object, $N(\mu_{\alpha'\delta'}, \Sigma_{\alpha'\delta'})$, with respect to an optical observation, y_{obs} , a positional md2 value, d_p^2 , is calculated using Equation 5.7 and plugged into Equation 4.42.

$$l_i = \frac{-d_p^2}{2} \quad (5.8)$$

Velocity log likelihoods are represented as $l_{i:i+1}$; ($i = 1, \dots, n-1$), where n is the number of observations in a set. To calculate $l_{i:i+1}$ for a catalog object, two consecutive observations are subtracted to find an observation velocity, v_{obs} , and a catalog object velocity distribution, $N(\mu_{\Delta\alpha'\Delta\delta'}, \Sigma_{\Delta\alpha'\Delta\delta'})$, in the $\Delta\alpha'$, $\Delta\delta'$ frame – as described in Section 4.4. Next, the v_{obs} , $\mu_{\Delta\alpha'\Delta\delta'}$, and $\Sigma_{\Delta\alpha'\Delta\delta'}$ values are plugged into Equation 4.2 to determine a velocity md2 value, d_v^2 . Then, by inputting d_v^2 into Equation 4.42, the velocity log likelihood is calculated.

$$d_v^2 = (v_{obs} - \mu_{\Delta\alpha'\Delta\delta'}) \cdot \Sigma_{\Delta\alpha'\Delta\delta'}^{-1} \cdot (v_{obs} - \mu_{\Delta\alpha'\Delta\delta'})^T \quad (5.9)$$

$$l_{i:i+1} = \frac{-d_v^2}{2} \quad (5.10)$$

Using all of the position and velocity log likelihoods for a catalog object in an observation set, the observation set log likelihood, l_{OS} , can be computed. The l_{OS} is computed by taking

the average of the mean position log likelihood, l_p , and mean velocity log likelihood, l_v . These log likelihoods are computed for the n -observation case.

$$l_p = \frac{\sum_{i=1}^n l_i}{n} \quad (5.11)$$

$$l_v = \frac{\sum_{i=1}^{n-1} l_{i:i+1}}{n-1} \quad (5.12)$$

$$l_{OS} = \frac{l_p + l_v}{2} \quad (5.13)$$

Tracking Data Message (TDM) Likelihood

Most of the data used to validate and test this algorithm is provided in Tracking Data Messages (TDMs) from the German Aerospace Center (DLR). TDMs contain many observation sets that usually pertain to a single object. For each TDM, a TDM log likelihood, l_{TDM} , can be computed for each potential catalog object. The l_{TDM} is a measure of how likely a catalog object is to being the observed object when taking into account all of the observation sets in the TDM. It is computed by taking the average of all the object's observation set log likelihoods in the TDM. The calculation of a TDM log likelihood for an object is shown for the j -observation set case.

$$l_{TDM} = \frac{\sum_{i=1}^j l_{OS_i}}{j} \quad (5.14)$$

Something to note is that all the log likelihoods calculated in this research maintain the inverse relationship to s^2 shown in Equation 4.44.

5.2.4 Match the Potential Object with the Highest Likelihood

Once observation set or TDM log likelihoods are found, the catalog object with the highest (most positive) log likelihood value is matched to the observation set or TDM,

respectfully. Since the s parameter is left as a variable for the catalog objects, all of the likelihoods and log likelihoods will contain an s^2 term. When any numerical value for s is used, all log likelihood values will range from $(-\infty, 0]$ and all likelihoods will range from $(0, 1]$. To gain some understanding of the outputs from this algorithm, this method is tested for an s parameter of 25 km – which is within the range of GEO and HEO TLE in-track uncertainties defined by [\[20\]](#).

6. VALIDATION AND RESULTS

This section dives into the validation of both the direct catalog comparison and the arc correlation methods developed in this research. The direct catalog comparison method is validated against the datefirst.txt file (described in Section 2.2.1) using 99 pairs of Space-Track and Vimpel catalogs ranging from January, 2019 to December, 2021. The arc correlation method is validated using observations from the Purdue Optical Ground Station (POGS) and three sets of TDMs from the German Aerospace Center (DLR).

6.1 Direct Catalog Comparison

6.1.1 Validation Against the Datefirst.txt File

The first test run is on the GEO buckets for Space-Track and Vimpel catalogs referenced to 3 February 2020. Table 6.1 shows that for an md2 threshold of $1 \times 10^6/s^2$, the method matches 92.5% of the Vimpel GEO objects listed in the datefirst.txt file to their appropriate Space-Track GEO pair.

Table 6.1. GEO bucket combination for catalogs referenced to 3 February 2020 with an md2 threshold of $1 \times 10^6/s^2$

Combined GEO buckets – 3 Feb 2020				
bucket	md2 thresh	Correctly Matched	Incorrectly Matched	Unmatched
GEO	$1 \times 10^6/s^2$	37/40 (92.5%)	3/40 (7.5%)	0/40 (0.0%)

This test for a single catalog shows that the direct catalog comparison method correctly produces most the Vimpel and Space-Track object pairs shown in the datefirst.txt file. In order to further validate the performance of this algorithm, the GEO buckets of 99 catalog pairs are combined. Table 6.2 shows that from these 99 combined GEO buckets, 93.80% of the Vimpel objects in the datefirst.txt file are matched to the correct Space-Track object when the md2 threshold is $1 \times 10^6/s^2$.

Table 6.2. GEO bucket combination for 99 catalog pairs ranging from January, 2019 through December, 2021

Combined GEO buckets – 99 Space-Track and Vimpel catalog pairs		
bucket	md2 thresh	Avg Correctly Matched
GEO	$1 \times 10^6/s^2$	93.80%

After running a full test (all 99 pairs) on the GEO buckets, a full test is run on the other four buckets.

Table 6.3. All buckets combination for 99 catalog pairs ranging from January, 2019 through December, 2021 with an md2 threshold of $1 \times 10^6/s^2$

All combined buckets – 99 Space-Track and Vimpel catalog pairs		
bucket	md2 thresh	Avg Correctly Matched
LEO	$1 \times 10^6/s^2$	97.17%
MEO	$1 \times 10^6/s^2$	97.23%
GEO	$1 \times 10^6/s^2$	93.80%
HEO	$1 \times 10^6/s^2$	98.30%
Other	$1 \times 10^6/s^2$	98.16%

From the full test of each bucket it is seen that the direct catalog combination method is able to pair over 90% of the Vimpel objects in the datefirst.txt file to their appropriate Space-Track object. It is important to note that one of the key parameters for this method is the md2 threshold. Going back to the two catalogs referenced to 3 February 2020, it is seen that as the md2 threshold is increased from Table 6.1 to 6.4, the number of correctly matched objects in the datefirst.txt file also increases. This trend is verified by a full test of all the buckets for an order of magnitude larger md2 threshold in Table 6.5.

Table 6.4. GEO bucket combination for catalogs referenced to 3 February 2020 with an md2 threshold of $1 \times 10^7/s^2$

Combined GEO buckets – 3 Feb 2020				
bucket	md2 thresh	Correctly Matched	Incorrectly Matched	Unmatched
GEO	$1 \times 10^7/s^2$	38/40 (95%)	2/40 (5%)	0/40 (0.0%)

Table 6.5. All buckets combination for 99 catalog pairs ranging from January, 2019 through December, 2021 with an md2 threshold of $1 \times 10^7/s^2$

All combined buckets – 99 Space-Track and Vimpel catalog pairs		
bucket	md2 thresh	Avg Correctly Matched
LEO	$1 \times 10^7/s^2$	98.05%
MEO	$1 \times 10^7/s^2$	97.38%
GEO	$1 \times 10^7/s^2$	93.83%
HEO	$1 \times 10^7/s^2$	98.32%
Other	$1 \times 10^7/s^2$	98.57%

As the md2 threshold increases, the number of correctly matched objects from the datefirst.txt file also tends to increase (until the threshold reaches a large enough value). However, as the md2 threshold increases, the number of matched Space-Track and Vimpel objects in a bucket also increases. In the case of Table 6.1 there are 113 Vimpel GEO objects with 40 of them being in the datefirst.txt file. For a md2 threshold of $1 \times 10^6/s^2$, 107 Vimpel objects are paired to Space-Track objects with 37 of them being correct pairings as given by the datefirst.txt file. When the md2 threshold is increased to $1 \times 10^7/s^2$ – as in Table 6.4 – 112 of these 113 Vimpel objects are paired to Space-Track objects with 38 of them being correct pairings as given by the datefirst.txt file. Table 6.6 shows the error relationship between the md2 threshold and the pairing of Vimpel to Space-Track objects. As the md2 threshold increases, the number of Type 1 errors increase. As the md2 threshold decreases, the number of Type 2 errors increase.

Table 6.6. Error analysis of the md2 threshold

Error analysis of the md2 threshold		
	same objects	different objects
matched	correct	false positive (Type 1 error)
unmatched	false negative (Type 2 error)	correct

For this research, a md2 threshold value which adequately minimizes both the Type 1 and Type 2 error was unable to be found when using the datefirst.txt file as the truth. It is possible that the datefirst.txt file contains an accurate subset of the same Space-Track and Vimpel objects but not the full set of Space-Track and Vimpel object pairs. For this

case, the datefirst.txt file validates the accurate pairing ability of the algorithm while leaving ambiguity for more Space-Track and Vimpel pairs to be found using this algorithm.

6.1.2 Inconsistency in the Datefirst.txt File

When debugging the md2 filter for the direct catalog comparison method, a table of incorrectly paired Vimpel objects from the datefirst.txt file was created for the GEO buckets of the catalogs referenced to 3 February 2020. Table 6.7 shows the md2s for the algorithm predicted Space-Track object match versus the md2s for the datefirst.txt file true Space-Track object match for each Vimpel object.

Table 6.7. Incorrectly Matched Objects from the datefirst.txt file - 3 Feb 2020

Incorrectly Matched Objects from the datefirst.txt file - 3 Feb 2020				
vimpel satnum	predicted space-track satnum	min md2	true space-track satnum	true md2
82200	41879	$6.0912 \times 10^4/s^2$	42075	$6.4380 \times 10^{10}/s^2$
92400	42075	$5.0579 \times 10^4/s^2$	41879	$6.3123 \times 10^{10}/s^2$

It is seen that the md2 filter predicts Vimpel 82200 to be NORAD 41879 and Vimpel 92400 to be NORAD 42075 while the datefirst.txt file claims the opposite pairing. It can also be seen that the “true” squared mahalanobis distances are six orders of magnitude larger than the predicted squared mahalanobis distances. Because of the large discrepancies in the squared mahalanobis distance values, some online digging was done to see what the actual pairing of these Vimpel and Space-Track objects should be. Figure 6.1 shows the NORAD IDs next to their satellite names in the Space-Track catalog. Figure 6.2 shows a section of the ESA Classification of Geosynchronous objects, issue 21. This section relates Vimpel object 92400 to WGS 9 (NORAD 42075). Therefore, [3] and [44] give enough evidence to claim that the datefirst.txt file is wrong, and that Vimpel object 92400 should be matched to NORAD 42075 as predicted in Table 6.7. It is further possible that the datefirst.txt file flipped its object pairings and that Vimpel object 82200 should be matched to NORAD 41879 as well.

NORAD CAT ID	SATNAME	INTLDES	TYPE	COUNTRY
41879	WGS 8 (USA 272)	2016-075A	PAYLOAD	US
42075	WGS 9 (USA 275)	2017-016A	PAYLOAD	US

Figure 6.1. Space-Track catalog objects 41879 and 42075 [3]

C1.8o ^m	2017-016A	USA 275 (WGS SV-9)	PL
vimpel	GEO (1.00)	2018-12-31 23:59:02	56.84
92400	J2000	42164.600 0.0000340 0.1200 79.7550 342.8190	56.8368

Figure 6.2. ESA Classification of Geosynchronous Objects, Issue 21, pairing WGS 9 to Vimpel 92400 [44]

6.2 Arc Correlation

6.2.1 Validation using the Purdue Optical Ground Station (POGS)

The initial couple tests of the arc correlation method are run using observation sets from the Purdue Optical Ground Station (POGS). The first test is run on an observation set containing 222 observations of NORAD 29486. Since NORAD 29486 is a GPS satellite, its location is well known and the SID group is confident that these observations pertain to it. Table 6.8 shows the algorithm matched Space-Track object to this observation set, its observation set (OS) log likelihood value with the ‘ s^2 ’ term included, and an OS likelihood value for an s value of 25 km – this value is chosen since it coincides with the GEO uncertainty listed in [20].

Table 6.8. Test on an observation set containing 222 observations of NORAD 29486 taken by POGS

29486_PRN31_workspace		
Algorithm Matched Object	OS Log Likelihood l_{OS}	L_{OS} for $s = 25$ km
NORAD 29486	$-15.8932/s^2$	0.9749

These results show that the arc correlation method accurately matches the observation set to NORAD 29486. For an s of 25 km, there is a 97.49% likelihood that NORAD 29486 is the observed object from this set. Figure 6.3 shows an observation (blue asterisk) and NORAD 29486 distribution (light blue mean point and 3σ covariance ellipse) at the observation time in the topocentric equatorial frame. From this figure, it is seen that the mean point of NORAD 29486 almost directly overlays the observation, and this trend is found for all 222 observations in the set. This trend coincides with the high likelihood value and makes sense in the case of a GPS satellite since the positions of these objects are more accurately known than the positions of many other space objects. For further validation and testing of the arc correlation method, sets of TDMs provided by DLR are used.

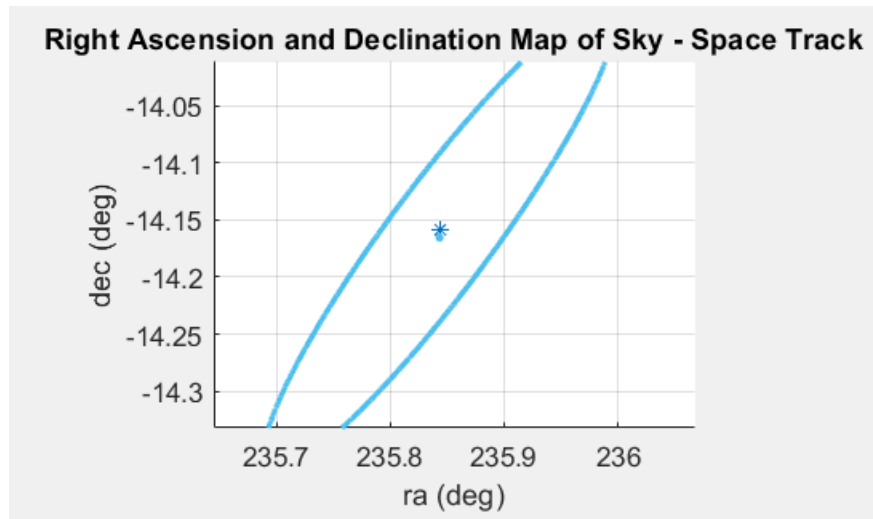


Figure 6.3. Difference between NORAD 29486 distribution (light blue) and observation position (blue asterisk) for newly processed POGS observations

6.2.2 DLR TDM Set 1

The first set of data sent by DLR consists of six TDMs containing observation sets for six different objects. The first five TDMs contain observations for tasked TLE objects, with TDMs two through five containing observations for the clustered ASTRA objects 1KR, 1L, 1M, and 1N, respectfully. The last TDM contains observations for an unknown object. Table 6.9 shows the claimed observed object for each TDM by DLR, the arc correlation matched object, the TDM log likelihood for each matched object and the TDM likelihood for an s of 25 km. From this table it is seen that the first five TDMs are all matched to their claimed observed object by DLR, and the unknown TDM is matched to the ARIANE 5 R/B (NORAD 38993). Another thing to note is that none of these TDMs closely match to any objects in the Vimpel catalog – this finding is consistent with the datefirst.txt file.

Table 6.9. Arc Correlation test on 6 DLR TDMs
Matched Space-Track Objects to TDMs

TDM	Claimed Observed Object (by TDM)	Algorithm Matched Object	TDM Log Likelihood (l_{TDM})	L_{TDM} for $s = 25$ km
1	METEOSAT 8	METEOSAT 8	$-26850.3/s^2$	2.201×10^{-19}
2	ASTRA 1KR	ASTRA 1KR	$-214.378/s^2$	0.7096
3	ASTRA 1L	ASTRA 1L	$-362.579/s^2$	0.5598
4	ASTRA 1M	ASTRA 1M	$-1110.98/s^2$	0.1690
5	ASTRA 1N	ASTRA 1N	$-1315.88/s^2$	0.1218
6	UNKNOWN	ARIANE 5 R/B	$-63.3361/s^2$	0.9036

TDM 1: METEOSAT 8

For the first TDM, 19 out of the 20 observation sets – containing 6 or 7 observations a piece – returned METEOSAT 8 (NORAD 27509) as the most likely object. For the specific observation sets in the TDM, the OS log likelihood for METEOSAT 8 varies greatly from around $-3/s^2$ in some sets to around $-7 \times 10^4/s^2$ in others. This wide range results in an average TDM log likelihood of $-26850.3/s^2$. The next closest potential object is NORAD 9009 as seen in Table 6.10. This table shows that even though METEOSAT 8 is matched

with a low TDM likelihood value, it still significantly more likely than the next closest Space-Track object.

Table 6.10. TDM 1: Likely Space-Track objects

TDM 1: Most Likely Space-Track objects			
NORAD ID	Space-Track satname	l_{TDM}	L_{TDM} for $s = 25$ km
29055	METEOSAT 8	$-26850.3/s^2$	2.201×10^{-19}
9009	PALAPA 1	$-437071/s^2$	1.958×10^{-304}

TDMs 2–5: ASTRA Cluster

The second through fifth TDMs contain observation sets for the clustered ASTRA objects 1KR, 1L, 1M, and 1N. Clustered objects have very similar orbits which makes them the hardest objects to distinguish from each other. Specifically, this ASTRA cluster makes up the most densely populated region in GEO. Figures 6.4–6.6 show some of the observations tasked for ASTRA 1KR in TDM 2, highlighting the overlapping nature of the ASTRA cluster in the 2D observation frame.

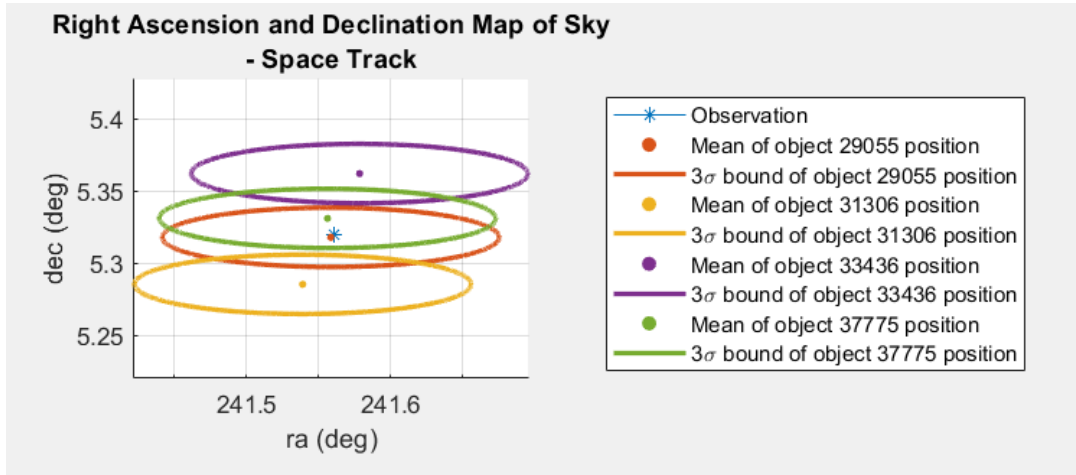


Figure 6.4. ASTRA cluster in the observation frame for an observation in TDM 2 OS 7

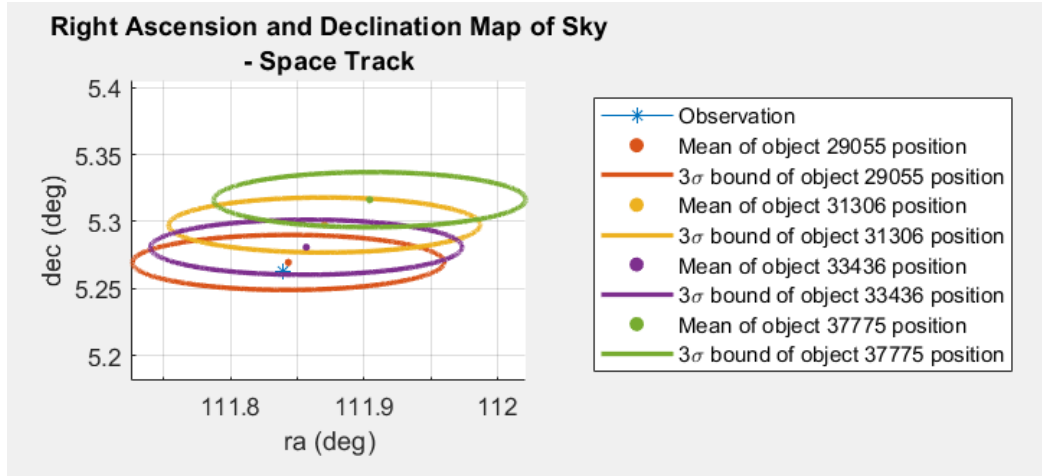


Figure 6.5. ASTRA cluster in the observation frame for an observation in TDM 2 OS 8

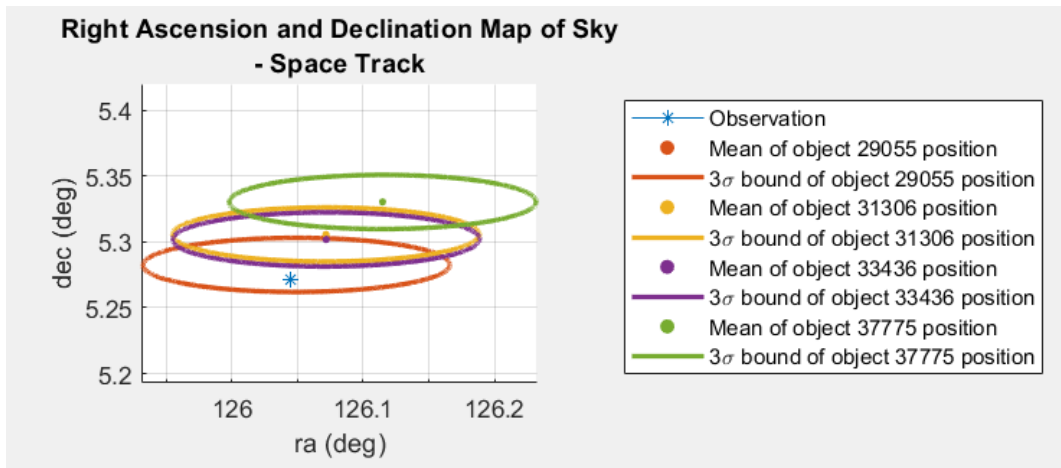


Figure 6.6. ASTRA cluster in the observation frame for an observation in TDM 2 OS 9

Even with this challenge, the arc correlation method was able to correctly pair all the TDMs to their claimed object by DLR. Tables 6.11–6.14 show the log likelihoods for each clustered ASTRA object with respect to TDMs 2 through 5.

Table 6.11. TDM 2: Likely Space-Track objects

TDM 2: Most Likely Space-Track objects			
NORAD ID	Space-Track satname	l_{TDM}	L_{TDM} for $s = 25$ km
29055	ASTRA 1KR	$-214.378/s^2$	0.7096
31306	ASTRA 1L	$-2468.30/s^2$	0.01926
33436	ASTRA 1M	$-5754.78/s^2$	1.003×10^{-4}
37775	ASTRA 1N	$-6147.10/s^2$	5.352×10^{-5}

Table 6.12. TDM 3: Likely Space-Track objects

TDM 3: Most Likely Space-Track objects			
NORAD ID	Space-Track satname	l_{TDM}	L_{TDM} for $s = 25$ km
31306	ASTRA 1L	$-362.578/s^2$	0.5598
29055	ASTRA 1KR	$-2704.48/s^2$	0.01320
37775	ASTRA 1N	$-6749.79/s^2$	2.041×10^{-5}
33436	ASTRA 1M	$-11398.1/s^2$	1.202×10^{-8}

Table 6.13. TDM 4: Likely Space-Track objects

TDM 4: Most Likely Space-Track objects			
NORAD ID	Space-Track satname	l_{TDM}	L_{TDM} for $s = 25$ km
33436	ASTRA 1M	$-1110.98/s^2$	0.1690
29055	ASTRA 1KR	$-2690.33/s^2$	0.01351
37775	ASTRA 1N	$-3166.57/s^2$	6.304×10^{-3}
31306	ASTRA 1L	$-5726.08/s^2$	1.050×10^{-4}

Table 6.14. TDM 5: Likely Space-Track objects

TDM 5: Most Likely Space-Track objects			
NORAD ID	Space-Track satname	l_{TDM}	L_{TDM} for $s = 25$ km
37775	ASTRA 1N	$-1315.88/s^2$	0.1218
31306	ASTRA 1L	$-3321.51/s^2$	4.920×10^{-3}
33436	ASTRA 1M	$-5996.38/s^2$	6.812×10^{-5}
29055	ASTRA 1KR	$-6552.07/s^2$	2.800×10^{-5}

It is seen in these tables that the arc correlation method appropriately pairs the correct ASTRA object while assigning the rest of the objects significantly lower log likelihood values than the paired object. Therefore, the arc correlation method is shown to work in identifying clustered objects from observations. Looking at the observation sets for each TDM (containing, on average, 6 to 7 observations per set), 13/15 sets are matched to ASTRA 1KR in TDM 2, 13/17 sets are matched to ASTRA 1L in TDM 3, 9/15 sets are matched to ASTRA 1M in TDM 4, and 11/16 sets are matched to ASTRA 1N in TDM 5.

One potential source of error for these TDMs (especially 4 and 5) is that not all of the observation sets in the TDMs are matched to the claimed object being observed. Since the ASTRA cluster is very dense, it is possible that some of these observation sets actually pertain to a different cluster object than the one claimed to be being observed. For example, in TDM 5 OS 6, ASTRA 1KR is matched to the set with an l_{OS} of $-85.4019/s^2$. The next closest object is ASTRA 1L with an l_{OS} of $-2001.50/s^2$, and then ASTRA 1N (the claimed object) is matched with an l_{OS} of $-5209.93/s^2$. The large difference in log likelihood values between ASTRA 1KR and ASTRA 1N for this observation set may mean that OS 6 in TDM 5 should really be an observation set in TDM 2.

TDM 6: Unknown

The last TDM in this set contains 20 observation sets of an unknown object that are all matched to the ARIANE 5 R/B (NORAD 38993) by the arc correlation method. Table 6.15 shows the most likely Space-Track objects for TDM 6, and it shows that the next closest object after NORAD 38993 is NORAD 41384 with a TDM log likelihood of $-424265/s^2$. Therefore, it is very likely that the observation sets in TDM 6 contain observations of the ARIANE 5 R/B and highly unlikely that these observation sets pertain to any other object in the Space-Track and Vimpel catalogs.

Table 6.15. TDM 6: Likely Space-Track objects

TDM 6: Most Likely Space-Track objects			
NORAD ID	Space-Track satname	l_{TDM}	L_{TDM} for $s = 25$ km
38993	ARIANE 5 R/B	$-63.3361/s^2$	0.9036
41384	IRNSS 1F	$-424265/s^2$	1.551×10^{-295}

6.2.3 DLR TDM Set 2

The second set of data sent by DLR consists of two TDMs. The first TDM contains 70 observation sets of WGS 9 spanning from January 2019 through October 2019. The second TDM contains 80 unknown observation sets ranging from 13 February 2020 to 22 February 2020. This second TDM is the only TDM containing observation sets that do not necessarily pertain to the same object.

TDM 1 (2017-16A): WGS 9

Looking back to Section 6.1.2, it is discussed that datefirst.txt file paired Vimpel objects 82200 and 92400 to the incorrect Space-Track objects. To further test this theory, DLR sent a TDM containing 70 observation sets tasked for WGS 9 – having an average of 7 observations per set. This 2017-16A TDM is processed and matched to objects in both the Space-Track and Vimpel catalogs, and the results are shown in Table 6.16. Since the arc correlation method matches the 2017-16A TDM to NORAD 42075 (with an l_{TDM} of $-6612.60/s^2$) in the Space-Track catalog and to Vimpel 92400 (with an l_{TDM} of $-7793.64/s^2$) in the Vimpel catalog, NORAD 42075 is indirectly matched to Vimpel 92400. This finding further validates the claim made in Section 6.1.2.

Table 6.16. Arc Correlation results for 2017-16A TDM

TDM 1 (2017-16A) - Claimed object: WGS-9			
Catalog	Algorithm Matched Object	l_{TDM}	L_{TDM} for $s = 25$ km
Space-Track	NORAD 42075 (WGS-9)	$-6612.60/s^2$	2.542×10^{-5}
Vimpel	Vimpel 92400	$-7793.64/s^2$	3.841×10^{-6}

For the Space-Track catalog, 61 of the 70 observation sets matched NORAD 42075 as the closest object with the majority of the l_{OS} values ranging from around $-100/s^2$ to $-10000/s^2$. For the Vimpel catalog, 68 of the 70 observation sets matched Vimpel 92400 as the closest object with the majority of these l_{OS} values range from $-1000/s^2$ to $-13000/s^2$. Tables 6.17 and 6.18 show the TDM log likelihoods for the closest matched Space-Track objects and Vimpel objects to this TDM. These tables show that NORAD 42075 is reasonably the most likely observed object for the Space-Track catalog and that Vimpel 92400 is by far the most likely observed object for the Vimpel catalog. It is also seen that Vimpel object 92400 has a closer l_{TDM} than any of the other closely matched Space-Track objects (excluding NORAD 42075).

Table 6.17. TDM 1: Likely Space-Track objects

TDM 1: Most Likely Space-Track objects			
NORAD ID	Space-Track satname	l_{TDM}	L_{TDM} for $s = 25$ km
42075	WGS 9	$-6612.60/s^2$	2.542×10^{-5}
36032	NSS 12	$-13121.2/s^2$	7.628×10^{-10}
39612	EXPRESS AT1	$-95105.2/s^2$	8.206×10^{-67}
42698	INMARSAT 5-F4	$-214091/s^2$	1.714×10^{-149}
40258	LUCH (OLYMP)	$-459158/s^2$	8.799×10^{-320}

Table 6.18. TDM 1: Likely Vimpel objects

TDM 1: Most Likely Space-Track objects		
Vimpel ID	l_{TDM}	L_{TDM} for $s = 25$ km
92400	$-7793.64/s^2$	3.841×10^{-6}
145303	$-425166/s^2$	3.666×10^{-296}

TDM 2 (unassociated)

The second TDM for this set contains 80 observation sets pertaining to various unknown objects. Each observation set – labeled by an assigned ID from DLR – contains about 3 to 5 observations and is matched to the Space-Track and Vimpel catalogs using the arc correlation method. Table 6.19 gives all of the matched Space-Track objects with l_{OS} values greater than $-2.5 \times 10^4/s^2$. This table is sorted first by the largest likelihood and second

by the NORAD ID, so that the observation sets which matched to the same Space-Track object are grouped together. For Vimpel, the matched objects with l_{OS} values greater than $-2.5 \times 10^4/s^2$ are shown in Table 6.20. This table is sorted like Table 6.19 – first by the largest likelihood and second by the Vimpel ID.

For the observation sets which are grouped together, further testing is run to determine if these observation sets likely pertain to the same object. For this testing, the groups of observation sets matching a single catalog object are put through a two-body least squares orbit determination algorithm – as described in Section 4.6. The initial orbit used in this algorithm is the orbit of the matched catalog object at the time of the earliest observation in all the sets. If an orbit is determined, then the groups of observation sets likely pertain to the same object. If an orbit fails to be determined, then these observation sets may not pertain to the same objects. The last column in Tables 6.19 and 6.20 states whether or not a two body least squares orbit could be determined for each group of observation sets.

Table 6.19. TDM 2 Space-Track object matches

Matched Space-Track Objects to Observation Sets with $l_{OS} > -2.5 \times 10^4/s^2$				
DLR OS ID	NORAD ID	l_{OS}	L_{OS} ($s = 25$ km)	Orbit det?
2394777	27441	$-0.15277/s^2$	0.9998	
2135840	21726	$-5.11460/s^2$	0.9919	
2394745	28094	$-6.02070/s^2$	0.9904	
2394835	22930	$-7.04715/s^2$	0.9888	
2394845	34264	$-12.1284/s^2$	0.9808	
2394839	25175	$-12.8207/s^2$	0.9797	
2135858	23111	$-12.8912/s^2$	0.9796	
2394822	36745	$-15.7417/s^2$	0.9751	Yes. Likely pertain to same object
2394843	36745	$-16.6320/s^2$	0.9737	
2394829	36745	$-16.9018/s^2$	0.9733	
2394850	36745	$-17.9267/s^2$	0.9732	

2154836	23717	$-16.9725/s^2$	0.9717	
2135827	19928	$-22.2181/s^2$	0.9651	
2394741	20696	$-27.5930/s^2$	0.9568	
2394700	23247	$-37.2368/s^2$	0.9422	
2394792	23966	$-47.7347/s^2$	0.9265	
2394727	21803	$-51.8796/s^2$	0.9203	
2144228	21223	$-65.1479/s^2$	0.9010	
2394802	16295	$-77.1919/s^2$	0.8838	
2135848	41593	$-84.9964/s^2$	0.8728	
2394774	36746	$-95.8843/s^2$	0.8578	
2394782	26721	$-109.114/s^2$	0.8398	
2394861	44475	$-124.543/s^2$	0.8193	Yes. Likely pertain to same object
2394844	44475	$-139.351/s^2$	0.8001	
2394831	44475	$-149.366/s^2$	0.7874	
2394824	44475	$-163.605/s^2$	0.7823	
2144240	38780	$-153.435/s^2$	0.7697	
2394855	44803	$-185.165/s^2$	0.7436	No. Anomaly
2154840	44803	$-258.748/s^2$	0.7151	
2394755	19857	$-209.607/s^2$	0.6610	
2394848	44186	$-549.919/s^2$	0.4148	Yes. Likely same object
2394827	44186	$-582.282/s^2$	0.3939	
2135830	44867	$-798.930/s^2$	0.2785	
2135157	40534	$-1381.13/s^2$	0.1097	
2144231	44545	$-3950.81/s^2$	0.001798	Yes. Likely same object
2144229	44545	$-4066.19/s^2$	0.001496	
2135152	32373	$-11473.0/s^2$	1.066×10^{-8}	
2394737	14497	$-21688.0/s^2$	8.504×10^{-16}	No. Likely different
2394735	14497	$-22034.0/s^2$	4.889×10^{-16}	

2394736	14497	$-22053.0/s^2$	4.743×10^{-16}	objects
---------	-------	----------------	-------------------------	---------

Table 6.20. TDM 2 Vimpel object matches

Matched Vimpel Objects to Observation Sets with $l_{OS} > -5 \times 10^5/s^2$				
DLR OS ID	Vimpel ID	l_{OS}	L_{OS} ($s = 25$ km)	Orbit det?
2135862	143513	$-93.2613/s^2$	0.8613	Yes. Likely pertain to same object
2394719	143513	$-142.689/s^2$	0.7959	
2144237	143513	$-146.402/s^2$	0.7912	
2394700	144502	$-94.3920/s^2$	0.8598	
2394815	140912	$-330.534/s^2$	0.5893	
2394685	86100	$-11609.2/s^2$	8.573×10^{-9}	
2394689	33500	$-14611.0/s^2$	7.035×10^{-11}	
2144231	47200	$-16649.9/s^2$	2.694×10^{-12}	

Tables 6.19 and 6.20 show the results of the arc correlation algorithm for the observation sets in the unassociated TDM. When looking specifically at the groups of observation sets, it is seen that a least squares two-body orbit is determined for the observation sets pertaining to NORAD objects 36745, 44475, 44186, and 44545 and Vimpel object 143513. Figure 6.7 shows the observations, initial guess orbit, and determined least squares two-body orbit for the NORAD 36745 group – note that this plot is not to scale. Figures 6.8 and 6.9 show the right ascension and declination residuals for this case. The convergence seen in these figures is also seen in the rest of the groups with determined two-body least squares orbits.

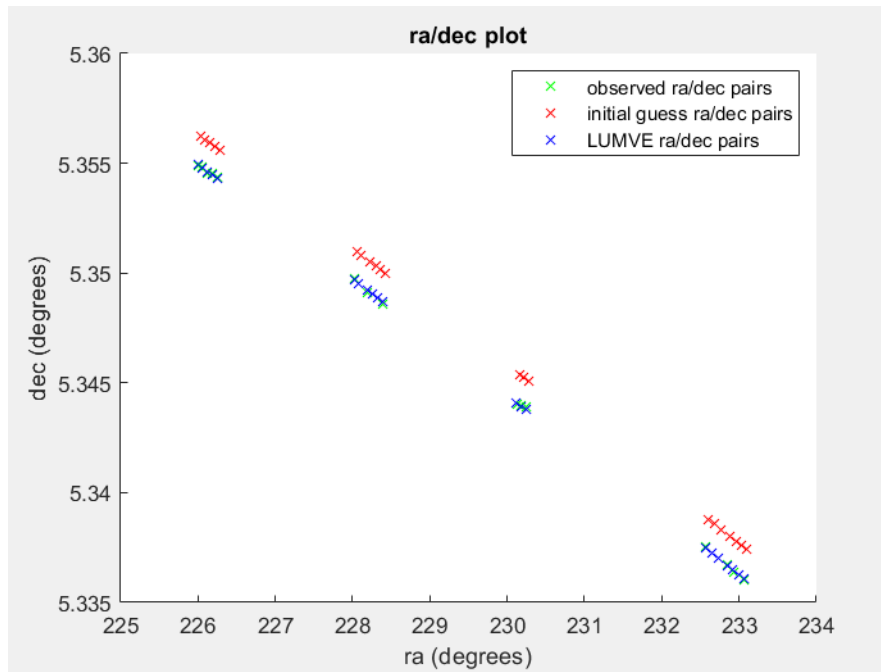


Figure 6.7. Determined least squares two-body orbit for the observation sets pertaining to NORAD 36745

For the observation sets in last group of Table 6.19, a two-body least squares orbit is not determined. Looking at Figure 6.10 it is clear that the initial orbit for NORAD 14497 does not match the observations. Therefore, it is likely that these observation sets are not matched to any of the objects in the Space-Track catalog. This result is not the case for the group pertaining to NORAD 44803 as seen in Figure 6.11.

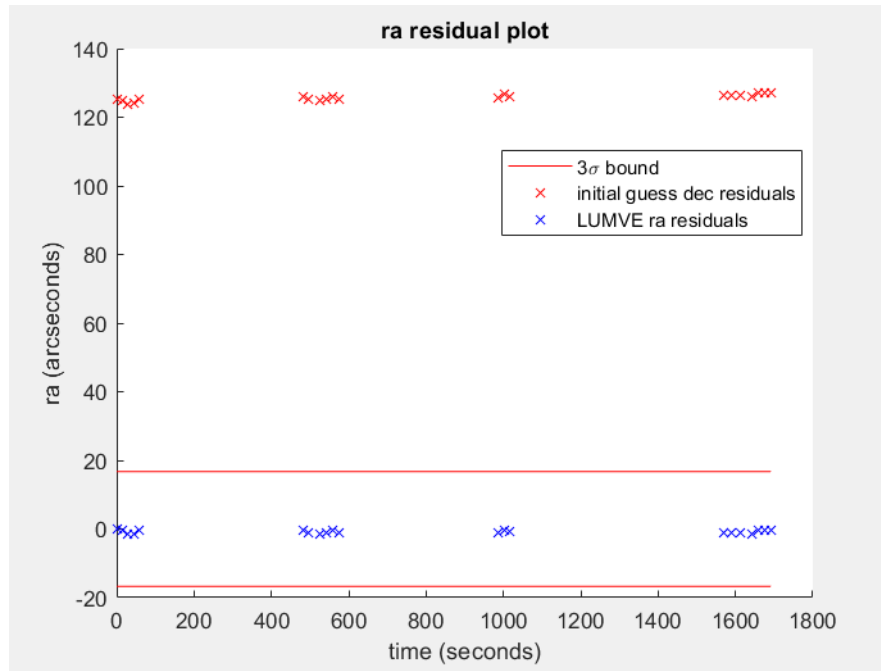


Figure 6.8. Right Ascension residuals for the NORAD 36745 two-body least squares orbit determination

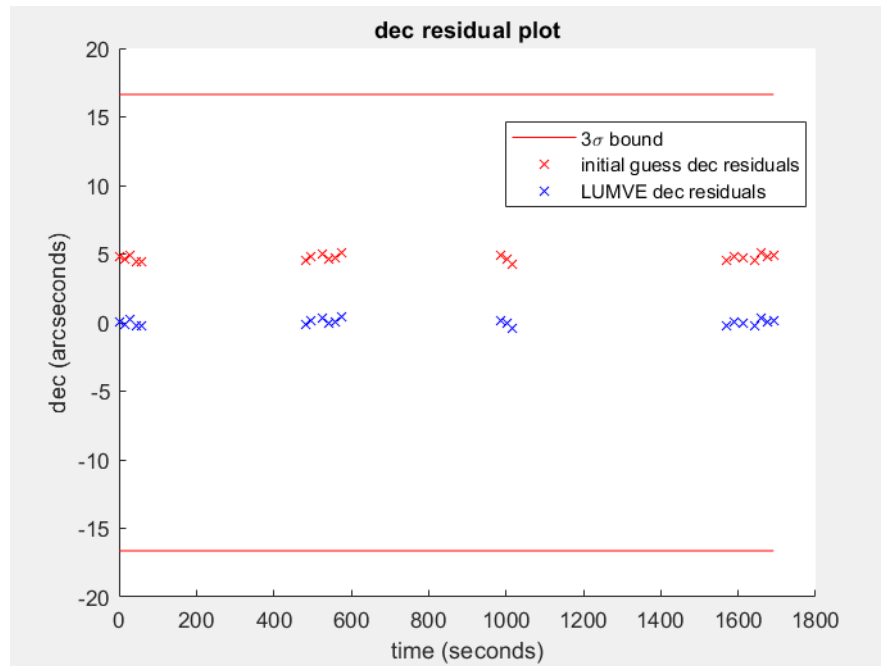


Figure 6.9. Declination residuals for the NORAD 36745 two-body least squares orbit determination

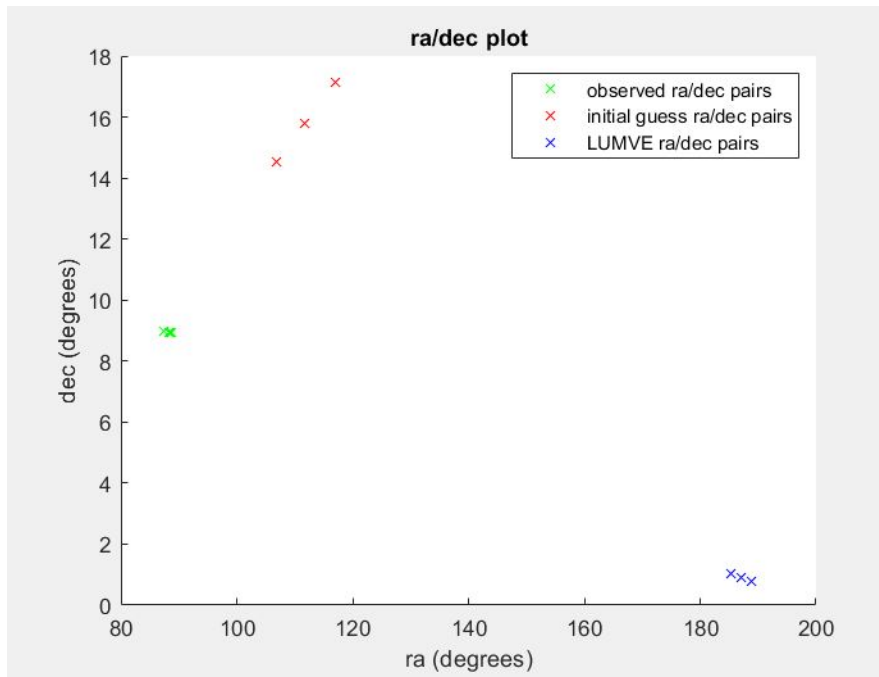


Figure 6.10. Undetermined least squares two-body orbit for the observation sets pertaining to NORAD 14497

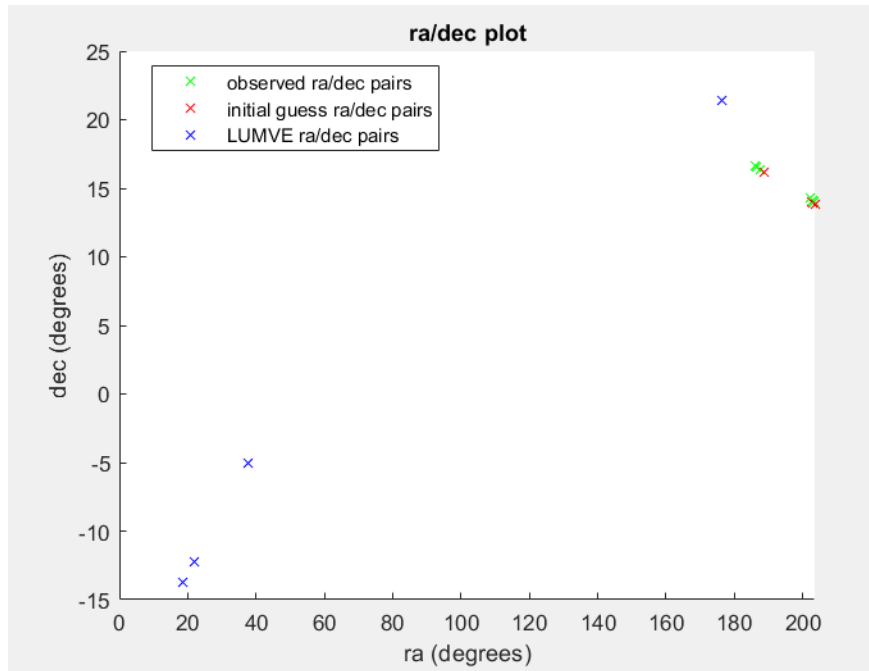


Figure 6.11. Undetermined least squares two-body orbit for the observation sets pertaining to NORAD 44803

Figure 6.11 shows the initial guess for NORAD 44803, the observations in the group, and the two-body least squares determined orbit. It is seen that, even though the least squares algorithm does not converge, the initial guess orbit nearly overlays the observations. Further digging on space-track.org reveals that NORAD 44803 is in an elliptical orbit with an average perigee height of 229 km, an average apogee height of 29284 km, and an average period of 509.61 minutes [3]. Additionally, the time between the observation sets in the NORAD 44803 group is nearly 1 day (1440 minutes). This means that NORAD 44803 would have passed perigee at least two times between the first and second observation sets in the group. As its perigee is so close to the Earth, it is probable that the effects of drag were too large for a two-body orbit estimate to be accurate in this case. Therefore, while the observation sets pertaining to NORAD 44803 do not converge for a two-body least squares solution, they are still assumed to pertain to NORAD 44803 and labeled as an anomaly. In future work, this assumption should be tested using a least-squares algorithm which takes into account the perturbations listed in Section 3.5.

Since the two-body least squares algorithm does not converge in the NORAD 14497 case, objects which match with log likelihoods in these areas can be deemed unlikely matches. A greater confidence is given to the matches with log likelihoods closer than $-4000/s^2$ since the least squares algorithm was able to converge for matched objects in this case. When running the least squares method on single tracklets, using the matched object as an initial guess, it was found that NORAD 32373, NORAD 14497, Vimpel 86100, Vimpel 33500, and Vimpel 47200 are all very unlikely matches to their observation set. Firstly, the two body least squares algorithm does not converge for these objects, and secondly, the initial guess locations of these objects do not match the observation locations. While more tests would need to be run to determine a clear confidence threshold, it can be reasonably assumed that any objects matched with log likelihoods lower than $-1.2 \times 10^4/s^2$ – or likelihoods lower than 1×10^{-8} for $s = 25$ km – are unlikely matches.

6.2.4 DLR TDM Set 3

The third set of data sent by DLR consists of 14 TDMs of known objects. These TDMs consist of 1 to 7 observation sets with an average of 4 observations per set, and their arc correlation results are shown in Tables 6.21–6.34. Space-Track and Vimpel objects are said to be unmatched if their l_{TDM} falls below $-1 \times 10^5/s^2$, and all the Space-Track and Vimpel pairs are referenced to the datefirst.txt file. For the Vimpel matched object in TDM 9, an anomaly is found.

Table 6.21. Arc Correlation results for 1993-056A TDM

TDM 1 (1993-056A.tdm) - Claimed object: UFO 2 (USA 95)			
Catalog	Algorithm Matched Object	l_{TDM}	L_{TDM} for $s = 25$ km
Space-Track	NORAD 22787 (UFO 2)	$-676.474/s^2$	0.3388
Vimpel	Vimpel 143522 (UFO 2)	$-23008.6/s^2$	1.028×10^{-16}

Table 6.22. Arc Correlation results for 1994-035A TDM

TDM 2 (1994-035A.tdm) - Claimed object: UFO 3 (USA 104)			
Catalog	Algorithm Matched Object	l_{TDM}	L_{TDM} for $s = 25$ km
Space-Track	NORAD 23132 (UFO 3)	$-4.26997/s^2$	0.9932
Vimpel	Vimpel 143701 (UFO 3)	$-147.628/s^2$	0.7896

Table 6.23. Arc Correlation results for 1996-042A TDM

TDM 3 (1996-042A.tdm) - Claimed object: UFO 7 (USA 127)			
Catalog	Algorithm Matched Object	l_{TDM}	L_{TDM} for $s = 25$ km
Space-Track	NORAD 23967 (UFO 7)	$-2.25734/s^2$	0.9964
Vimpel	Vimpel 143613 (UFO 7)	$-542.246/s^2$	0.4200

Table 6.24. Arc Correlation results for 1999-063A TDM

TDM 4 (1999-063A.tdm) - Claimed object: UFO 10 (USA 146)			
Catalog	Algorithm Matched Object	l_{TDM}	L_{TDM} for $s = 25$ km
Space-Track	NORAD 25967 (UFO 10)	$-0.67127/s^2$	0.9989
Vimpel	Vimpel 143618 (UFO 10)	$-8326.31/s^2$	1.637×10^{-6}

Table 6.25. Arc Correlation results for 2002-001A TDM

TDM 5 (2002-001A.tdm) - Claimed object: USA 164			
Catalog	Algorithm Matched Object	l_{TDM}	L_{TDM} for $s = 25$ km
Space-Track	NORAD 27168 (USA 164)	$-3.85762/s^2$	0.9938
Vimpel	Vimpel 143523 (USA 164)	$-4684.19/s^2$	5.560×10^{-4}

Table 6.26. Arc Correlation results for 2002-040A TDM

TDM 6 (2002-040A.tdm) - Claimed object: EUTE 12 WEST A (AB 1)			
Catalog	Algorithm Matched Object	l_{TDM}	L_{TDM} for $s = 25$ km
Space-Track	NORAD 27508 (AB 1)	$-26.3860/s^2$	0.9587
Vimpel	Unmatched	N/A	N/A

Table 6.27. Arc Correlation results for 2005-049B TDM

TDM 7 (2005-049B.tdm) - Claimed object: METEOSAT 9 (MSG 2)			
Catalog	Algorithm Matched Object	l_{TDM}	L_{TDM} for $s = 25$ km
Space-Track	NORAD 28912 (MSG 2)	$-7.41843/s^2$	0.9882
Vimpel	Vimpel 25701	$-36279.0/s^2$	6.177×10^{-26}

Table 6.28. Arc Correlation results for 2006-012A TDM

TDM 8 (2006-012A.tdm) - Claimed object: ASTRA 1KR			
Catalog	Algorithm Matched Object	l_{TDM}	L_{TDM} for $s = 25$ km
Space-Track	NORAD 29055 (ASTRA 1KR)	$-2230.46/s^2$	0.02819
Vimpel	Unmatched	N/A	N/A

Table 6.29. Arc Correlation results for 2007-046A TDM

TDM 9 (2007-046A.tdm) - Claimed object: WGS F1 (USA 195)			
Catalog	Algorithm Matched Object	l_{TDM}	L_{TDM} for $s = 25$ km
Space-Track	NORAD 32258 (WGS F1)	$-106.538/s^2$	0.8433
Vimpel	Vimpel 143629 (WGS F1)	$-313112/s^2$	2.676×10^{-218}

Table 6.30. Arc Correlation results for 2009-017A TDM

TDM 10 (2009-017A.tdm) - Claimed object: WGS F2 (USA 204)			
Catalog	Algorithm Matched Object	l_{TDM}	L_{TDM} for $s = 25$ km
Space-Track	NORAD 34713 (WGS F2)	$-89.4020/s^2$	0.8667
Vimpel	Vimpel 143637 (WGS F2)	$-13797.8/s^2$	2.584×10^{-10}

Table 6.31. Arc Correlation results for 2010-039A TDM

TDM 11 (2010-039A.tdm) - Claimed object: AEHF 1 (USA 214)			
Catalog	Algorithm Matched Object	l_{TDM}	L_{TDM} for $s = 25$ km
Space-Track	NORAD 36868 (AEHF 1)	$-0.96300/s^2$	0.9985
Vimpel	Vimpel 143644 (AEHF 1)	$-5818.64/s^2$	9.053×10^{-5}

Table 6.32. Arc Correlation results for 2012-035B TDM

TDM 12 (2012-035B.tdm) - Claimed object: METEOSAT 10 (MSG 3)			
Catalog	Algorithm Matched Object	l_{TDM}	L_{TDM} for $s = 25$ km
Space-Track	NORAD 38552 (MSG 3)	$-2.97371/s^2$	0.9953
Vimpel	Unmatched	N/A	N/A

Table 6.33. Arc Correlation results for 2015-034A TDM

TDM 13 (2015-034A.tdm) - Claimed object: METEOSAT 11 (MSG 4)			
Catalog	Algorithm Matched Object	l_{TDM}	L_{TDM} for $s = 25$ km
Space-Track	NORAD 40732 (MSG 4)	$-110.919/s^2$	0.8374
Vimpel	Unmatched	N/A	N/A

Table 6.34. Arc Correlation results for 2017-016A TDM

TDM 14 (2017-016A.tdm) - Claimed object: WGS 9 (USA 275)			
Catalog	Algorithm Matched Object	l_{TDM}	L_{TDM} for $s = 25$ km
Space-Track	NORAD 42075 (WGS 9)	$-80.3346/s^2$	0.8794
Vimpel	Vimpel 92400 (WGS 9)	$-13034.8/s^2$	8.760×10^{-10}

The first thing to note is that all the Space-Track objects are appropriately matched to the DLR claimed observed object for each TDM. Using the datefirst.txt file (and the direct catalog comparison algorithm for TDM 14) it is also found that the Vimpel objects matched in TDMs 1-5, 9-11, and 14 are appropriately matched to their respective TDM and Space-Track object – even for the Vimpel objects with l_{TDM} s less than $-1.2 \times 10^4/s^2$. Another thing to note is that the Vimpel objects all match with lower l_{TDM} values than their Space-Track counterparts. This result may be due to the fact that DLR performs its tasking assignments using the Space-Track catalog.

One anomaly found is that Vimpel object 25701 is matched to TDM 7. When using the `datefirst.txt` file and the direct catalog comparison algorithm, the Vimpel 25701 to NORAD 28912 object pairing was not confirmed. Since TDM 7 only contains a single observation set, a test was run to see if Vimpel object 25701 is just a close object passing by to the observation rather than the actual object being observed. Figures 6.12–6.14 show the location of Vimpel 25701 with respect to the observation for the three observations in the set. From these figures it is seen that Vimpel 25701 is not actually the object being observed, but that it is just an object passing close by at the time of the observations. Since only one observation set with a small number of tracklets was provided with TDM 7, Vimpel object 25701 was able to be matched closer than the confidence threshold to TDM 7.

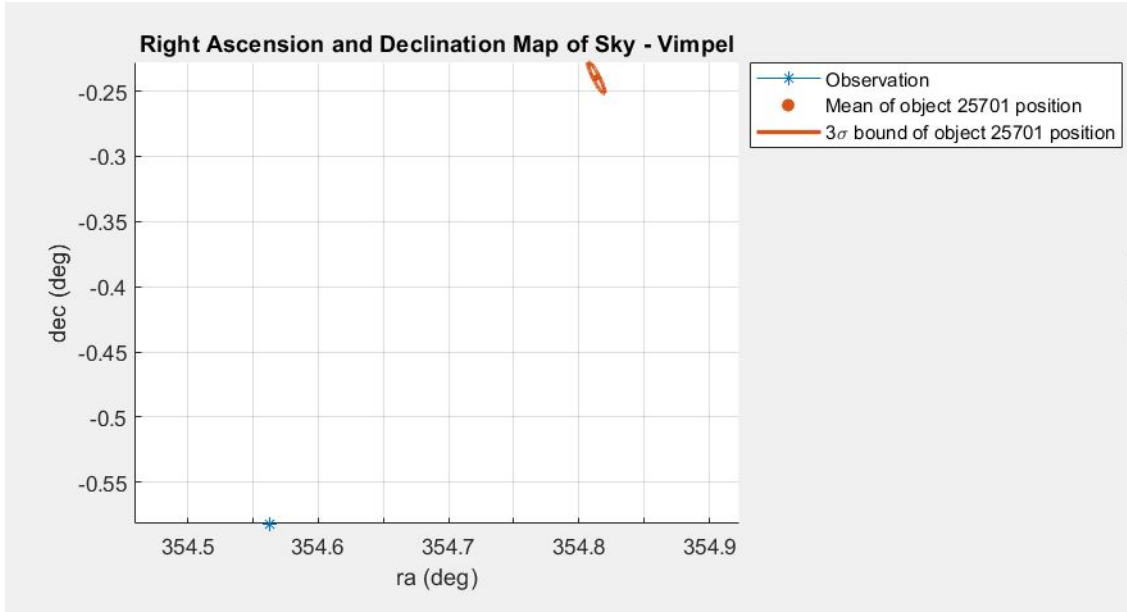


Figure 6.12. TDM 7: Vimpel object 25701 at first observation in set

Another anomaly is that Vimpel object 143629 matches to TDM 9 with a very small likelihood value (the l_{TDM} is $-313112/s^2$). Looking at the two observation sets in this TDM, Vimpel 143629 matches with a l_{OS} of $-134.247/s^2$ to the first one and it matches with an l_{OS} of $-626090/s^2$ to the second one. The matching to the second observation set is significantly worse, and it explains why the l_{TDM} is so poor. To determine potential sources of error, a test was done using different Vimpel catalogs for the weeks prior to and later

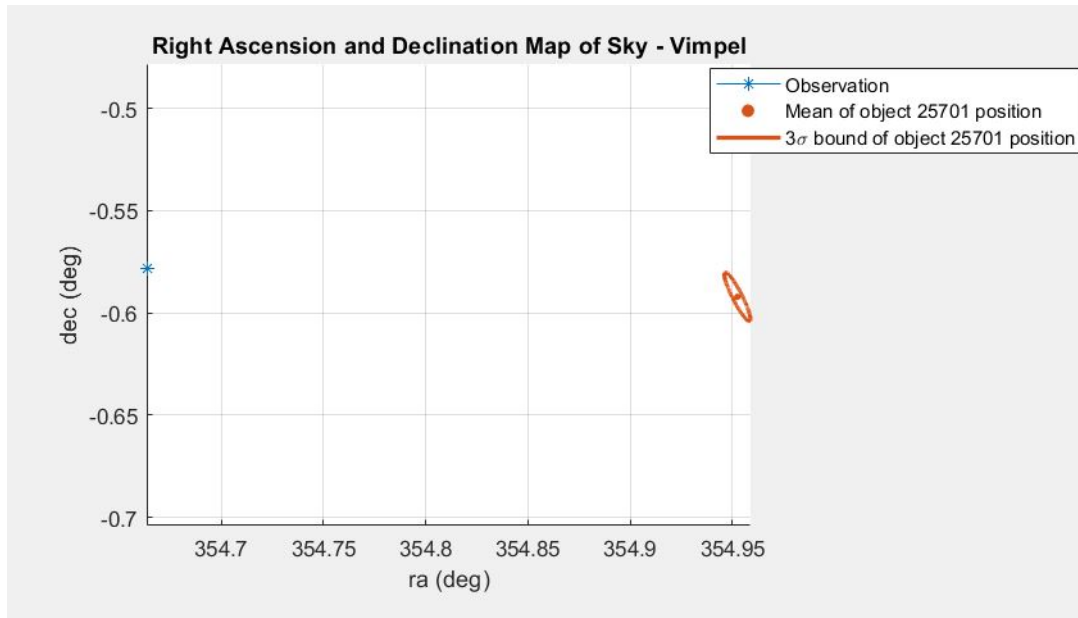


Figure 6.13. TDM 7: Vimpel object 25701 at second observation in set

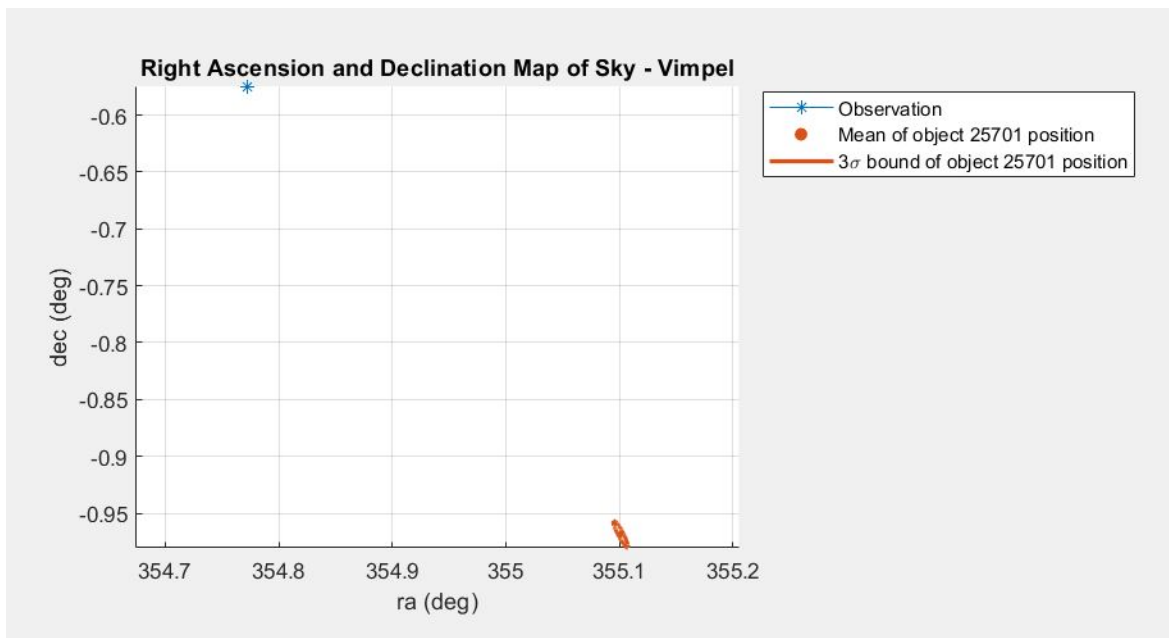


Figure 6.14. TDM 7: Vimpel object 25701 at third observation in set

than the Vimpel catalog being used by the algorithm. Since the first observation set was taken on 1 August 2021 and the second observation set was taken on 4 August 2021, the algorithm chosen Vimpel catalog is referenced to 2 August 2021. When forcing the algorithm to propagate the Vimpel objects from the 26 July 2021 and 9 August 2021 catalogs, the l_{TDM} s obtained for Vimpel 143629 are $-12227.7/s^2$ and $-19929.4/s^2$, respectfully. Both of these l_{TDM} s are significantly better than the l_{TDM} for the closer Vimpel catalog (2 August 2021). It is possible that the Vimpel catalog for 2 August 2021 has an error in one of the perturbation parameters for Vimpel 143629 which is not introduced in the shorter propagation to the first observation set but is introduced in the longer propagation to the second observation set. This error, then, would not be present in the 26 July 2021 or 9 August 2021 catalogs resulting in a better matching of Vimpel 143629 from these catalogs to both observation sets and better l_{TDM} values. Further testing is needed to verify any definite error in the osculating parameters provided for Vimpel 143629 in the 2 August 2021 catalog.

7. SUMMARY

7.1 Conclusions

Two techniques for catalog correlation are developed and tested in this thesis. These methods both rely on a modified nearest neighbor approach to determine the closest potential catalog objects with respect to another catalog or to optical observations. The first method, direct catalog correlation, focuses on the direct correlation of the Space-Track and Vimpel catalogs. This method uses three steps: making buckets, determining potential object Space-Track object matches for each Vimpel object, and determining the most likely Space-Track object match for each Vimpel object, and it is validated against the `datefirst.txt` file – a file provided by Vimpel that claims which Space-Track and Vimpel objects are the same between the catalogs.

The direct catalog combination method is validated by running 99 pairs of Space-Track and Vimpel catalogs ranging from January 2019 to December 2021 through the algorithm and checking the results against the `datefirst.txt` file. For a very inclusive squared Mahalanobis distance threshold, over 90% of all the Vimpel objects in the `datefirst.txt` file are paired to their claimed Space-Track object match. Thus, the method works in pairing Vimpel objects to their associated Space-Track object. The next challenge was to determine a squared Mahalanobis distance threshold that maximizes the number of correctly matched Space-Track and Vimpel objects while minimizing the number of incorrect matches. A value for this threshold was not able to be found. One reason could be that the `datefirst.txt` file only contains an accurate subset of the Space-Track and Vimpel object pairs but not the full set of catalog object pairs. Therefore, the `datefirst.txt` file is used to validate the pairing ability of the algorithm without limiting the potential for more Space-Track and Vimpel object pairs to be found.

The last discovery made in this research using the direct catalog correlation method is the incorrect pairing of Vimpel object 92400 in the `datefirst.txt` file. Data from [3] and [44] give the evidence needed to verify the algorithm predicted pairing of Vimpel 92400 to NORAD 42075 over the `datefirst.txt` claimed pairing of Vimpel 92400 to NORAD 41879. By extension,

this finding results in Vimpel 82200 also being paired incorrectly in the datefirst.txt file (as it was claimed to be NORAD 42075). The algorithm predicted pairing of Vimpel 82200 is to NORAD 41879.

The second method, arc correlation, focuses on the correlation of optical observations (in the form of observation sets) to both the Space-Track and Vimpel catalogs. By correlating a tracklet to objects in both catalogs, the method indirectly matches the catalog objects to each other. First, this method takes in optical observation sets and determines potential catalog object matches to the sets using positional mahalanobis distances in the topocentric equatorial frame. Then, an observation set log likelihood value is calculated for each potential object. This likelihood claims how likely the object is to be the observation set. For the tracking data messages (TDMs) sent by the German Aerospace Center, a TDM log likelihood is also computed. These likelihood values are a function of the in-track uncertainty term, s , in an object's covariance matrix. For these results, s is assigned to be 25 km as this value is the average in-track uncertainty for Geosynchronous two-line element objects [20].

An observation set from the Purdue Optical Ground Station is used to validate the arc correlation method. This set consists of 222 observations tasked for NORAD 29486 (a GPS satellite), and the test results in a 97.49% likelihood that NORAD 29486 is the object observed by the observation set for an s equal to 25 km. Further validation is performed using the first five TDMs sent by the German Aerospace Center. These TDMs contain observation sets of tasked Space-Track objects, and they are all appropriately matched by the arc correlation algorithm to their tasked object. Four of the five TDMs pertain to the ASTRA Cluster 1KR, 1L, 1M, and 1N – this cluster makes up the most densely populated region in GEO.

A TDM consisting of observation sets tasked for NORAD 42075 is used to further correlate NORAD 42075 to Vimpel 92400 (as claimed by the direct catalog comparison method). When processing this TDM for both catalogs, it is found that NORAD 42075 and Vimpel 92400 match as the closest objects in their respective catalog to the TDM, so they are indirectly matched to each other! When processing 14 more TDMs of tasked objects from DLR,

the arc correlation algorithm appropriately pairs these TDMs to their tasked Space-Track object. For the 14 TDMs, TDMs 1-5, 7, 9-11, and 14 are matched to Vimpel objects. Of this group, TDMs 1-5, 9-11, and 14 are appropriately matched to their respective TDM and Space-Track object pair as claimed by the datefirst.txt file and the direct catalog comparison algorithm (for TDM 14). The Vimpel object matching to TDM 7 is an anomaly where a near object, but not the real observed object, is closely matched. For this case, the actual object being observed is not in the Vimpel catalog.

The German Aerospace Center also sent TDMs of unknown objects. The first of these unknown TDMs contains observation sets for a single unknown object, and it is matched to the ARIANE 5 R/B (NORAD 38993) with a TDM likelihood of 90.36% for $s = 25$ km. No other objects are closely matched to this TDM. The second TDM contains 80 unknown observation sets for potentially different objects. For each observation set, the arc correlation algorithm is run, and the observation sets matching to Space-Track and Vimpel catalog objects with observation set log likelihood values closer than $-2.5 \times 10^4/s^2$ are listed. From the two-body least squares method, it is found that the objects with log likelihood values better than -1.2×10^4 – or likelihoods greater than 1×10^{-8} for $s = 25$ km – are likely catalog matches.

7.2 Recommendations and Future Work

For the direct catalog comparison method, a squared Mahalanobis distance filter is used to find potential Space-Track object matches for each Vimpel object. The current filter assigns an uncertainty ellipsoid to each Space-Track object while keeping the Vimpel objects as points in space. It would be interesting to see how the filter works when an uncertainty distribution is also assigned to the Vimpel objects since this distribution would retain the Vimpel object’s velocity information. Instead of computing a Mahalanobis distance (the distance from a point to a distribution); however, this case would compute the distance between two distributions. Since covariance matrix information is not presently available for either catalog, the size and shape of these distributions would still have to be approximated. Something else to note is that the direct catalog comparison method currently correlates the

99 pairs of Space-Track and Vimpel catalogs independently of each other. It would be useful to establish a database that retains information on paired catalog objects throughout the 99 correlations. This database would show which object pairings are more likely – as they are matched in the majority of the catalog pairs – versus which object pairings are less likely. For the arc correlation method, uncertainty distributions of the same size are assigned to each catalog object in the 3D Earth Centered Inertial frame. When rotating from the Earth Centered Inertial frame to the 2D angular topocentric equatorial frame, objects at lower altitudes will have larger 2D covariance matrices. It would be interesting to see the effects of forcing the topocentric covariance matrix for each catalog object to be the same size. This constraint may help reduce the improper correlation of lower regime objects to observation sets of objects in higher orbits.

It would also benefit both methods if more accurate uncertainty information could be known for the cataloged objects. Most of this work relies on the Gaussian uncertainty distribution model used to represent the covariance matrix for a propagated space object. When using short period propagations, this distribution gives a decent representation of the actual propagated covariance matrix for an object. For longer propagations, the representation is not as accurate. Therefore, it would be useful to establish an uncertainty distribution that models the two body trajectory of an object. This way, the in-track direction of the uncertainty would follow the trajectory of the object rather than just extending in the direction of the current velocity vector. As for the results provided in this thesis, they should be used to aid in the determination of previously unknown Space-Track and Vimpel object pairs and the validation of some currently postulated catalog object pairs.

REFERENCES

- [1] NASA, *Space debris and human spacecraft*, M. Garcia, Ed., May 2021. [Online]. Available: https://www.nasa.gov/mission_pages/station/news/orbital_debris.html.
- [2] ESA Space Debris Office, *Space debris by the numbers*, Jan. 2022. [Online]. Available: http://www.esa.int/Safety_Security/Space_Debris/Space_debris_by_the_numbers.
- [3] *Space-track.org*. [Online]. Available: <https://www.space-track.org>.
- [4] European Space Agency, *Low earth orbit*, Feb. 2020. [Online]. Available: https://www.esa.int/ESA_Multimedia/Images/2020/03/Low_Earth_orbit.
- [5] *Deorbit systems*, 2021. [Online]. Available: <https://www.nasa.gov/smallsat-institute/sst-soa/deorbit-systems>.
- [6] ESA Space Debris Office, *Esa's annual space environment report*, May 2021. [Online]. Available: https://www.sdo.esoc.esa.int/environment_report/Environment_Report_latest.pdf.
- [7] B. Weeden, *Us policy and capabilities on ssa*, Jan. 2019. [Online]. Available: <https://swfound-staging.azurewebsites.net/media/206348/weeden-us-policy-and-capabilities-for-ssa.pdf>.
- [8] C. Früh, T. Schildknecht, R. Musci, and M. Ploner, *Catalogue correlation of space debris objects*, 2009. [Online]. Available: <https://conference.sdo.esoc.esa.int/proceedings/sdc5/paper/130/SDC5-paper130.pdf>.
- [9] G. Pulford, "Taxonomy of multiple target tracking methods," *IEE Proceedings - Radar, Sonar and Navigation*, vol. 152, no. 5, p. 291, 2005. DOI: [10.1049/ip-rsn:20045064](https://doi.org/10.1049/ip-rsn:20045064).
- [10] T. M. Cover and P. E. Hart, "Nearest neighbor pattern classification," *IEEE Trans. Inf. Theory*, vol. 13, pp. 21–27, 1967.
- [11] B. Banitalebi and H. Amiri, "An improved nearest neighbor data association method for underwater multi-target tracking," 2008.
- [12] L. G. Taff, "On initial orbit determination," *Astronomical Journal*, vol. 89, pp. 1426–1428, Sep. 1984. DOI: [10.1086/113644](https://doi.org/10.1086/113644).
- [13] R. H. Gooding, "A new procedure for the solution of the classical problem of minimal orbit determination from three lines of sight," *CELESTIAL MECHANICS AND DYNAMICAL ASTRONOMY*, vol. 66, no. 4, pp. 387–423, 1997. DOI: [10.1007/bf00049379](https://doi.org/10.1007/bf00049379).

- [14] A. Milani, G. F. Gronchi, M. D. Vitturi, and Z. Knežević, “Orbit determination with very short arcs. i admissible regions,” *Celestial Mechanics and Dynamical Astronomy*, vol. 90, no. 1-2, pp. 57–85, 2004. DOI: [10.1007/s10569-004-6593-5](https://doi.org/10.1007/s10569-004-6593-5).
- [15] J. Bloch and R. Rast, “Space surveillance one photon at a time,” Jan. 2007.
- [16] K. J. DeMars, M. K. Jah, and P. W. Schumacher, “Initial orbit determination using short-arc angle and angle rate data,” *IEEE Transactions on Aerospace and Electronic Systems*, vol. 48, no. 3, pp. 2628–2637, 2012. DOI: [10.1109/TAES.2012.6237613](https://doi.org/10.1109/TAES.2012.6237613).
- [17] A. Milani, G. Tommei, D. Farnocchia, A. Rossi, T. Schildknecht, and R. Jehn, “Correlation and orbit determination of space objects based on sparse optical data,” *Monthly Notices of the Royal Astronomical Society*, vol. 417, pp. 2094–2103, Nov. 2011. DOI: [10.1111/j.1365-2966.2011.19392.x](https://doi.org/10.1111/j.1365-2966.2011.19392.x).
- [18] X.-H. Wang, J.-F. Li, X.-P. Du, and X. Zhang, “Orbital correlation of space objects based on orbital elements,” *Research in Astronomy and Astrophysics*, vol. 16, no. 3, p. 016, 2016. DOI: [10.1088/1674-4527/16/3/052](https://doi.org/10.1088/1674-4527/16/3/052).
- [19] S. Yu, R. Sun, and C. Zhang, *A method for catalogue correlation of space objects*, 2019. [Online]. Available: <https://conference.sdo.esoc.esa.int/proceedings/neosst1/paper/450/NEOSST1-paper450.pdf>.
- [20] C. Früh and T. Schildknecht, “Accuracy of two-line-element data for geostationary and high-eccentricity orbits,” *Journal of Guidance, Control, and Dynamics*, vol. 35, no. 5, pp. 1483–1491, 2012. DOI: [10.2514/1.55843](https://doi.org/10.2514/1.55843).
- [21] S. Dong, D. Chen, P. Yang, and Y. Zhang, “A real-time correlation method for space objects in satellite-based coordinate system,” in *2019 IEEE 2nd International Conference on Electronics Technology (ICET)*, 2019, pp. 263–268. DOI: [10.1109/ELTECH.2019.8839380](https://doi.org/10.1109/ELTECH.2019.8839380).
- [22] M. J. Holzinger, D. J. Scheeres, and K. T. Alfriend, “Object correlation, maneuver detection, and characterization using control distance metrics,” in *Journal of Guidance, Control, and Dynamics*, vol. 35, 2012, pp. 1312–1325. DOI: [10.2514/1.53245](https://doi.org/10.2514/1.53245).
- [23] Space Foundation Editorial Team, *Space situational awareness*, Feb. 2021. [Online]. Available: https://www.spacefoundation.org/space_brief/space-situational-awareness/.
- [24] 18th Space Control Squadron, Aug. 2020. [Online]. Available: https://www.space-track.org/documents/Spaceflight_Safety_Handbook_for_Operators.pdf.
- [25] T. S. Kelso, *Frequently asked questions: Two-line element set format*, Dec. 2019. [Online]. Available: <https://celestrak.com/columns/v04n03/>.

- [26] E. Olson, *How tracking the international space station works*, May 2017. [Online]. Available: <https://insights.globalspec.com/article/5084/how-tracking-the-international-space-station-works>.
- [27] *Spacedata.vimpel.ru*. [Online]. Available: <http://spacedata.vimpel.ru/welcome>.
- [28] D. A. Vallado and W. D. McClain, *Fundamentals of astrodynamics and applications*. Microcosm Press, 2013.
- [29] C. Frueh, *Space Traffic Management*. Purdue University, 2019.
- [30] P. Ravi, “Investigating on-orbit satellite fragmentation events,” M.S. thesis, 2021.
- [31] O. Montenbruck and E. Gill, *Satellite orbits: Models, methods and applications; with 47 tables, and a CD-ROM*. Springer, 2005.
- [32] J. Seago and D. Vallado, “Coordinate frames of the u.s. space object catalogs,” *Astrodynamics Specialist Conference*, 2000. DOI: [10.2514/6.2000-4025](https://doi.org/10.2514/6.2000-4025). [Online]. Available: <https://geodesy.geology.ohio-state.edu/course/refpapers/AIAA4025.pdf>.
- [33] M. A. Wieczorek and M. Meschede, “Shtools: Tools for working with spherical harmonics,” *Geochemistry, Geophysics, Geosystems*, vol. 19, no. 8, pp. 2574–2592, 2018. DOI: <https://doi.org/10.1029/2018GC007529>.
- [34] G. E. Cook, *Drag coefficients of spherical satellites*. 1966.
- [35] D. A. Vallado and D. Finkleman, “A critical assessment of satellite drag and atmospheric density modeling,” *Acta Astronautica*, vol. 95, pp. 141–165, Oct. 2014. DOI: [10.1016/j.actaastro.2013.10.005](https://doi.org/10.1016/j.actaastro.2013.10.005).
- [36] F. R. Hoots and R. L. Roehrich, “Spacetrack report no. 3: Models for propagation of NORAD element sets,” Aerospace Defense Center, Peterson Air Force Base, Tech. Rep., 1980.
- [37] F. R. Hoots, P. W. Schumacher, and R. A. Glover, “History of analytical orbit modeling in the u. s. space surveillance system,” *Journal of Guidance, Control, and Dynamics*, vol. 27, no. 2, pp. 174–185, 2004. DOI: [10.2514/1.9161](https://doi.org/10.2514/1.9161). eprint: <https://doi.org/10.2514/1.9161>. [Online]. Available: <https://doi.org/10.2514/1.9161>.
- [38] F. R. Hoots, *Sgp4-xp a new tle orbit prediction model*, Feb. 2021. [Online]. Available: <https://www.coursehero.com/file/114453058/SGP4docpdf/>.

- [39] L. G. Jacchia, “New static models of the thermosphere and exosphere with empirical temperature profiles,” *Smithsonian Astrophysical Observatory Cambridge, MA*, May 1970.
- [40] P. C. Mahalanobis, “On the generalised distance in statistics,” *Proceedings of the National Institute of Sciences of India*, pp. 49–55, 1936.
- [41] R. Peck et al, *Introduction to Statistics and Data Analysis*. Thomson Brooks/Cole, 2008, ISBN: 9780495118732.
- [42] M. Bensimhoun, *N-dimensional cumulative function, and other useful facts about gaussians and normal densities*, Jun. 2009. [Online]. Available: https://file.wikipediam.org/wikipedia/commons/a/a2/Cumulative_function_n_dimensional_Gaussians_12.2013.pdf.
- [43] B. Dunbar, *Technology readiness level*, Jul. 2015. [Online]. Available: <https://www.nasa.gov/directorates/heo/scan/definitions/glossary/index.html>.
- [44] ESA Space Debris Office, *Classification of geosynchronous objects*, Jul. 2019. [Online]. Available: http://www.astronomer.ru/data/0128/Classification_of_Geosynchronous_Objects_I21R0.pdf.